UCLouvain

AGRO LOUVAIN

Faculté des bioingénieurs

Assessing the environmental impact of the NEOM project on coastal ecosystems in the Northern Red Sed and Gulf of Aqaba

Author :	Mattias Van Eetvelt
Supervisor :	Emmanuel Hanert
Co-supervisor :	Colin Scherpereel
Readers :	Eric Deleersnijder
	Jonathan Lambrechts
Academic year :	2023 - 2024

Thesis presented in partial fulfillment of the requirements for the degree of Master in Bioengineering : Environmental Bioengineering

Abstract

In the context of a warming world, annual bleaching events are becoming more likely and threaten coral reefs on a global scale, leading to a growing interest in identifying local-scale thermal refugia. However such shallow reef refugia are predicted to disappear in a +2.0 °C climate world. Yet, hope remains as Northern Red Sea (NRS) corals could act as a thermal refuge until the end of the century. While being virtually immune to climate change, these so-called 'super-corals' are not immune to anthropogenic stressors such as the NEOM mega-project. Here, we used a three-dimensional multi-scale ocean model coupled with a Lagragian Particle Tracker (LPT) model to simulate sediment dispersal originating from coastal development sites and assess the environmental impact of the NEOM project on NRS corals. We show that fine sediments (<32µm) have a high potential to impact the entire Gulf of Aqaba (GoA) and part of the NRS, as they can remain suspended in the water column for up to one month and can settle 200 km away from their release site. We identified the most exposed reefs located within 10 km of Sindalah and along 45 km of the Oxagon coastline. Furthermore, we highlight that all the most exposed reefs are located in the NRS; none are within the GoA. To our knowledge, this work is the first to quantitatively assess the environmental impact of the NEOM project on NRS and GoA shallow coral reefs. Based on our results, we expose the need for the implementation of mitigation measures to ensure sustainable coastal development. In a broader way, our model could provide further insights into marine pollution (e.g. desalination plants brines, heavy metals) and mesophotic-shallow reef interaction.

Acknowledgements

Many people have helped me during this master thesis and I want to thank them properly.

I am very grateful to my supervisor Emmanuel Hanert for his excellent guidance, continuous support, and constant presence and availability from the beginning of the year until the very last day.

I would like to particularly thank Colin who has always supported me and reassured me that the 3D hydro will (eventually) not crash and who always took the time to answer my questions, or took the time to have in-depth conversations. This work would not have been the same hadn't he helped as he did. I am very grateful for his help. I also wish to thank Thomas who helped me to fix many bugs and to explain to me the math behind the code. I also want to thank Lauranne and Riana for all their advice, support and constant good mood. Thanks to Douchan, Alexis and Amaury for their feedback and support during the year.

I wish to thank Sam Purkis who granted us access to the OceanX ADCP datasets which were more than welcome for this work.

I shared this year with my fellow SLIM x option 10 students Julien, Marie, and Louis who joined us in January. Sharing this year together was a real pleasure and the post-weekly-meeting coffee was definitely Friday's highlight. I have to give a special mention to Marie with who I shared all the ups and downs, the formations and the bugs of the 3D model. Her enthusiasm for (questionably long) coffee or puzzle breaks was always the most welcome. Doing this master thesis all by myself would have been a totally different experience, I am grateful for her company during this year. I wish them all the very best for the years to come.

I want to thank my all my close friends, but particularly Antoine, Tanguy and Basile for their support during this year but also for the five years we shared together. I want to thank Romain who always took the time to help me when I needed it but more importantly for his presence and support during the last years. Thanks to the Courby friends for the constant good mood.

Thanks to my parents, my sister, and the whole family for the constant love, presence and support.

Contents

Chapter 1

Introduction

The ocean, directly or indirectly, interacts with us in our everyday lives. It plays a major role in controlling the weather and climate, is a major source of food and provides many medicines (Kantha and Clayson, 2000; Jha and Zi-rong, 2004). Yet, it remains largely unexplored (Jantara Junior et al., 2021). Of all ecosystems on Earth, the richest and the most biologically diverse is found on the ocean floor : coral reefs (Moberg and Folke, 1999). While covering less than 0.1% of the ocean floor, tropical coral reef ecosystems provide habitat for at least 25% of known marine species, with many reef species still to be discovered (Fisher et al., 2015). Coral reefs supply vast numbers of people with goods and services : over half a billion people globally depend on coral reef ecosystems for food, income from tourism and fisheries, and coastal protection (Moberg and Folke, 1999; Hoegh-Guldberg, 2011).

Corals reefs are found in a wide range of environments. Warm-water corals are typically found in tropical and subtropical regions where they thrive in shallow sunlit seas (Fig. 1.1). At deeper depths where light is more scarce, mesophotic corals live at depth ranging from 30 to 150 meters. Corals can even be found in the cold and dark depth of the ocean, down to 2000 meters or more. The latter type of corals are called "cold-corals" (Hoegh-Guldberg et al., 2017). The term *coral reef* refers to massive, wave-resistant structures of limestone and calcareous sediments built by skeletons of successive generations of corals. Such reef-building corals are called hard corals or stony corals and belong to the Scleractinia order (Done, 2011).

The animal constituting the light-dependent corals (i.e. warm-water and mesophotic corals), called a polyp, shares a mutualistic relationship with the single-cell algea dinoflagellate, often referred to as zooxanthellae, and lives within the polyp's tissue (Knowlton and Jackson, 2001). The polyp provides the zooxanthellae with a protected environment and the compounds needed for photosynthesis. In return, the zooxanthellae supplies the polyp with the products of photosynthesis that are used to produce calcium carbonate, the coral skeleton. This symbiosis is highly efficient with respect to recycling of precious nutrients. In fact, the symbiote provides up to 90% of a coral's nutritional requirements (Muscatine and Porter, 1977). Being light-dependent, the amount of light available for zooxanthellae to effectively be able to photosynthesise and sustain the coral drives the lower depth threshold at which coral reefs can be found. Particularly, mesophotic (*meso-*, low-light) coral reefs are mainly found between 30 and 150 meters. The abiotic factor affecting the most these ecosystems is the decrease in solar radiation with depth (Lesser et al., 2009). Being further away from surface stressors, mesophotic coral reefs are less degraded than their shallow water counterparts. Indeed, the most profound changes have occurred on coral reefs less than 20 meters deep whereas deeper reefs (> 30 m) have been shown

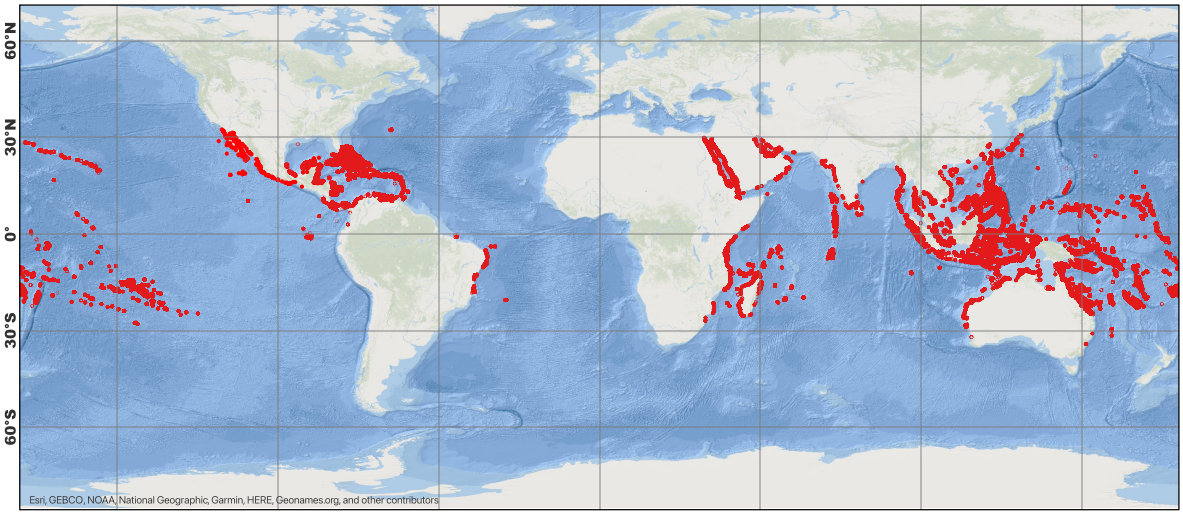

Figure 1.1: Global distribution of warm-water coral reefs. They are usually found in latitudes between 30°S and 30°N. Source: `https://data.unep-wcmc.org` (UNEP-WCMC et al., 2021).

to be largely free from anthropogenic and natural impacts (Bak et al., 2005).

Wave energy, lowered salinity, extreme temperatures, excessive sedimentation, extremely lowtides, uplift or destruction by earthquakes and changes in flow patterns are among the most common natural sources of physical disturbance on reefs (Knowlton and Jackson, 2001). Additionally to natural stressors, coral reef ecosystems are subject to many of the same anthropogenic impacts that affect other marine ecosystems; however, they are considered particularly susceptible to changes in environmental conditions (Wagner et al., 2020). It has been observed that during the last 50 years, almost 30% of corals have disappeared, this loss being explained by both natural and anthropogenic factors (Hoegh-Guldberg, 2005; Pandolfi et al., 2003). Hoegh-Guldberg et al. (2018) made an even more alarming statement, postulating that up to 90% of coral reefs may be gone in the next few decades in the absence of swift conservation action. Recently, a study showed that for a global warming of 1.5°C and 2°C relative to pre-industrial levels, more than 99% and 100% of corals are, respectively, threatened by thermal stress levels that are high enough to cause significant coral bleaching and some mortality (Dixon et al., 2022). Thus making coral reefs one of the world's most endangered ecosystems (Spalding et al., 2001).

As described previously, polyps and zooxanthellae share a mutualistic relationship. However, this relationship is often better viewed as a reciprocally selfish association. Indeed, each partner tries to maximize its net gain from the association by minimizing costs and maximizing benefits. This selfishness has the potential to lead to ecological instability, because if stress makes it difficult for one partner to provide its normal complement of benefits, the other partner may respond in the short term by terminating the relationship. This specific response, called bleaching, occurs when corals experience an intolerable level of stress induced by, for example, temperature, acidity or light radiation. Bleached corals thus refer to corals in which photosynthetic pigments are drastically reduced, typically because of algal death or expulsion. As a consequence, their white skeleton structure becomes visible. They can survive without their normal complement of zooxanthellae for weeks or sometimes months, but their growth and reproductive output are reduced and they will eventually die (Knowlton, 2001).

Although coral bleaching can result from various stressors, the primary and most closely

associated factor is elevated sea temperatures. In fact, temperatures as little as 1℃ over the normal seasonal maximum can provoke substantial bleaching. Hence, global warming is a particular concern since climate models suggest that temperatures sufficient to induce bleaching could become annual events within a few decades (Knowlton, 2001) and global warming will continue to increase in the near term (2021–2040; IPCC (2023)). Bleaching may occur at local scales (e.g. parts of reefs) or at geographic scales that may involve entire reef systems and geographic realms. Such event are defined as 'mass bleaching'. Furthermore, coral bleaching is linked to strong El Niño-Southern Oscillation (ENSO) events (Hoegh-Guldberg, 1999).

2014–2017 was an unprecedented period of successive record-breaking hot years, which coincided with the most severe, widespread, and longest-lasting global-scale mass coral bleaching event ever recorded. The 2014–2017 global-scale coral bleaching event (GCBE) resulted in very high coral mortality on many reefs, rapid deterioration of reef structures, and far-reaching environmental impacts. This 4-years mass bleaching event is now acknowledged to be caused by both the incomplete 2014–2015 and strong 2015-2016 El Niño events (Eakin et al., 2019). During the last decades, marine heatwaves have increased in frequency and intensity across the oceans, increasing heat stress on coral reefs. This has resulted in an increase in the frequency of severe bleaching (Hughes et al., 2018). Given 10 to 15 year recovery times for fast-growing corals on the most ideally located, least-disturbed reefs, it is far more likely we will witness the repeat of severe bleaching on most reefs around the world rather than their recovery(Eakin et al., 2019).

The world's coral reefs are being degraded, and the need to reduce local pressures to offset the effects of increasing global pressures is now widely recognized (De'Ath et al., 2012). Therefore understanding and solving both local and global threats to coral reefs will be critically important if they are to survive some of the greatest rates of environmental change in the recent history of the Earth (Hoegh-Guldberg et al., 2017).

1.1 Northern Red Sea coral reefs

To enhance coral reef resilience in a warming world, the National Oceanic and Atmospheric Administration (NOAA) established the Coral Reef Watch (CRW) program in 2000. Using near real-time satellite products, the CRW provides insights to evaluate the current health of global coral reefs and has accurately predicted all major mass coral bleaching events observed globally since 1997. These metrics all rely on the fact that corals are susceptible to bleach when the sea surface temperature (SST) is 1℃ warmer than the maximum monthly mean temperature (MMM), referred to as the bleaching threshold or 'bleaching rule' (Glynn and D'Croz, 1990), which defines 'hot spots' as used by the NOAA.

In particular, the sea surface temperature anomaly (SSTA) and the degree heating week (DHW) are used the quantify the potential of coral bleaching events. The former is defined as the difference between the current SST compared to the long term averaged SST, while the later is defined as the daily summation, over a 12-week running window, of the hot spot value if ≥1℃, expressed as degrees Celsius weeks (℃ weeks). The DHW shows how much heat stress has accumulated in an area over the past 12 weeks, i.e. how long temperature has stayed above the bleaching threshold (Skirving et al., 2020).

Additionally to the bleaching threshold, patterns of DHW have been linked to global bleaching events. Bleaching often occurs only after a DHW value of 4℃ weeks and widespread mortality at 8℃ weeks (Eakin et al., 2010). However, during the severe El Niño event of 2015-

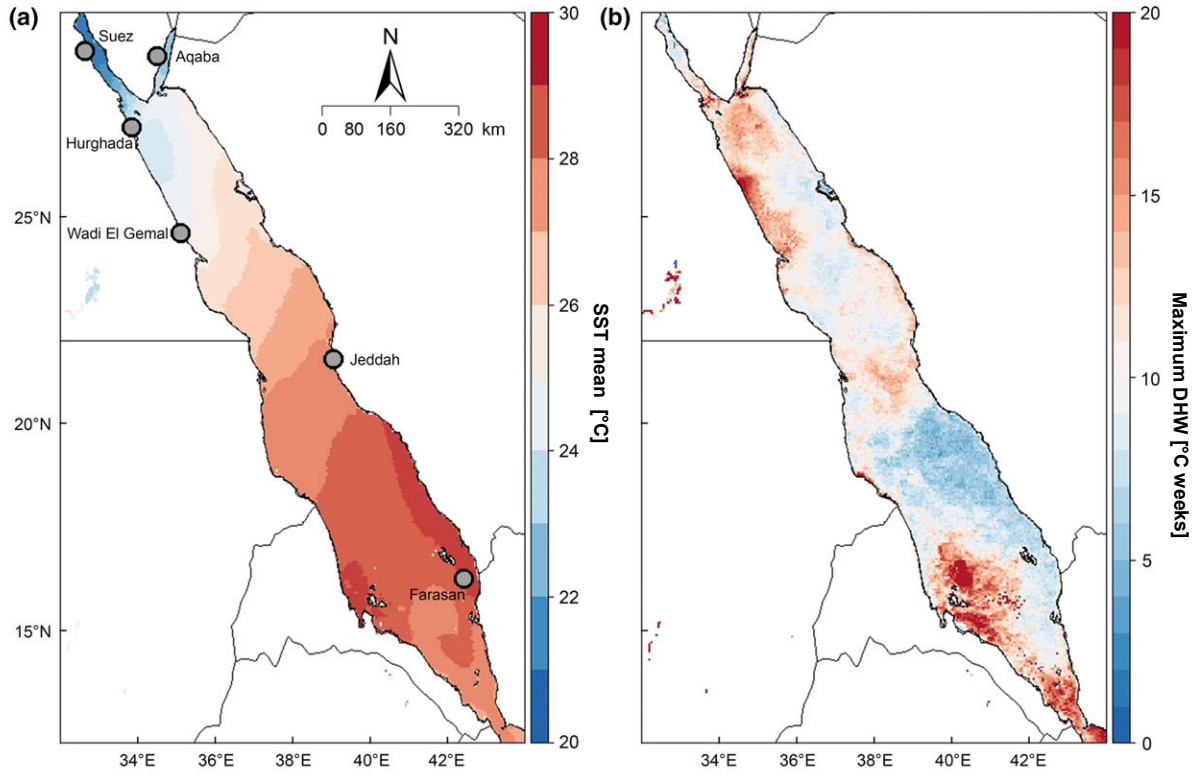

Figure 1.2: Characterization of sea surface temperature (SST) and degree heating weeks (DHWs) across the Red Sea. Maps shows SST mean and maximum DHWs during the period of 1982–2012. Map of SST mean (a) shows a decline of ambient SST northward, while maximum DHW map (b) illustrates that the northern area is exposed to high DHWs despite its low ambient temperature (Osman et al. (2018), modified).

2016, thermal anomalies in the northern Red Sea (NRS) reached DHW values ranging from 7 to 10.5 °C weeks with no observed bleaching. Despite relatively lower DHW (<8°C weeks), bleaching was restricted to the central and southern regions of the Red Sea. This specific event confirms the bleaching patterns observed in the Red Sea for a 30 year-long period : coral reefs in the northern Red Sea do not experience mass bleaching events despite high DHW values. Severe bleaching is restricted to the central and southern regions of the Red Sea where DHWs have been far less intense (DHWs < 4°C-weeks), but more frequent (Osman et al., 2018). Figure 1.2 displays this peculiar distribution of DHW intensity across the Red Sea.

Table 1.1 shows that NRS corals regularly experience water temperatures of 26-29°C. Fine et al. (2013) exposed a coral abundantly found in the gulf of Aqaba (GoA), *Stylophora pistillata*, to a range of temperatures from 26°C up to 34°C. Only at 34°C did they observe a reduction of zooxanthellae density. Later, Evensen et al. (2021) investigated the impacts of acute and chronic thermal stress events. No bleaching was observed up to 32°C as well as a high rate of mortality beyond 34.5°C. The authors argue that, while it is possible that the thermal threshold for this coral population lies within a very narrow range between 34°C and 34.5°C, a more likely explanation is an upper thermal threshold around 34°C. This thermal threshold approximately corresponds to a temperature 6°C above the MMM. Hence, corals in northern Red Sea and in the Gulf of Aqaba do not respect the bleaching rule, i.e. 1°C above MMM (Osman et al., 2018), nor the DHW model (Bellworthy and Fine, 2017) and live well below their bleaching threshold (Fine et al., 2013).

Table 1.1: Summary of environmental variability in different study sites along the Red Sea during 1982–2012 showing annual range of SST, thermal threshold (SST higher than maximum monthly mean by 1°C). Sites arranged from the north to the south (left to right) to show the spatial variability of SST characteristics across latitudinal gradients of the Red Sea (Osman et al. (2018), simplified).

SST metrics (°C)	Gulf of Aqaba	Jeddah	Farasan
Min. SST	18.5	21	23.5
Max. SST	28.8	33.7	33.9
Annual SST mean	23.6 ± 0.6	28.0 ± 0.5	29.0 ± 0.4
Thermal threshold	27.6 ± 1	32.2 ± 1	32.3 ± 1.1

Coral reefs in the northern Red Sea and in the Gulf of Aqaba have extraordinary high thermal tolerance in relation to the ambient water temperatures they thrive in (Fine et al., 2013; Bellworthy and Fine, 2017; Osman et al., 2018; Evensen et al., 2021). This unique feature is supported by the hypothesis that corals of the Red Sea are evolutionary selected for thermal tolerance. This is the outcome of the unique geography and topography of the Red Sea. This elongated sea is connected to the open ocean via a narrow and shallow strait at its southernmost end, the Bab el-Mandeb Strait. Consequently, during the last glacial maximum, when global sea level dropped, the Red Sea became nearly disconnected from the open ocean leading to a local decimation of corals, among others. Reestablishment of coral reefs started after sea level returned to within 20 meters of the present level, around 8000 years before present (Braithwaite, 1987). As the only possible source of coral larvae for recolonization was the Gulf of Aden, each coral larva entering the Red Sea had to pass through the exceedingly warm waters (>32℃ in summer) in the entrance to the Red Sea. The palaeoceanographic conditions in the northern and central Red Sea were similar to present day or warmer at the time corals started to recolonize the Red Sea (Trommer et al., 2010). Since the duration of the corals' planktonic larval stage is in the order of days to weeks (Cetina-Heredia and Connolly, 2011), and since it takes more than 1 year for recently settled corals to start reproducing, the colonization of the northern Red Sea and Gulf of Aqaba must have occurred via stepping stones (Fine et al., 2013).

Assuming that the bleaching threshold for northern Red Sea and Gulf of Aqaba corals is closer to the lower bound proposed by Osman et al. (2018) (32-34℃), there is, at least, a 5℃ gap compared to the expected 27℃ bleaching threshold for such high latitudes (Dalton and Carroll, 2011). Figure 1.3 shows that considering the rate of warming in the region, by the time the Gulf of Aden and southern Red Sea reefs (as well as many other indopacific reefs) will cross their threshold and experience temperatures above 35 °C in 2100, corals in the Gulf of Aqaba will still be experiencing maximum summer temperatures below 31 °C, which is under their bleaching threshold. Therefore, the northern Red Sea and the Gulf of Aqaba is considered as a coral refuge from the effects of climate change. This raises a call for special efforts to protect this exceptional refuge from anthropogenic damage (Fine et al., 2013) and the urge to reduce local stressors(Krueger et al., 2017).

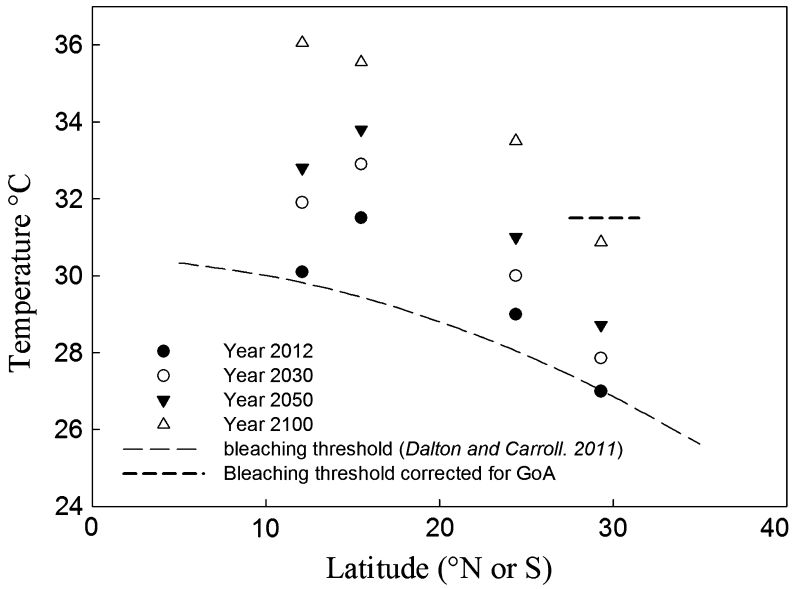

Figure 1.3: Estimates of thermal bleaching threshold by latitude on which present and future Red Sea SST are plotted. SST predictions are for the warmest month in each region, demonstrating that although present-day temperatures in the GoA are already crossing the predicted local bleaching threshold, the actual bleaching threshold (thick dashed line), experimentally identified, will not be crossed even by 2100 (Fine et al., 2013).

1.2 Mesophotic coral ecosystems

Most coral research has focused on shallow corals, partly due to their ease of observation and the inherent limitations of scuba diving, which restricts the exploration depth to approximately 150 meters. However, coral habitats have been confirmed to extend to deeper zones (Lesser et al., 2009). Bongaerts et al. (2010) proposed the 'deep reef refugia hypothesis' (DRRH), which suggests that deep reef areas are protected or dampened from disturbances that affect shallow corals and may provide a viable reproductive source for shallow reef areas after disturbance. Mesophotic coral ecosystems (MCEs) are thus expected to suffer less from antropogenic impacts and higher sea temperatures therefore acting as a larvae source and genetic bank.

Mesophotic reefs usually represent an extension of the shallow-reef ecosystem and share some species composition but harbor as well specific species (Lesser et al., 2009). This shallow-reef continuum suggests a connectivity between shallow and mesophotic reefs, which is integral to the DRRH. Despite this hopeful yet intuitive hypothesis, vertical connectivity has only been assessed in very few locations. Moreover, little evidence exists that supports or refutes that coral larval exchange actively occurs between deep and shallow habitats. However, recent studies using biophysical modelling (Thomas et al., 2015; Holstein et al., 2016; Takeyasu et al., 2023) show encouraging results supporting the deep reef refugia hypothesis.

While being attractive, the DRRH has some limitations. Bongaerts et al. (2017) demonstrated that coral species with similar ecological distributions can exhibit very distinct potentials for vertical connectivity at a single location. Hence, the DRRH should be considered as an ecological concept relevant to individual species, rather than being referred to as an ecosystem-wide phenomenon. Additionally, contrary to what was first hypothesized, mesophotic coral reefs do suffer from natural impacts such as hurricanes and tropical storms (Rocha et al., 2018) as well as from thermal stress and have been shown to bleach (Diaz et al., 2023). Therefore, it is argued that mesophotic reefs are impacted and in as much need of protection as shallow coral reefs

(Rocha et al., 2018; de Oliveira Soares et al., 2020).

The MCEs of Eliat, one of the northernmost cities in the gulf adjacent to Aqaba, are among the most extensively studied MCEs globally as demonstrated by the high number of publications from the region (Eyal et al., 2019). Eliat's MCEs have been characterised as a significant sink of larvae, but the study was conducted only at specific locations (Kramer et al., 2019). Although the latter MCEs are well documented, this is not the case for the MCEs in the rest of the northern Red Sea region. Practically, there is no clear consensus in the literature about the extent to which mesophotic reefs of the NRS and GoA could act as a refuge for shallow ones.

1.3 NEOM : a futuristic mega-city project in the Gulf of Aqaba

While being virtually immune to the effects of climate change, the 'super corals' of the NRS and GoA are not immune to the effects of local anthropogenic disturbances. Table 1.2 shows some of the major threats to NRS and GoA corals. The proximity of Egypt's Suez Canal, which is a very important passageway for oil and commercial tankers, and hence a possible source of oil spills, is a high risk on corals health. Furthermore, cities and touristic centers are hotspots of sewage discharge, which are poorly or non-treated resulting in eutrophication and may compromise corals resilience to global change (Hall et al., 2018).

The Saudi coast (GoA) host the more extensive areas of Red Sea coral reefs (Barale et al., 2007). It is specifically on these shores that NEOM is planned to take place (Fig. 1.4). NEOM is a futuristic mega city project and is part of Saudi Arabia's Vision 2030 economic plan that seeks to diversify the kingdom's economy and reduce its reliance on revenues from oil (Fattouh and

Table 1.2: Threats to coral reefs showing the risk for the considered region(+ low, ++ medium, and +++ high). Simplified from Fine et al. (2019).

Threat	Source	Consequences	NRS	GoA
Oil spills	Ship, oil terminals	Coral and planula larva mortality	+++	+++
Sewage discharge	Cities	Changes in bacterial communities, algal growth	++	++
Diving, snorkeling and reef trampling	Tourism industry (resorts, diving centers)	Corals and coral reef physical destructions, mortality, impacts on reproduction	+++	+++
Coastal construction	Urbanization and coastal infrastructure	Alterations in flow dynamics and physical damage to reefs, sedimentation	+++	+++

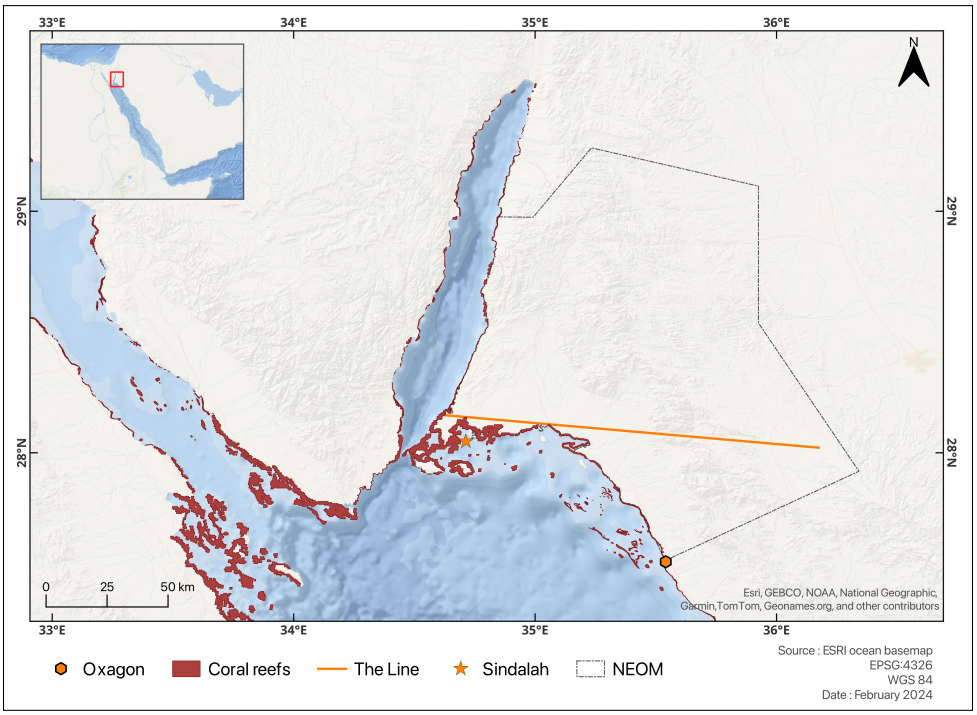

Figure 1.4: NRS and GoA coral reefs with the 26 500 km^2 region allocated to the NEOM project. The approximate location of three of NEOM's subprojects are display, namely The Line, Sindalah and Oxagon.

Sen, 2016). NEOM is expected to be carbon neutral and rely exclusively on renewable energy. This project is divided in various sub-projects. The most popular one is The Line which is a futuristic city that will be shaped as a thin and 150km-long line. Another example is Sindalah, a luxury yacht club that will be build on an entire island on the southernmost part of the Gulf of Aqaba. Altogether, NEOM is planned to attract 1 million citizens (Madakam and Bhawsar, 2020). Over the next 10 years, it will lead to extensive coastal development including the construction of desalination plants, sewage plants and tourist resorts. These human activities have caused and will cause extensive marine pollution, which has the potential to seriously damage Red Sea ecosystems by placing extra stress on organisms that are already threatened or endangered (Lakhouit, 2019). Important dredging project are sources of sediments that impact corals in several ways, but primarily through increased turbidity and deposition. Turbidity from suspended sediments reduces light availability to symbiotic zooxanthellae, which are crucial for coral subsistence as they perform photosynthesis, while sedimentation can smother or bury coral polyps, severely disrupting their normal functions (Erftemeijer et al., 2012; Jones et al., 2019). In fact, fine-grained sediments are particularly detrimental as they significantly reduce light penetration (Storlazzi et al., 2015).

1.4 Objectives of this thesis

NEOM is the major anticipated pressure in the region. Lakhouit (2019) have identified the main threats that the NEOM project could cause on NRS and GoA corals. However, no study has been led to quantify the impacts of those threats on reefs. This work is focused on bringing an answer to the following question :

How and to what extent will the NEOM project impact the coral reefs in the NRS?

To answer to this question we will first model the three-dimensional hydrodynamics using the 3D version of the ocean model SLIM. Then, we will use the modelled currents to simulate sediment dispersal where we will consider various sediment sizes. From the particle tracks we will derive cumulative densities that will allow us to study the spatio-temporal patterns of the sediments and compute environmental indicators.

Chapter 2

Materials and Methods

This second chapters aims to present the context and methodology of this work. The region of interest is first described as well as the study area considered here, followed by the main outline of the modelling sequence used is the present work. We then introduce the hydrodynamic model and the sediment dispersal methodology. We conclude this chapter by presenting and the defining the metrics used to assess the environmental impact.

2.1 Region of interest : the Northern Red Sea and the Gulf of Aqaba

The Red Sea is a unique body of water, characterized by its narrow and elongated shape, lying between Africa and the Arabian Peninsula, and spanning roughly over 20° of latitude, from 12°30'N to 30°N. It is a semi-enclosed basin, connected to the Indian Ocean through the Bab-el-Mandeb strait and the Gulf of Aden in its southernmost part (Fig. 2.1A). In the northern end, the Red Sea forms two gulfs, the Gulf of Aqaba in the East and the Gulf of Suez in the West, leading to the Suez canal (Fig. 2.1B). The latter connects the Red Sea and the Mediterranean Sea, thereby making the Red Sea one of the most heavily traveled waterways in the world, carrying maritime traffic between Europe and Asia. The waters of the Red Sea itself, too, are unique. These waters are characterised by very high surface temperatures coupled with extreme salinities, making it one of the hottest and saltiest seawater bodies in the world. The average depth of the Red Sea is 700 m and the main trough exceeds 1000 m everywhere, with a maximal depth of 3040 m (Edwards, 1987).

Up in the northernmost part of Red Sea, lies the Gulf of Aqaba (GoA). It is 180 km long, between 14 and 26 km wide, and has an average surface of 3300 km^2 (Ahmed et al., 2012). The GoA coastline is divided among four countries : Egypt, Israel, Jordan and Saudi Arabia, with the two major port cities, Aqaba (Jordan) and Eilat (Israel), located on the northern coast and separated only by a few kilometers. It is separated from the Northern Red Sea by the narrow and shallow Strait of Tiran (see location in Fig. 2.1B), which has a sill depth of 265 m. The GoA is part of the Syrian-African rift valley and displays non-regular seismic activity, as it is part of the Dead Sea Fault. The GoA is characterised by a succession of three pull-apart basins, which showcase important depth of more than 1000 m and a maximum gulf depth of 1777 m. The gulf is flanked by mountains and desert on both the east and west sides. The mountains reach 1000 m and more, only a few kilometers off the eastern and western coasts of the GoA. Given the narrowness of the gulf, this corresponds to a dramatic topographic change over a relatively

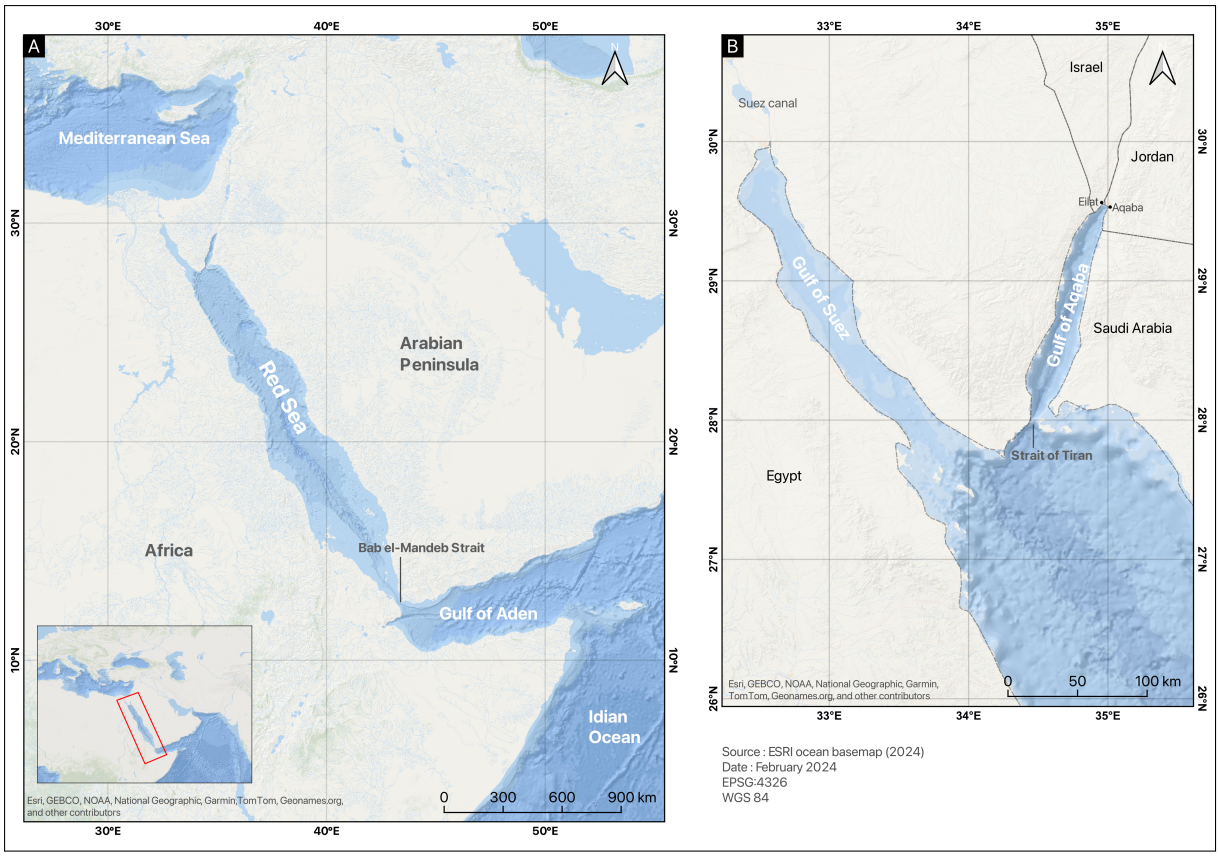

Figure 2.1: (A) The Red Sea and (B) the Northern Red Sea

short distance (Ribot et al., 2021).

2.1.1 Physical oceanography

The GoA climate is arid with an average net evaporation of 2 m/year and with no permanent rivers flowing into the gulf. As a result, GoA waters are among the most saline in the world. Throughout the year, the wind blows over 90% of the time from the North, which further enhances the evaporation and the resulting thermocline circulation (Ahmed et al., 2012). The consensual view of the general circulation of the Gulf of Aqaba corresponds to an inverse estuarine circulation, where, throughout the year, the net buoyancy loss due to large evaporation and heat loss drives the circulation, causing a northward flow of warm and low-salinity surface water from the Red Sea into the gulf. As the surface water flows northward, it becomes denser through cooling and evaporation. When the water reaches the northern end of the gulf, it sinks and returns to the Red Sea as a deep dense layer, out-flowing in the lower level of the Straits of Tiran (Klinker et al., 1976). However, the latter study was conducted on a short period during the winter months and used indirect methods (e.g. mass and heat flux balance), rather than actual measurements. Thus the seasonal variations in the flux exchange were not accounted for (Manasrah et al., 2019).

Biton and Gildor (2011a) ran an oceanic general circulation model (OGCM) for 15 years and showed that on a subannual time scale, the GoA circulation deviates from the inverse estuarine circulation. Based on temperature profiles observation and on model results from the latter authors, three layers characterising the GoA water column can be distinguished : (1) a deep and quasi stagnant layer, (2) the intermediate water, and (3) the surface water. The deep layer

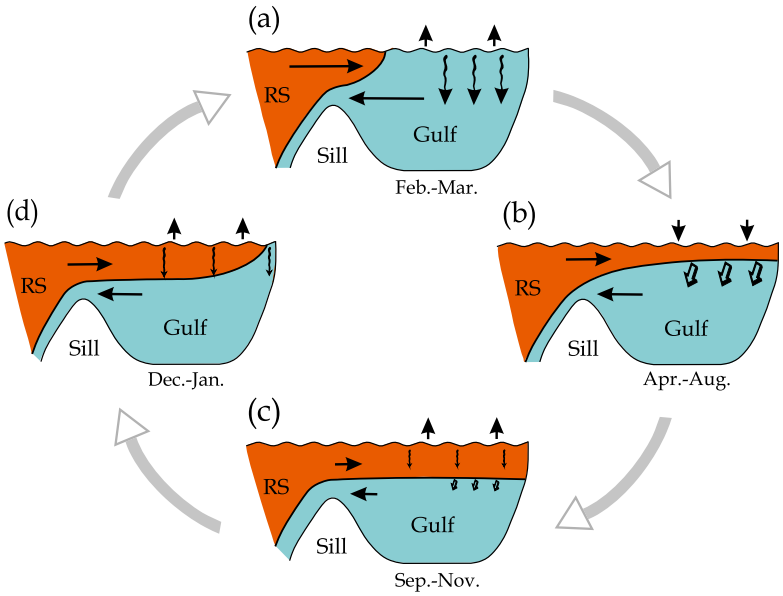

Figure 2.2: A schematic representation of different stages in the GoA seasonal evolution of the deep/intermediate water balance, including (a) the wintertime mixing conditions, when the intermediate water accumulates up to the surface (February–March); (b) the restratification period during April–August, when the intermediate water level is sinking relatively fast; (c) quasi-steady conditions in the intermediate water level/volume (September–November); and (d) the transition stage, when thermally driven vertical mixing creates a new intermediate water mass along the gulf (starting at the north). Retrieved from Biton and Gildor (2016).

is sligly colder than 21°C and fills the gulf below 600 m. The intermediate water temperature slowly increases from 21°C to 21.9°C and the surface layer has a temperature above 21.9°C. Unlike the deep water layer, the two upper layers are highly active and exhibit strong seasonal variability, with thermally driven deep mixing that occurs during February–March, followed by a restratification period between April and August (Fig. 2.2). During the restratification phase, the surface layer is rebuilt, increases its temperature and volume, and pushes the 21.9°C isotherm from the surface down to ~200 m. From September to December, the surface layer increases its volume at a much slower rate and the strong stratification starts to erode due to atmospheric cooling, until the surface layer is vertically mixed, and a relatively thin (stratified) layer separates the surface layer from intermediate water everywhere along the gulf. From January to March the surface layer is mixed with the intermediate layer almost completely and the sea surface temperature in mid-February is below 21.9°C in most places in the gulf. In severe winters the water column can mix down to ~700 m at the northernmost end of the gulf, where the deep water is formed via both open water convection and shelf convection (Biton and Gildor, 2011a). Additionally, the horizontal circulation of the GoA is characterized by a chain of eddies along its northward axis, as previously shown by both measurements and models (Biton and Gildor, 2011a, 2016).

The NRS circulation is of major importance as it plays a crucial role in the formation of Red Sea near-bottom water. Both the gulfs of Suez and Aqaba are the regular sources of the Red Sea near-bottom water. However, parts of the coastal areas over the far North of the basin may also contribute, though occasionally. The water masses out-flowing the gulfs are dense enough to sink following the lateral slope path reaching the bottom layers of the Red Sea (Papadopoulos

et al., 2015) and travel in a southwards direction, driven by the overturning circulation of the Red Sea (Yao et al., 2014).

The Red Sea surface circulation includes several cyclonic and anticyclonic gyres. A cyclonic gyre prevailing over the Northern Red Sea centered between 26°N and 27°N has been extensively documented (Papadopoulos et al., 2015). During winter under strong buoyancy forcing, this gyre uplifts deeper waters to intermediate depths and is responsible of producing two thirds of Red Sea out-flowing water (i.e. the water flowing out of the Red Sea to the Indian Ocean) (Sofianos and Johns, 2003).

2.1.2 Biological context

The Red Sea is a biodiversity hotspot, and the GoA is no exception. The gulf comprises some of the world's most biologically diverse ecosystems, home to tens of thousands of species, many of which remain undiscovered. Over 5% of scleractinian corals and 2.9% of fishes found in the GoA are endemic to the Red Sea (DiBattista et al., 2016). In Eilat, scleractinian coral species diversity and community structure show considerable spatial variability (Loya, 1972; Eyal et al., 2019). Depth zonation creates various zones that can be characterised based on the most abundant species for a given zone. However there is no clear border between zones, much overlap thus exist between them. *Stylophora pistillata* is the most abundant coral specie in the lagoon and reef flat zone whereas *Echinopora gemmacea* is more present in the (upper) fore-reef region Loya (1972). In a more broader way, the dominant habitat-building families of scleractinian corals found in the NRS are *Acroporidae, Pocilloporidae, Merulinidae*. Moreover, approximately 210 scleractinian hard coral species and 120 species of soft coral have been recorded in the GoA (Eyal et al., 2019). In addition to harboring some of the best-developed, northernmost, deepest, and scientifically important coral reefs on the planet, the GoA region contains other ecologically significant associated habitats, including mangrove forests, seagrass meadows, tropical saltmarshes, shallow lagoons, and reef flats (Hoegh-Guldberg et al., 2022).

2.2 Study area

Our study area covers the GoA and a small part of the NRS (Fig. 2.3). Various reasons led to this spatial restriction. First, as explained previously, both GoA and NRS corals are of interest given their exceptional thermal resistance. Hence, the study area covers the GoA as well as the northeastern part of the NRS. The southern limit of the study area is set by the location of NEOM's Oxagon project. The latter limit could be set further South as the NRS coral refuge extends down to a latitude of 24°N (Osman et al., 2018), but we chose to focus on this limited area to keep the model computationally tractable. A buffer distance is then added to minimize the influence of boundary conditions on the simulated currents. Finally, the study area is closed in the West by drawing a straight line from the southernmost part of the peninsula separating the two gulfs. Again, this choice is motivated by the aim to focus this work on the northern part of the coral refuge region. The study area has a surface of 11 650 km^2. Coastlines are provided by OpenStreetMap.

2.3 General approach

We will consider a biophysical modelling approach to assess the environmental impact of the NEOM project on marine ecosystems through sediment releases in the NRS and GoA. The

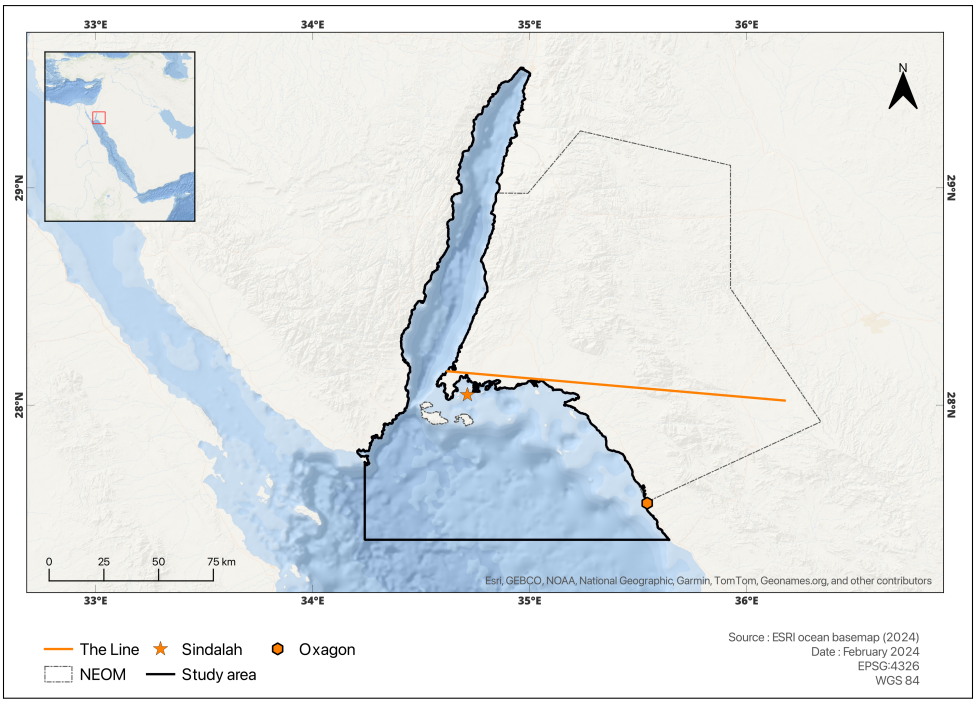

Figure 2.3: The study area includes the totality of the GoA and the northeastern part of the NRS. Three NEOM subproject lie within the study area, namely The Line, Oxagon and Sindalah.

ultimate goal of such a model is to provide outputs that can be leveraged to support decision-making to drive sustainable coastal development. The standard modelling sequence to produce the latter desired outputs can be summarized in three major steps and is described hereafter.

The modelling sequence first step consists in representing the hydrodynamics of the NRS and GoA. This requires the use of a 3D ocean model given the deep bathymetry and its steep slopes. Here, the 3D version of the multi-scale Second-generation Louvain-la-Neuve Ice-Ocean Model (SLIM) is used. SLIM is developed at UCLouvain and relies on the finite elements method to solve the ocean dynamics governing equations on an unstructured mesh. The nature of the unstructured mesh allows the resolution to be refined in areas of interest while keeping it coarser elsewhere. As such, computational resources are prioritarily allocated over coral reefs, along the coast and along steep bathymetry gradients, thereby effectively capturing the most complex dynamics. In the vertical, SLIM uses σ-layers to solve the aforementioned equations. Both the number and the width of the layers can be defined by the user to assure an optimal vertical resolution throughout the water column. The depth of the σ-layers is defined using a stretching function which allows a variable resolution with a higher resolution near the surface.

The second step uses dispersal models to represent the sediment dynamics. These models rely on Lagrangian particle tracking (LPT). The particles are forced by the currents computed in the previous step. Using these models, it is possible to study the trajectories the particles followed during a period of time. Other particles dispersal behaviours can be studied such as oil slick, plastic debris or, in this case, sediments resulting from coastal development sites. Here, various sediments will be released from the identified coastal development sites and will be tracked until they settle. It should be noted that, in this work, only the sediments resulting from coastal development areas that are transported by ocean currents are considered. Other potential major sources of pollution related to coastal development such as desalination plants brines or sewage plants discharge are relevant to study, but it is decided to ignore them for lack of time.

Finally, the last step involves the post-processing of the raw results. It is not a modelling

step strictly speaking but rather an analysis step of the raw outputs produced at the two previous steps. This step is specific to each application, there is thus no standard tool for this step. In a non-exhaustive way, for sediment dispersal, we can mention post-processing outputs such as dispersal pattern maps, sediment footprint, or risk maps.

2.4 Hydrodynamics

As mentioned before, we simulate the ocean circulation with the 3D version of the multi-scale Second-generation Louvain-la-Neuve Ice-Ocean Model (SLIM3D). Ocean currents and other variables such as temperature, salinity and surface elevation are computed by solving the ocean circulation governing equations under the hydrostatic and Boussinesq approximations on an unstructured mesh. This section aims to present and briefly describe the model equations (based on the work of Vallaeys (2018)) as well as its numerical implementation. The final 3D setup is presented and all the required forcings are then described. We conclude this section by describing the model validation procedure.

2.4.1 Mathematical model

SLIM3D solves the three-dimensional hydrostatic equations under the Boussinesq approximation on a domain Ω (Fig. 2.4). The vector position is defined as $\mathbf{x} = (x, y, z)$. The bottom boundary is located on the sea floor at $z = -h(x, y)$. The top surface is located at the moving surface elevation $z = \eta(t, x, y)$. The total water depth is thus $H(t, x, y) = h(x, y) + \eta(t, x, y)$.

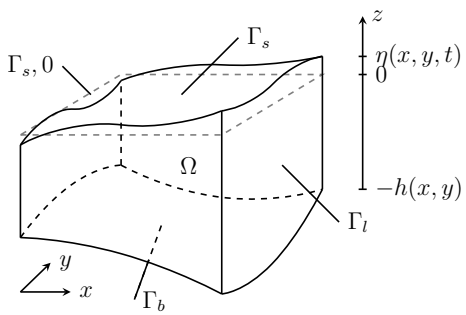

Figure 2.4: Sketch of the 3D domain Ω, where $h(x, y)$ is the bathymetry, $\eta(t, x, y)$ is the moving surface elevation, Γ_s is the moving top surface boundary, $\Gamma_s 0$ is the reference surface boundary, Γ_l and Γ_b are respectively the fixed lateral and bottom boundary (Delandmeter, 2017).

The hydrostatic hypothesis states that the vertical pressure gradient is equal to the weight of the water mass lying above. With the pressure $p(t, x, y, z)$ and the density $\rho(t, x, y, z)$ and under the hydrostatic hypothesis, the Navier-Stokes vertical momentum equation reduces to

$$\frac{\partial p}{\partial z} = -\rho g. \tag{2.1}$$

When integrating from z to η, it yields :

$$p = p_a + g\rho_0(\eta - z) + g\int_z^\eta (\rho - \rho_0)dz \tag{2.2}$$

where p_a is the atmospheric pressure, $\rho_0 = 1027\,kg/m^3$ is the constant reference seawater density and $\rho - \rho_0$ is the density deviation. The Boussinesq approximation implies that, since the density variation is much smaller than the reference density, i.e. $\rho - \rho_0 \ll \rho_0$, density variations can be neglected in all the terms of the momentum equation, except in the gravity one.

Five governing equations and one supplementary equation for the computation of the density are then solved by SLIM3D. The output is a temporal sequence of the six hydrodynamics variables: $\mathbf{u}(t,\mathbf{x})$ the horizontal velocity field [m.s^{-1}], $w(t,\mathbf{x})$ the vertical velocity component [m.s^{-1}], $\eta(x,y)$ the sea surface elevation [m], $S(t,\mathbf{x})$ the salinity [g.kg^{-1}], $T(t,\mathbf{x})$ the temperature [°C] and $p(t,\mathbf{x})$ the hydrostatic pressure [N.m^{-2}]. The model equations read :

$$\frac{\partial \mathbf{u}}{\partial t} + \nabla_h \cdot (\mathbf{u}\mathbf{u}) + \frac{\partial (w\mathbf{u})}{\partial z} = \nabla_h \cdot (\nu_h \nabla_h \mathbf{u}) + \frac{\partial}{\partial z}\left(\nu \frac{\partial \mathbf{u}}{\partial z}\right) - f\,\mathbf{e_z} \times \mathbf{u} - \frac{1}{\rho_0}\nabla_h p, \tag{2.3}$$

$$\nabla_h \cdot \mathbf{u} + \frac{\partial w}{\partial z} = 0, \tag{2.4}$$

$$\frac{\partial S}{\partial t} + \nabla_h \cdot (\mathbf{u}S) + \frac{\partial (wS)}{\partial z} = \nabla_h \cdot (\kappa_h \nabla_h S) + \frac{\partial}{\partial z}\left(\kappa \frac{\partial S}{\partial z}\right)(+S_{rel}), \tag{2.5}$$

$$\frac{\partial T}{\partial t} + \nabla_h \cdot (\mathbf{u}T) + \frac{\partial (wT)}{\partial z} = \nabla_h \cdot (\kappa_h \nabla_h T) + \frac{\partial}{\partial z}\left(\kappa \frac{\partial T}{\partial z}\right) + T_{rel} \tag{2.6}$$

where ∇_h is the horizontal gradient operator defined as

$$\nabla_h = \frac{\partial}{\partial x}\mathbf{e}_x + \frac{\partial}{\partial y}\mathbf{e}_y$$

and, $f = 2\Omega \sin\phi$ is the Coriolis factor [s^{-1}] with $\Omega = 7.29 \times 10^{-5}$ rad.s^{-1} and ϕ the latitude. The horizontal and vertical diffusivities are $\kappa_h(t,\mathbf{x})$ and $\kappa(t,\mathbf{x})$ and the horizontal and vertical eddy viscosities are $\nu_h(t,\mathbf{x})$ and $\nu(t,\mathbf{x})$. Closure schemes are necessary to take into account turbulent subscale processes that can not be explicitly represented by the model. The horizontal viscosity follows the Smagorinsky (1963) closure scheme:

$$\nu_h = \alpha \Delta^2 \sqrt{2\left(\frac{\partial u}{\partial x}\right) + 2\left(\frac{\partial v}{\partial y}\right) + \left(\frac{\partial u}{\partial y} + \frac{\partial v}{\partial x}\right)^2}, \tag{2.7}$$

where α is a non-dimensional constant and Δ^2 is the horizontal surface area of the 3D mesh element. The vertical eddy viscosity and diffusivity, ν and κ, on the other hand, are computed with the κ-ϵ turbulent closure model (Burchard et al., 1999; Kärnä et al., 2012)) with Canuto A stability functions (Canuto et al., 2001). Finally, the horizontal diffusivity κ_h is defined using the Okubo (1971) parameterization.

In equation 2.3, the horizontal pressure gradient is divided into its atmospheric, external and internal components:

$$\frac{1}{\rho_0}\nabla_h p = \frac{1}{\rho_0}\nabla_h p_a + g\nabla_h \eta + \frac{g}{\rho_0}\nabla_h \int_z^\eta (\hat{\rho}(S,T) - \rho_0)\,dz, \tag{2.8}$$

where $\hat{\rho}(S,T)$ is the density calculated with the state equations from Jackett et al. (2006).

The last terms of equations 2.5 and 2.6 are relaxation terms that are used to nudge the values to a reference salinity and temperature value provided by an OGCM such as Nucleus for European

Modelling of the Ocean (NEMO) for the salinity, or from remote sensing observations for the temperature. By default, the salinity nudging is disabled. On the other hand, the temperature relaxation is always enabled. The temperature surface boundary equation reads :

$$\kappa \frac{\partial T}{\partial z} = -(Q_{net} + Q_{pen} + Q_{nudg}), \tag{2.9}$$

where Q_{pen} is the heat flux that effectively penetrates the water surface, Q_{net} is the heat balance flux which considers both radiative and turbulent fluxes and Q_{nudg} is the additional heat flux that is imposed at the surface and is computed as

$$Q_{nudg} = T_{rel} = \frac{\Delta z_s (SST_{obs} - T)}{\tau_s}. \tag{2.10}$$

The temperature nudging is hence formulated as a surface heat flux that is applied entirely at the surface. Its characteristic time is defined by the relaxation period τ_s it is applied over a depth Δz_s.

The surface elevation $\eta(t, \mathbf{x})$ is computed from the model's external 2D mode relying on the depth-averaged velocity $\bar{\mathbf{u}}(t, x, y)$ given by the depth-averaged shallow water equations (SWE). The non-conservative SWE read:

$$\frac{\partial \eta}{\partial t} + \nabla_h \cdot (H\bar{\mathbf{u}}) = 0 \tag{2.11}$$

$$\frac{\partial \bar{\mathbf{u}}}{\partial t} + \bar{\mathbf{u}} \cdot \nabla_h \bar{\mathbf{u}} + f\mathbf{e}_z \times \bar{\mathbf{u}} = -g\nabla_h \eta + \frac{\nu}{H}\nabla_h \cdot (H\nabla_h \bar{\mathbf{u}}) + \frac{\tau_s - \tau_b}{\rho_0 H} \tag{2.12}$$

where

$$\bar{\mathbf{u}} = \frac{1}{H}\int_{-h}^{\eta} \mathbf{u}\, dz.$$

and τ_s and τ_b respectively denote surface and bottom stresses.

Boundaries conditions vary depending on the considered boundary. Closed lateral boundaries Γ_l (land barriers) are imposed to be impermeable:

$$\mathbf{u} \cdot \mathbf{n}_h = 0,$$

where $\mathbf{n}_h(x, y) = (n_x, n_y)$ is the horizontal unit vector normal to Γ_l. Top boundaries Γ_s and bottom boundaries Γ_b are also imposed to be impermeable:

$$w + \mathbf{u} \cdot \nabla_h h = 0, \quad \mathbf{x} \in \Gamma_b$$

$$w - \frac{\partial \eta}{\partial t} - \mathbf{u} \cdot \nabla_h \eta = 0, \quad \mathbf{x} \in \Gamma_s.$$

Boundary conditions on open lateral boundaries (open ocean) are defined by the outputs of other hydrodynamics models (e.g. NEMO).

2.4.2 Numerical model

The governing equations 2.3-2.6 are solved numerically using the discontinuous Galerkin (DG) finite element method on an unstructured mesh. The DG method combines the features of the classical finite element method (i.e. high-order accuracy) and the finite volume method (i.e. well suited for convection-dominant problems) and is applicable to complex geometries. The

DG method doesn't require the continuity of the solution between neighbouring elements, as each element is considered as a separate entity; for a mesh node between various elements, we consider that the solution takes a different value at each node, hence the discontinuity. In the DG method, the link between the elements is assured through a flux term.

Unstructured meshes have a variable resolution that can be increased near areas of interest, while kept coarser in other parts of the domain. Such meshes thus allow a better allocation of computational resources by increasing them where they are most needed. The use of parallel programming and high performance computing (HPC) resources is vital to reduce simulations times. The three-dimensional domain is divided into many subsets that are handled in parallel. While HPC and parallel programming greatly reduces computation times, increasing the resolution will still increase the complexity of the computations and thereby the computation time. It is thus necessary to find a balance between a good enough resolution that correctly captures the dynamics and a complexity that avoids excessive computational demands. Here, we use the latest version of SLIM that runs on GPUs.

The mesh is generated using GMSH (Geuzaine and Remacle, 2009) and its python wrapper. This library takes shapefiles as inputs to define tagged domain boundaries (e.g. closed or open boundaries). The first step consist of generating a 2D unstructured mesh which is latter extruded to obtain a 3D mesh. As mentioned in section 2.2, the domain is closed by two straight lines. The location of these lines depend on the distance between areas of interest such as Oxagon or the Strait of Tiran (see Fig. 2.3). For such areas of interest, the model must accurately represent currents. Therefore, it's vital to maintain a significant distance between these areas and the boundaries. This distance helps minimize the influence of external forcings applied at the boundaries on the simulated currents within the areas of interest. As the OGCM that is used to force SLIM has a resolution of approximately 8 km, a buffer distance of 15 km is added. Thus the southern boundary lies 15 km south from Oxagon. Here, the mesh resolution is increased near coastlines where the topography is more complex, near coral reefs since they are the object of this work and finally over areas where bathymetry gradients are important, such as the Strait of Tiran.

The 3D mesh is generated by extruding the 2D mesh along the vertical axis. This can be viewed as various 2D meshes lying on top of each other. The 2D triangular elements become triangular-based prism, corresponding to the 3D elements. The thickness of the 3D elements depends on the desired resolution. Generally, the prisms will be fine near the surface and their thickness will increase with depth. There are various vertical layer types that can be used to represent the bathymetry: z-layers, σ-layers, S-layers or hybrid z-σ-layers (Fig. 2.5). In the current SLIM3D implementation, only σ-layers and S-layers are supported. The z-layers offer computational stability as their primary advantage. However, their major drawback lies in the representation of bathymetry, which adopts a stair-like structure. On the other hand, σ-layers mitigate this weakness as they follow the domain's bathymetry and therefore represent it more accurately. While providing more accurate hydrodynamics, this second system is less computationally stable, especially when bathymetry gradients are important. S-layers (stretched) are σ-layers on which a stretching functions has been applied. S-layers suffer from the same computational instability, however, this can be mitigated by appropriately choosing the stretching function. Finally, the hybrid σ-z-layers combines the advantages of both approaches. Usually, σ-layers are placed at low depths where a good representation of the hydrodynamics is mandatory and z-layers take place deeper down to potentially reduce the number of elements at high depths, and to improve the stability of the setup.

As the σ-layers follow the bathymetry, the layers thickness is not fixed. This means that the nodes composing a vertical will not be at the same depth. In other words, the element's horizontal

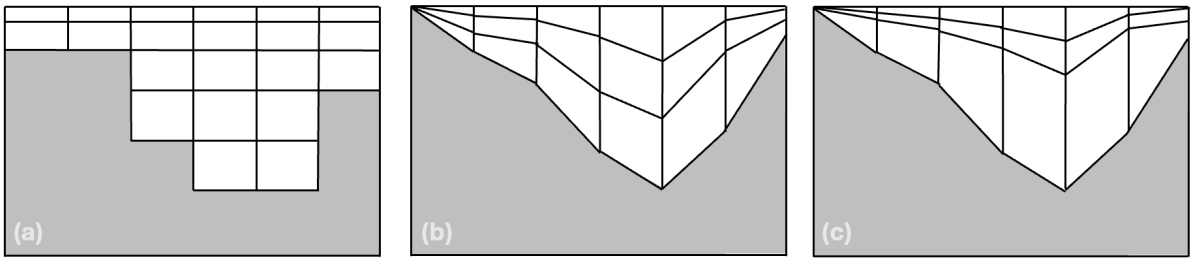

Figure 2.5: Schematic representation of various vertical layers type: (a) z-layers, (b) σ-layers and (c) S-layers. z-layers are placed at fixed level with (typically) a higher resolution close to the surface and showcase a stair-like bathymetry, whereas σ- and S-layers are bathymetry-following layers. The (fictive) stretching function applied here on (c) results in a higher resolution near the surface and a coarse resolution at the bottom.

surface is not necessarily flat. This leads to numerical issues, specially over areas where the bathymetry exhibits important variations. To avoid such numerical instabilities, Haney (1991) defined a criterion based on the mesh features :

$$\left|\frac{\sigma}{h}\frac{\partial h}{\partial x}\right|\Delta x < \Delta\sigma \quad \Leftrightarrow \quad \frac{\Delta h}{h} < \frac{\Delta\sigma}{\sigma}, \tag{2.13}$$

where $\sigma = z/h$ is the vertical coordinate in the σ-layer system, z is the vertical coordinate measured from the mean sea level reference (negative downwards), $\Delta\sigma$ is the vertical grid interval, Δx is the horizontal grid interval and Δh is the difference of bathymetry between two neighbouring nodes of the bottom layer. Practically this ensures that every node belonging to the depth layer z_i is located below (above) the neighbouring nodes from the depth layer just above z_{i-1} (below z_{i+1}). Over areas with important bathymetry gradients this criterion is respected by either small horizontal grid intervals (small 2D elements) or by coarse vertical resolution (few σ-layers).

Satisfying the Haney criterion is a sufficient condition to ensure a stable scheme, but it is not a necessary condition, meaning that the Haney criterion can be too restrictive. A less restrictive criterion is the Haidvogel one (Beckmann and Haidvogel, 1993) which defines a slope parameter r that is the ratio of the maximum local bathymetry change δh and the mean local bottom depth $\bar{h}$:

$$r = \frac{|\delta h|}{2\bar{h}} \qquad \text{with} \quad 0 < r < 1 \tag{2.14}$$

When using the Haidvogel criterion, the scheme stability increases when r approaches 0. A value of $r = 0$ represents a flat topography (i.e. there is no slope).

As the 3D mesh is created by extruding the 2D mesh, the latter can not be modified during the computations. Therefore, to respect either criterion, a pre-processing step during which the bathymetry is smoothed is needed. Consequently the bathymetry gradients are reduced, which impacts the quality of the resulting hydrodynamics. The degree of the bathymetry smoothing should allow a stable-enough setup while still being representative of the study area characteristics. Practically, the user sets the maximum value of r that is accepted over the domain, then the bathymetry is iteratively smoothed until $r < r_{max}$ is respected everywhere. Thus the user controls the degree to which the bathymetry is smoothed, for a given horizontal mesh resolution. Another consequence of the 2D vertical extrusion is that two 3D meshes are not necessarily alike. Indeed, as the sea surface elevation varies, the depth of the various layers will vary as well. Absolute layers thickness will increase/decrease when the sea surface height is higher/lower than the reference (the zero level), while relative layer width will be constant.

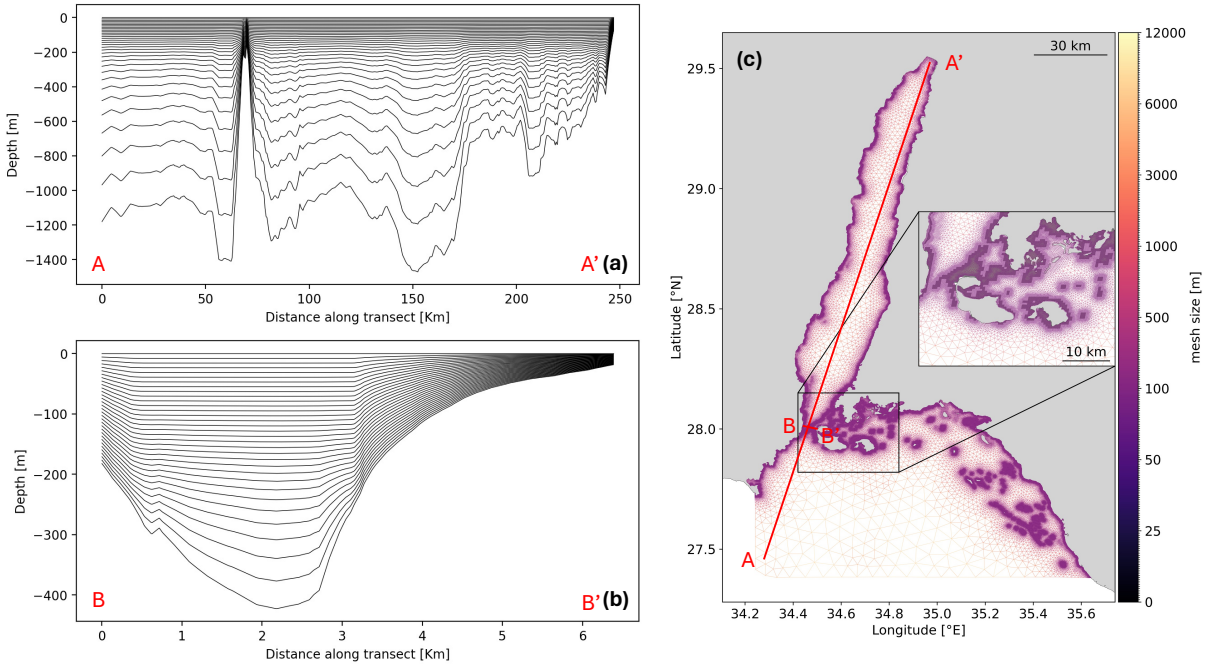

Figure 2.6: (a) Vertical transect across the domain from the lower-left corner, through the Strait of Tiran and up to the northern tip of the GoA and (b) vertical transect across the Strait of Tiran. (c) The 2D mesh used in this work. Note how the resolution greatly increases over coral reefs (see inlet).

2.4.3 Final 3D setup

The final 3D setup used in this work is composed of a 2D mesh of 1.76×10^5 elements with 32 vertical S-layers (Fig. 2.6), hence a total of 5.6×10^6 3D elements. The 2D mesh is refined over coral reefs, and along coastlines and bathymetry gradients. The maximal and minimal resolution are respectively 150 m and 12 km. The stretching function is the one described by Song and Haidvogel (1994) (refereed hereafter as the SH stretching). The stretching function's parameters are chosen so that the vertical layers are concentrated closer to the surface. Approximately half the number of layers are in the upper half of the domain. This allow to better capture the dynamics taking place at the surface. On the contrary, dynamics at the bottom of the domain are of lesser interest thus a coarser resolution is acceptable. The SH stretching functions is further discussed in appendix A.

The r_{max} value is fixed at 0.85. A relatively small value of r_{max} is mandatory considering the strong bathymetry gradients of the domain. Yet, this value is not extreme and allows to keep a representative bathymetry. Indeed, the maximum bathymetry difference from the resulting smoothing is approximately 750 m, but it is extremely localised. The mean smoothing is 38 m (see Fig. B.1 in appendix B). Moreover, to further ensure the setup stability, a maximal velocity threshold is applied on the horizontal velocities. This threshold has a value of 3 m/s. All velocities exceeding this value are clipped and set to 3 m/s.

We used a spin-up period of 38 days, starting on September 1st 2023. We assume the model yields representative values after this period. The hydrodynamics are modeled over 35 days, from October 8th to November 11th 2023. The model's output are exported on a hourly basis.

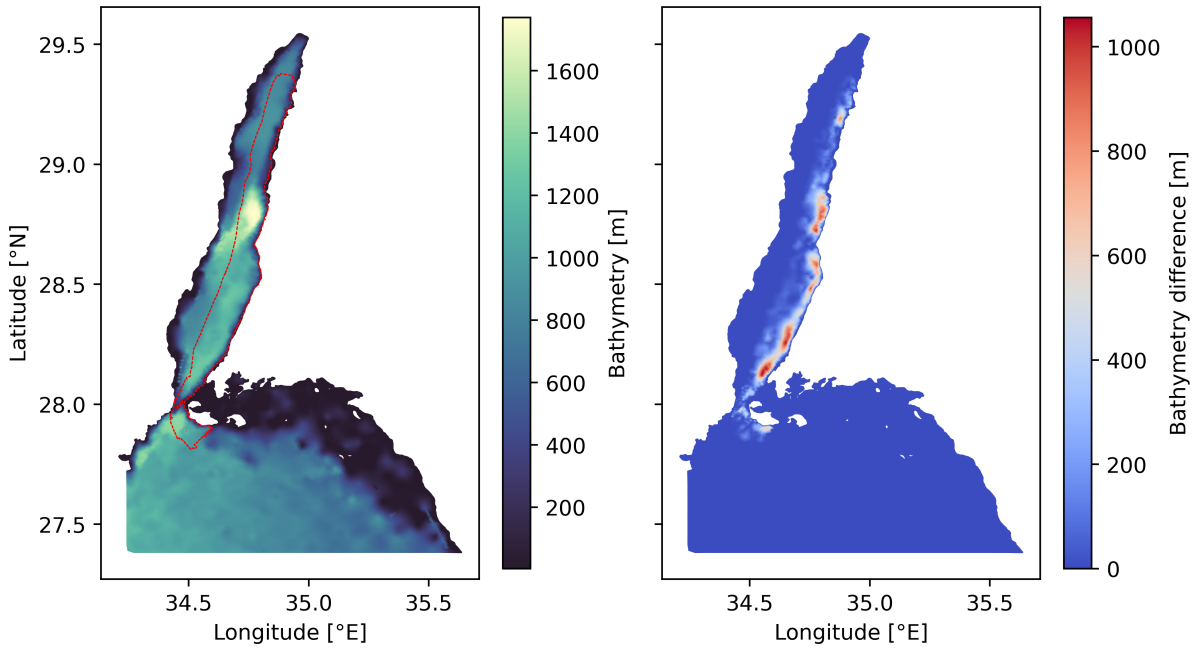

Figure 2.7: Merged bathymetry of the study area with the extent of the higher-resolution bathymetry provided by Ribot et al. (2021) (in red, left) and the bathymetry difference between the two data sources (GEBCO and Ribot et.al.'s DEM, right).

2.4.4 Forcing data

External forcings are the main drivers of water circulation. They are therefore essential to simulate realistic ocean currents. The hydrodynamic model requires both initial conditions and time-dependent boundary conditions to initialize and sustain the simulations effectively. Time-depending forcings are retrieved from different models and dataset which are presented hereafter.

The bathymetry is the only forcing with the coastline topography that is not time-dependent. In the present work, two bathymetry source are used. First, the General Bathymetric Chart of the Oceans (GEBCO), which has a resolution of 15 arc-seconds (~ 450 m) is used on the main part of the domain. Secondly, a Digital Elevation Model (DEM) of half of the GoA bathymetry with a 30 m horizontal grid resolution and a 1.5 m vertical resolution is used (Ribot et al., 2021)[1]. This DEM was produced from multibeam echo sounder measurement and covers the eastern half of the Gulf of Aqaba (within Saudi waters) and the Strait of Tiran. The two datasets have been merged (Fig. 2.7) using a buffer distance of 30 m along which a smooth transition from one dataset to the other is ensured. The buffer distance is relatively short in order to prioritize DEM data, as the bathymetry provided by GEBCO along Saudi shores is less accurate.

On the boundaries, the model is forced by large-scale ocean currents and tides. The tidal signal imposed on the boundaries is constructed from TPXO9 (Egbert and Erofeeva, 2002). Currents, temperature, salinity and sea surface temperature are retrieved from the global ocean model NEMO (Madec et al., 2023) which uses a regular 1/12° grid with 50 vertical layers. NEMO's outputs are available through the Copernicus Marine Environment Monitoring Service (CMEMS) interface[2]. Finally, wind, surface heat fluxes, precipitation and air temperature are retrieved from the ERA5 dataset (ECMWF Reanalysis 5^{th} Generation) produced by the European

[1]DEM bathymetric data is available at https://doi.org/10.5281/zenodo.4607639
[2]Copernicus Marine Service : https://marine.copernicus.eu

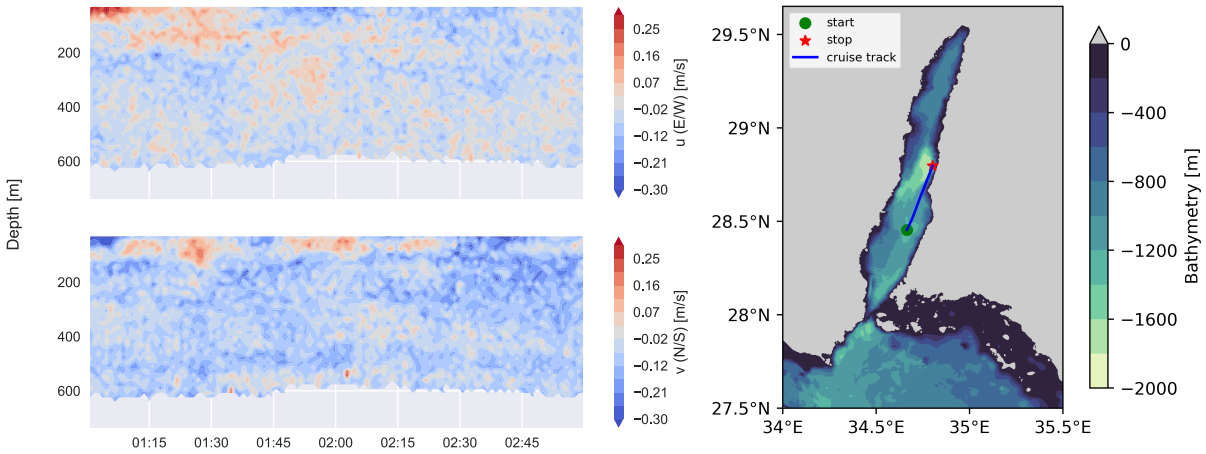

Figure 2.8: Example of ADCP data collected by the OceanX mission. The figure shows both northward and eastward velocity components (left) along the cruise track (right) for a 2h period (2020/10/20 1 AM – 3 AM). The data was pre- and post-processed using the tools provided by UHDAS+CODAS

Center for Medium-Range Weather Forecasts (ECMWF)[3]. ERA5 has a global coverage over a standard regular grid with a 31 km spatial resolution and an one hour temporal resolution.

2.4.5 Model validation

A key aspect of the modelling sequence is the validation step. This step is vital as it ensures that the model behaves correctly. It is however not sufficient to ensure that the model is accurate in all the area of interest. A key aspect of the present work is to leverage extensive *in-situ* data collected during two campaigns to thoroughly validate simulated ocean currents.

The validation dataset consists of Acoustic Doppler Current Profiler (ADCP) data that was measured during two fields campaigns on Oct. 6^{th} - Nov. 16^{th}, 2020, and Oct. 4^{th} - Oct. 22^{th}, 2023. The measurements were collected by one of the most advanced research vessel in the world, the OceanXplorer[4] within NEOM coastal waters (Fig. 2.8). Prof. Sam Purkis (UMiami) took part in that survey and granted us access to both datasets. ADCP sensors rely on the Doppler effect to measure the two components of the horizontal velocity along the water column. During the two surveys, two sensors were used : os75 operating as 75 kHz and wh300 operating at 300 kHz. The former has a temporal resolution of 1 minute and a spatial (vertical) resolution of 16 m while the latter has a temporal resolution of 5 minutes with a spatial resolution of 4 m. The frequency used has an impact on the maximum depth measurements. The os75 sensor has a large range and provides (coarse resolution) data up to 800 m, while wh300 has a smaller range and provides (fine resolution) data for depths less than 100 m.

The raw ADCP data must be pre- and post-prossed. This is done using the CODAS+UHDAS open-source software suite developed by the University of Hawaii's UH Currents Group[5]. During the pre-processing step, raw ADCP is converted into CODAS format which allows to use the software provided by the UH Currents Group. The final ADCP velocities are derived by subtracting the ship's speed, measured via GPS data, from the raw measured speeds. Raw GPS

[3]Copernicus Marine Environment Monitoring Service : https://www.ecmwf.int
[4]OceanX website : https://oceanx.org
[5]UH Currents Group : https://currents.soest.hawaii.edu

data undergoes calibration during the post-processing stage. Finally, any obvious erroneous data are manually removed.

As previously stated, GPS data is used to calculate the ship speed. An horizontal offset between the ADCP sensor and the GPS can cause errors in the calculated ocean velocity. This only occurs when the ship is maneuvering (i.e. turning) while underway. Slow speeds and "no turning" reduce the error. For this reason, we applied a mask on the ADCP data when the ship is maneuvering. The ship is considered as maneuvering when the heading difference between two successive measurements points is greater than 45°.

The vertical layers at which SLIM and ADCP data are available are different. To effectively compare both datasets, SLIM outputs have to be interpolated on the ADCP grid. SLIM output is linearly interpolated using the distance difference to the closest ADCP depth layer as weights.

2.5 Sediment dispersal

This section describes the transport model used to model the sediments plume dispersal, as well as the model's implementation. The release sites considered are presented, as well as the various sediment classes used in this work. Here, we used a similar approach as the one described in Saint-Amand et al. (2022).

2.5.1 Lagrangian Particle Tracker

The second step of the modelling sequence consists of simulating the dispersal of sediment plumes. This is achieved by using a Lagrangian Particle Tracker (LPT) which is integrated in SLIM3D. The LPT uses the simulated velocity fields resulting from the hydrodynamic model output to transport virtual the particles. All released particles trajectories are tracked during the simulation duration, until they settle.

The three-dimensional position of the particles is computed with an advection-diffusion equation in Lagrangian form :

$$d\mathbf{X}(t) = (\mathbf{u} + \nabla \cdot \mathbf{K})dt + \sqrt{2\mathbf{K}dt} \cdot \mathbf{R}(t), \tag{2.15}$$

where $\mathbf{X}(t)$ is the time-dependent 3D position vector of the particles, $\mathbf{u}$ is the total particle velocity, $\mathbf{R}(t)$ is a Brownian motion and $\mathbf{K}$ is the diffusivity coefficient described as a diagonal diffusivity tensor:

$$\mathbf{K} = \begin{bmatrix} \kappa_h & 0 & 0 \\ 0 & \kappa_h & 0 \\ 0 & 0 & \kappa \end{bmatrix}. \tag{2.16}$$

The first term on the right hand side of equation 2.15 is the deterministic part and represents the advection, whereas the second term is the stochastic part and represents the diffusion. The particles experience a random displacement of average size $\sqrt{2\mathbf{K}dt}$, which is caused by the ocean turbulent diffusion. The term $\nabla \cdot \mathbf{K}$ is added to the deterministic part as the turbulent diffusivity $\mathbf{K}$ is spatially highly variable. This ensures that the mean drift of particles is taken into account and prevents them to accumulate in regions of low diffusivity (Gräwe and Wolff, 2010).

Equation 2.15 is solved using a 4th order explicit Runge-Kutta (RK4) scheme. The Runge-Kutta scheme approximates the solution at time step t as the weighted average of four preliminary estimates. This is particularly convenient to correctly account for the curvature of the velocity

field, which is a non-negligible feature. The horizontal diffusion is computed using the Okubo parametrisation while the vertical diffusion is approximated using a first order Euler forward scheme. After computing the deterministic displacement, the stochastic displacement resulting from both the horizontal and vertical diffusion are added.

The total velocity $\mathbf{u}$ is the sum of the currents velocities and the particles velocities :

$$\mathbf{u} = \mathbf{u}_{curr} + \mathbf{w}_s. \tag{2.17}$$

The settling velocity is only defined in the vertical direction $\mathbf{w}_s = [0, 0, -w_s]$, where the non zero component is computed from an empirical formula described in the Particle Transport Model developed by the US Army Corps of Engineers (MacDonald et al., 2006), who adapted Soulsby (1997)'s settling velocity equation for extremely fine grains sizes :

$$\frac{w_s D}{\nu} = \begin{cases} \sqrt{107.33 + 1.049 D_{gr}^3} - 10.46 & D_{gr} \geq 0.672 \\ 0.0077 D_{gr}^2 & D_{gr} < 0.672, \end{cases} \tag{2.18}$$

where ν [m^2/s] is the kinematic viscosity, D [m] is the sediment grain size and $D_{gr}[-]$ is the dimensionless grain size defined as

$$D_{gr} = d \left(\frac{g(s-1)}{\nu^2} \right)^{1/3} \quad \text{with} \quad s = \rho_s / \rho \tag{2.19}$$

with ρ [kg/m^3] the mean seawater density, ρ_s [kg/m^3] the sediment density and d [m] the sediment diameter. The sediment density is computed following the relation between the mean grain size and density for continental terrace sediments from Hamilton and Bachman (1982) :

$$\rho_s = \left(2.374 - 0.175\phi + 0.008\phi^2 \right) 10^3 \quad \text{with} \quad \phi = -\log_2 d \tag{2.20}$$

where d is expressed in mm and 10^3 is a conversion factor.

2.5.2 Particles dispersal

As the dispersion potential of sediments depends on the particles sizes, various particles diameters were considered and range from 2 to 125 µm. The particles size were divided into four classes: coarse clay and very fine silt (2-8 µm), fine and medium silt (8-32 µm), coarse silt (32-64 µm) and very fine sand (64-125 µm). The classes are constructed by combining adjacent categories from the grain size scale established by Wentworth (1922).

Particles are released from Sindalah and Oxagon, which are sites where dredging recently occurred or is planned in the future. In fact, Sindalah is planned to open later this year (NEOM, 2024a). Particles were released inside a 200 m buffer zone surrounding Sindalah island and at a maximal distance of 400 m from Oxagon into the Red Sea, and along a distance of 700 m in both north and south direction. All particles were released at the water surface. Particles were continuously released at an hourly rate for two weeks, starting on October 10$^{\text{th}}$ 2023. The particles were then tracked for 17 extra days after the last release. Twenty distinct simulations were ran for each sediment class, during which particles diameters were randomly sampled from an uniform distribution. This amounts to a total of $\sim 2.42 \times 10^6$ tracked particles.

Particles were tracked for 31 consecutive days, from the moment they were released until they settled, with a time step of 200 s. We used a simplified sediment model that considered

only deposition, excluding resuspension, erosion, potential eolian transport, and other factors. In the current LPT implementation, a particle was considered as settled when the particle's depth was greater or equal to the bathymetry at the particle's position and was directly removed from the tracker. Hence, the correctness of the settlement dynamics depends on the bathymetry data used in the hydrodynamic model, described in section 2.4.4. The simulation scenarios that were considered are simplified ones, as they do not represent the complex nature of dredging projects that involves several vessels and different sediment release dynamics.

2.6 Environmental impact assessment

The environmental impact of the sediment plumes is assessed using various metrics, all of which are presented in the following section. All the metrics use a regular grid covering the whole computational domain.

2.6.1 Sediment footprints

The cumulative sediment densities are computed over a regular grid of 250 m of resolution throughout the simulation, following the approach of Saint-Amand et al. (2022). The cumulative densities correspond to the cumulative sum of of the number of particles inside each grid cell at each time step. From these cumulative densities, footprint maps are derived for each sediment class. The sediment footprints represent the extent reached by the sediment plumes in a given time. This extent is computed from the density grids by keeping all the cells visited by a minimum of 1000 sediment particles. This minimal value is chosen to reject all the grid cells that were not visited by enough particles and are thus non-representative, without being too restrictive to avoid rejecting meaningful data. The minimal threshold value was determined through an iterative process.

Sediment footprints are computed on a weekly basis, during the first four weeks of the simulation. We chose to ignore the first three days of the fifth week, as extrapolating the footprint to a full week using only the first three days is not representative, whereas neglecting these extra days resolves this issue. Due to the cumulative nature of the densities, the same particle can be counted multiple times in a single cell if it stays on the same cell during several consecutive time steps. The footprint thus takes into account the duration of the exposure and therefore the severity of the impact. Lastly, the footprint computations only includes the sediment particles that are suspended in the water column.

2.6.2 Plume frequency

The sediment plume frequency uses the same grid as the one used for the sediment footprints. Here, we used the approach described by Dobbelaere et al. (2024). The plume frequency is computed for each sediment class by counting all the grid cells that intersect with a particle trajectory for all time steps during a given day, and then dividing by the total number of simulated days. In that way, we count the number of days during which sediment plumes occurred over all grid cells. Additionally, the plume frequency allows us to discriminate the most frequents particles trajectory and hence the main dispersal patterns. Similarly to the sediment footprints, the sediment plume frequency only considers the particles that are suspended in the water column.

A major drawback of the way sediment footprints are expressed is that they cannot quantitatively measure the potential impact nor the severity caused by the temporal accumulation of

the sediment plumes. However, the plume frequency indicator addresses this issue by taking temporal accumulation into account.

2.6.3 Turbidity and deposition indicators

Similarly to the first two metrics, the turbidity and deposition indicators use the regular grid to count the number of particles in each grid cell, following the methodology of Dobbelaere et al. (2024). The turbidity and deposition are derived from the cumulative concentration of suspended and sedimented particles, respectively. At each time step of the simulation, the number of suspended and settled particles are counted within each grid cell. The cumulative concentrations are then obtained by computing the sum over all the time steps, which are then normalized by the total number of time steps and the number of released particles. The resulting normalized indicators are thus time-independent.

With n_t time steps, $p_{tot,c}$ the total number of released particles for the sediment class c and $p_c^{i,j}$ the number of suspended or sedimented particles in a grid cell located on row i and column j, the normalized indicator is defined as :

$$\text{indicator} = 16\frac{\sum_{t=1}^{n_t} p_c^{i,j}}{n_t\, p_{tot,c}}, \tag{2.21}$$

where 16 is a conversion factor to express the indicator in km^{-2}.

The normalized turbidity and deposition indicators respectively represent the average mass fraction of released particles that are in suspension in the water column and that have settled in each grid cell, expressed in km^{-2}. A higher indicator value represents a larger turbidity or deposition, which in turn indicates a higher impact.

2.6.4 Total turbidity exposure

The exposure of the coral reefs to the total turbidity is assessed. First, the total normalized turbidity indicator is computed as the sum of the normalized turbidity indicator of each sediment class. It is then normalized by dividing it by its 99th percentile. Given that we use a cumulative sum to compute the normalized turbidity indicator, some grid cells will have a value higher than 1, corresponding to locations where the value is higher than the 99th percentile. Such cell values are adjusted and cropped to 1. The total normalized turbidity indicator is computed as:

$$\text{Total turbidity} = \frac{\sum_{c=1}^{n_c} turbidity_c}{q_{99}}, \tag{2.22}$$

where $turbidity_c$ is the normalized turbidity indicator for the sediment class c computed using 2.21, n_c is the number of sediment classes and q_{99} is the 99th percentile. High total turbidity values indicate greater exposure to suspended particles across all sediment classes

Finally, the risk was intersected with the coral reefs layer from the United Nations Environment Program - World Conservation Monitoring Centre[6] (UNEP-WCMC) Global Distribution of Coral Reefs dataset (UNEP-WCMC et al., 2021) to exclusively highlight coral's sediment exposure. This layer only considers shallow corals. Hence mesophotic corals are not considered here.

[6] https://data.unep-wcmc.org

Chapter 3

Results

This chapter presents the results regarding the three steps of the modelling sequence. First, the outputs of the three-dimensional hydrodynamic model are presented. The results of the sediment plumes dispersal are then displayed. We conclude this chapter by addressing the results of the environmental impact assessment. In this section we will refer to animations for additional visual support which are available at `https://github.com/mattiasve/master-thesis-gifs.git`.

3.1 Hydrodynamic model

3.1.1 Validation

We used the 2023 OceanX ADCP dataset to carry out the validation. Within this dataset, we identified two periods during which the ship executed only a limited number of maneuvers. The first period start on Oct. 16th 5 AM and ends on Oct. 19th 6 AM. The second period spans from Oct. 20th 12 PM until Oct 22th 4:30 AM (see Fig. C.1). We purposely divided the validation into two periods due to the significant amount of unreliable data in the interval between them. Our ocean circulation model was validated with respect to currents magnitude and direction. Note that the surface layer is never considered here as the minimal depth of ADCP sensors are -16 m and -32 m for wh300 and os75, respectively (see section 2.4.5 for the temporal and spatial resolution of these sensors).

Figures 3.1 and 3.2 respectively show the spatial distribution of the error for the first and second validation period. We observe that the largest errors are well distributed throughout the water column. Current norm errors exceeding 0.15 m/s can occur at the surface, where the 3D mesh vertical resolution is the highest, as well as deeper in the water column. Errors of such magnitude are however a minority. The errors regarding the current direction are more contrasted. Some locations show minimal error over the whole water column while other

Table 3.1: RMSE between model results and measurements from both ADCP sensor and for the two validation periods considered in 2023.

	RMSE os75		**RMSE wh300**	
Validation period	Oct. 16-19	Oct. 20-22	Oct. 16-19	Oct. 20-22
current norm [m/s]	0.0946	0.0899	0.0915	0.0929
current direction [°]	135.62	148.52	121.69	144.86

locations show the opposite. Current norm and direction errors don't seem to be related as large current norm errors occur where current direction errors are minimal. Overall, our model results agree well with the current norm observations with RMSE values varying close to 9 cm/s, but performs poorly against current direction observations with RMSE values ranging between 121° and 148° (Table 3.1). Given this important error, all following results should therefore be carefully considered.

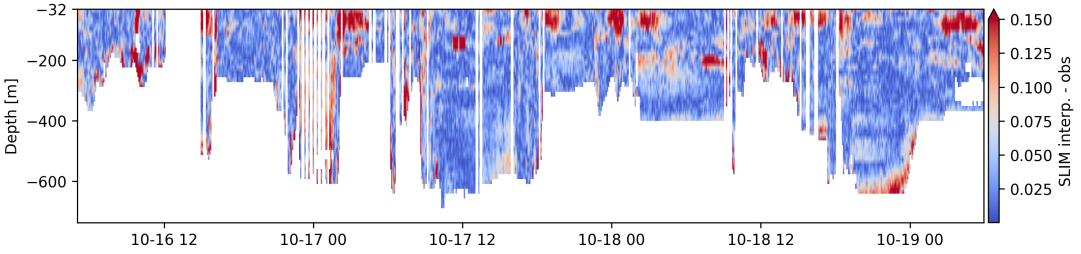

(a) Current norm difference from os75 in m/s

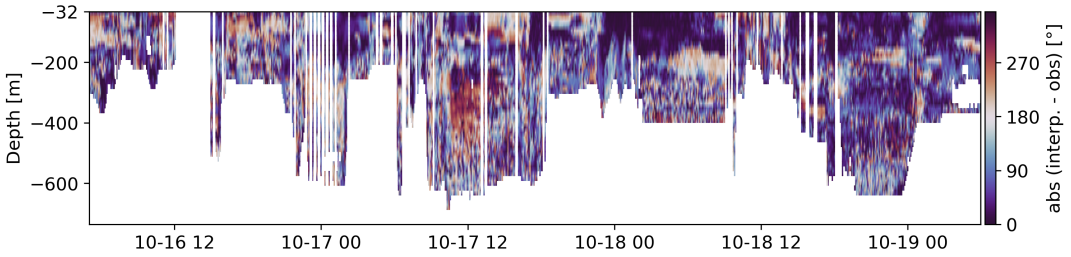

(b) Current direction difference from os75

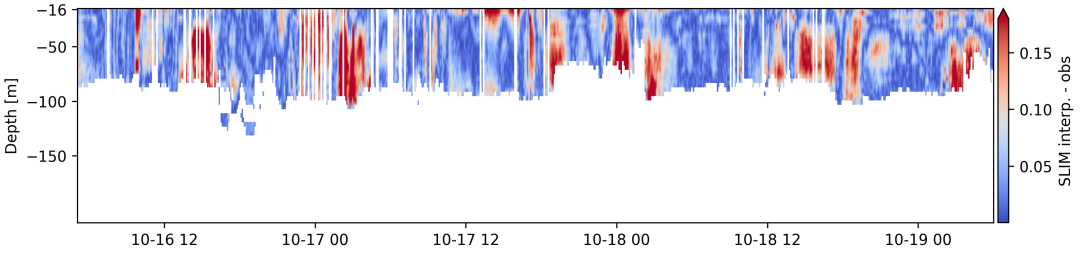

(c) Current norm difference from wh300 in m/s

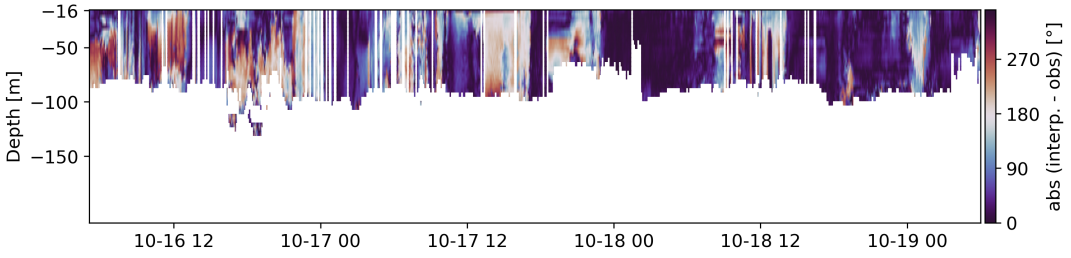

(d) Current direction difference from wh300

Figure 3.1: Spatial distribution (along the cruise track) of the current norm and direction difference between observations (ADCP data) and interpolated SLIM values, for the two ADCP sensors, between 2023/10/16 5 AM and 2023/10/19 6 AM. For the current norm, the maximum displayed value corresponds to the 95th percentile of the error values with respect to each sensor. For the current direction, the values are cyclic. An error of 0° is equivalent to an error of 360° and is represented by the cyclic colormap. Vertical black spaces corresponds to locations where the mask was applied. Full comparison figures are presented in Appendix C.

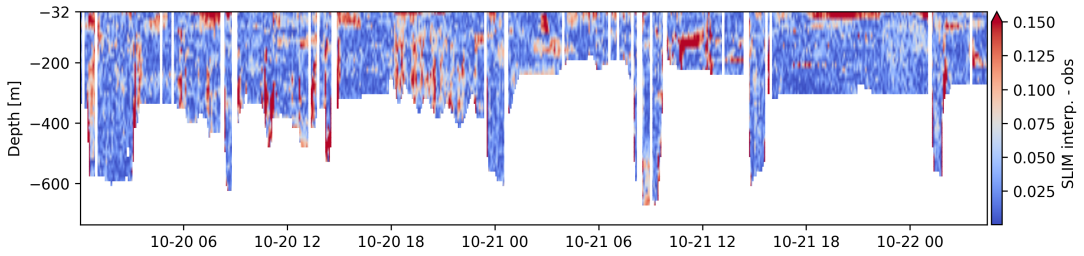

(a) Current norm difference from os75 in m/s

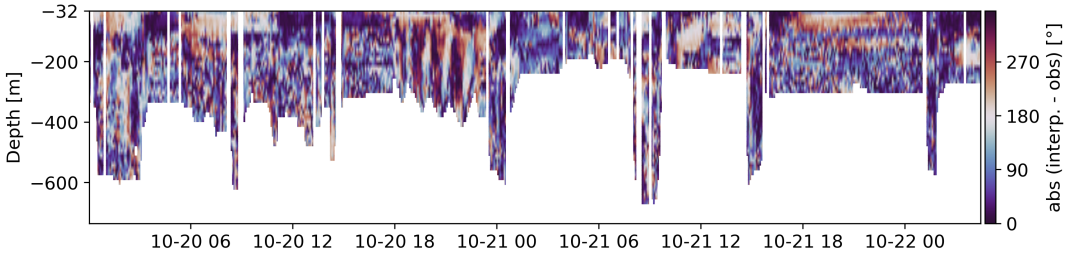

(b) Current direction difference from os75

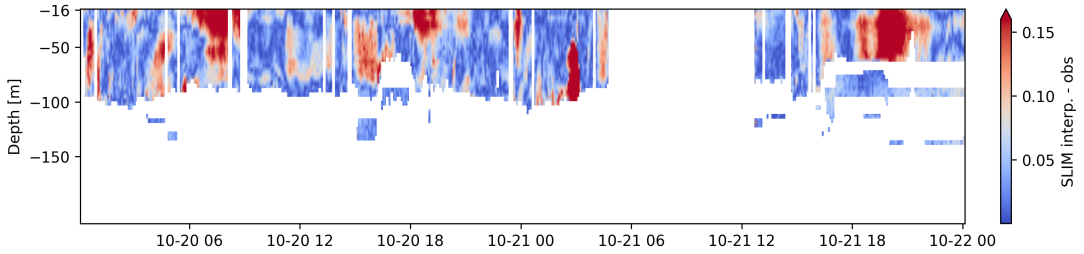

(c) Current norm difference from wh300 in m/s

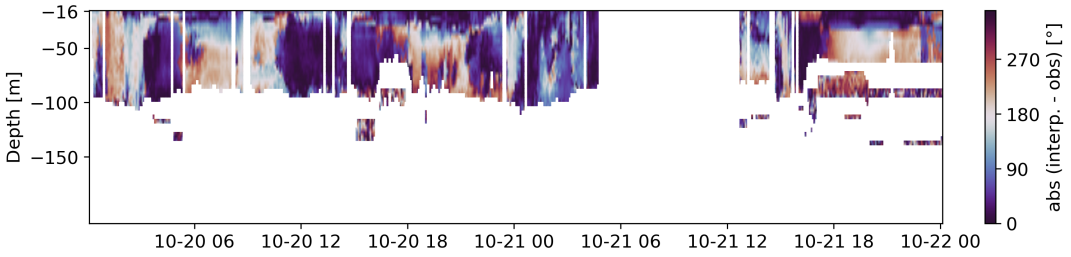

(d) Current direction difference from wh300

Figure 3.2: Spatial distribution (along the cruise track) of the current norm and direction difference between observations (ADCP data) and interpolated SLIM values, for the two ADCP sensors, between 2023/10/20 12PM and 2023/10/22 04:30 AM. The big blank in (c) and (d) corresponds to the moment during which the sensor was turned-off.

3.1.2 Salinity and temperature profiles

The temperature profile in the north of the GoA shows that the temperature is stable through time while the salinity displays more variation (Fig. 3.3). These variations are the strongest near the surface for both profiles. For the salinity, the magnitude of the variation reduces with depth and are constant throughout the water column for the temperature. Based on these profile, we clearly identify the shallow layer which is warm and fresh with a depth less than 10 m. There is an intermediate mixed layer between 10 m and 150 m where temperature and salinity are somewhat constant. Both profile then follow a slight slope until 400 m where they are almost constant, corresponding to the deep layer.

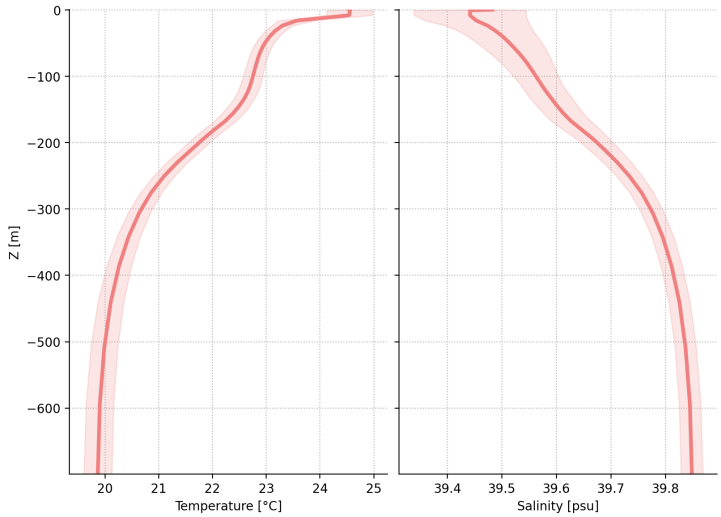

Figure 3.3: 34 days mean temperature and salinity profile approximately 10 km off the northern coast of the GoA (29.45 °N 34.98 °E). The shaded area corresponds to the standard deviation.

The temperature and salinity vertical transects show that the domain is stratified and that it is composed of two water masses separated by the Strait of Tiran (Fig. 3.4). The NRS surface layer is warm with temperature values of ~ 28 °C and relatively fresh, showcasing the lowest salinity values over the whole domain with 38.5 psu. Below 200 m, the NRS water is relatively warm with a constant value of ~ 22 °C until the sea floor. This deep water has high salinity values of 40 psu and more. The surface and deep layer are separated by a relatively shallow mixed layer of approximately 150 m width. Compared to the NRS, the GoA is less stratified and its surface layer is colder, with values of ~ 24 °C and is less saline as well. Temperatures below 400 m are colder than ~ 21 °C and the salinity is roughly constant below 200 m.

After computing the daily mean of a vertical transect across the GoA, we observe that the isotherms tend to deepen throughout the simulated period (Fig. 3.5). This is particularly true for the 21.1 isotherm which deepens approximately 100 m over the considered period. The 21.9 isotherm shows a similar pattern but with less variation. The latter displays a depth difference of roughly 50 m. These two isotherms are of particular interest as they respectively delimit the upper limit of the deep and intermediate layer. The isotherms depth difference reduces as the isotherm's value increases, as showcased by the isotherms located in the surface layer (i.e. >21.9 °C). This variation is particularly visible on the hourly vertical transect animation for the temperature. We recommend the reader to consult this animations[1].

Moreover, the model outputs show the presence of horizontal surface gradients in both temperature and salinity across the GoA. The thermal gradient is negative: the SST decreases from south to north. This gradient is particularly strong in the first half of the gulf and weaker in the second half. On the contrary, the saline gradient is positive from south to north and is more homogeneous along the gulf length. Additionally, note that the surface water temperature is generally colder on the eastern shore as well. The respective animations[2] show that both gradients are maintained throughout the whole simulated period, with the thermal one decreasing slightly.

[1]The vertical animation is available here
[2]The horizontal animations are available here

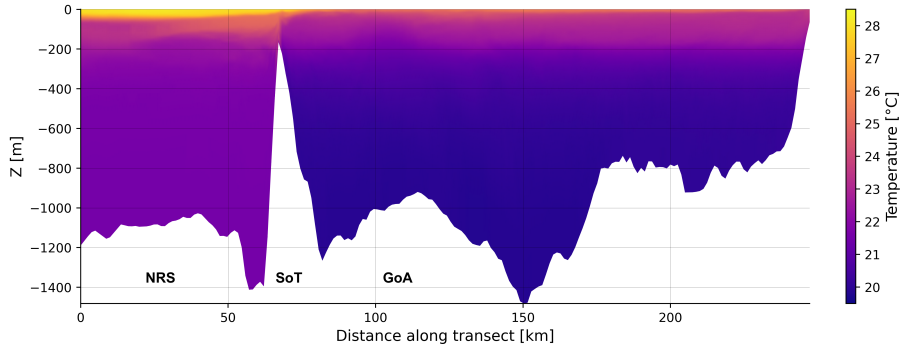

(a) Temperature

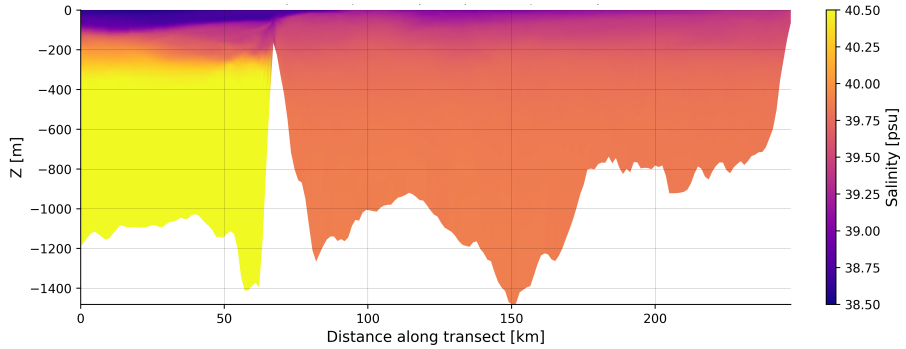

(b) Salinity

Figure 3.4: Tracers vertical transect across the domain from the NRS, through the Strait of Tiran (SoT), to the tip of of the GoA on 2023/11/04 at 12 PM. The NRS and GoA water masses are separated by the SoT.

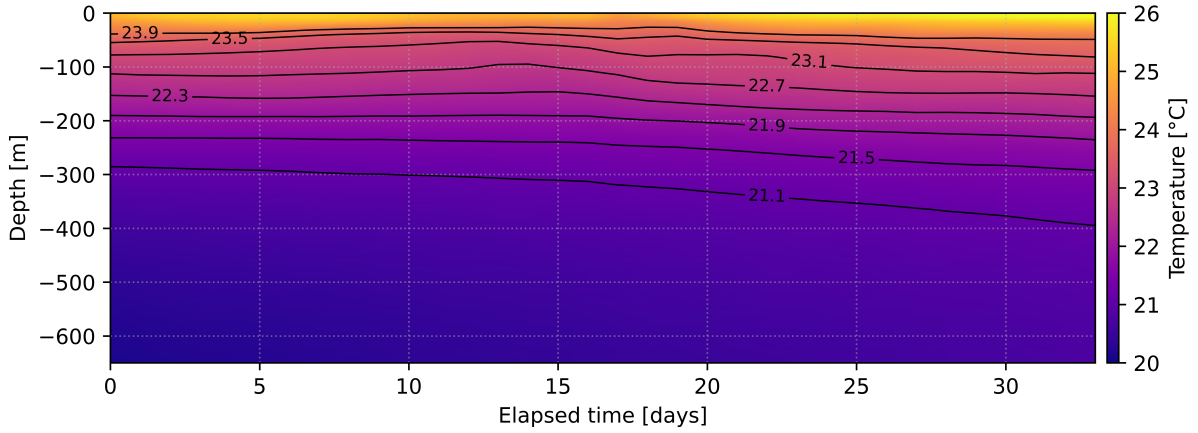

Figure 3.5: Daily average of a vertical transect along the center axis of the GoA for all the simulated days showing the evolution of the thermal stratification. The depth is cropped at - 650 m.

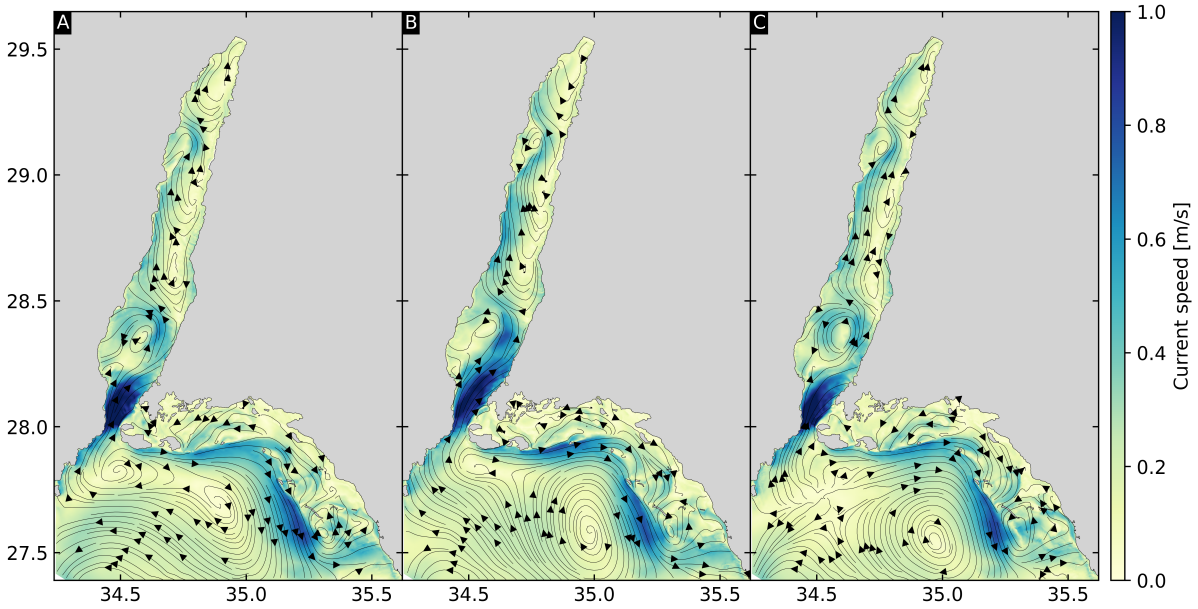

Figure 3.6: Surface velocity magnitude and streamlines snapshots over the whole domain on 2023/11/10 at (A) 11 AM, (B) 5 PM and (C) 11 PM. The main surface dynamics are constant through time and do not vary greatly.

3.1.3 Current dynamics

The surface current dynamics of the domain display particular features and do not vary much, the main features are constant through time (Fig. 3.6). A gyre is present in the NRS and covers most of the width of the domain. This gyre features important velocities that reach approximately 1 m/s on the north where the currents follow the isobath between the shallow shelf and the deeper part, as well as on the eastern side. In the center of the gyre, velocities values are relatively weak. The gyre is however limited to the offshore region. Along the Saudi coastlines, the currents are more turbulent. In the GoA, we observe various eddies along the gulf. The main one is located north of the Strait of Tiran. Smaller eddies can be observed further north as well, notably around 28.6 °N and 29.2 °N. The strongest currents take place on the Strait of Tiran, where they reach values of 1 m/s over a large area. These strong currents then weaken as they progress northward and merge into the main gyre, after which they head to the western coast of the GoA.

Secondly, the weekly zonal surface current average better highlights the smaller scale coastal processes and shows that we can clearly differentiate the coastal currents from the NRS gyre (Fig. 3.7). These coastal currents are weaker than those in the gyre, except along Oxagon where mean current values reach 0.6 m/s, approaching the range of values observed in the NRS gyre. Along Oxagon, coastal current flow northward while further north on the coastlines they flow southward (Fig. 3.7b). These opposing currents then meet halfway and merge into the NRS gyre. Coastal currents east of Sindalah flow westward before merging into the northern part of the NRS gyre (Fig. 3.7a). On the west side of the island, the intense currents from the gyre are deflected by the island located at 27.95°N 34.7°E. The defected currents flow towards the GoA where they merge into the extremely intense currents in the Strait of Tiran.

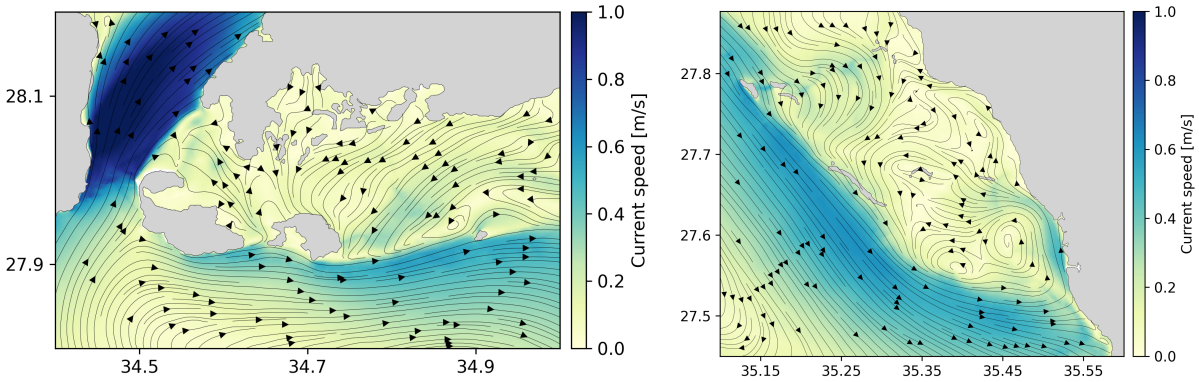

(a) Strait of Tiran and Sindalah

(b) Oxagon

Figure 3.7: 7 days average (2023/11/03 - 2023/11/10) surface current velocity and streamlines for two NEOM projects displaying the main zonal current pattern.

3.1.4 Exchange flow in the Strait of Tiran

Similarly to the GoA, the exchange flow in the Strait of Tiran is stratified and is composed of two water masses. The surface water mass corresponds the inflowing NRS water which is warm and saline, while the outflowing water mass correspond to the cold and saline GoA intermediate water (Fig. 3.8). As mentioned previously, the 21.9 °C isotherm delimits the two upper layers (Fig. 3.4a). A bottom layer located at roughly −300 m can be observed as well. This layer corresponds to the deep water layer of the GoA. As the maximum sill depth of the Strait of Tiran is of about 265 m, it is likely that this layer has a minor influence in the exchange flow. Figure 3.9 shows that, for the upper 200 m, the GoA water is always denser than the NRS water, and hence the exchange flow across the strait is indeed always composed of two layers. Below 200 m, the contrary is observed. However, the exchange flow direction switches direction only from −300 m (Fig. 3.8d). Thus, a third layer could potentially take place in the exchange flow between −200 m and−265 m but is only begins to appear deeper in the water (i.e below the strait sill).

The surface layer current flowing into the GoA is intense in the first 40 m and weak in the following 10 m as the current direction begins to switch from north to south. Note that at −50 m of depth and on the first kilometer from the western shore the currents flow in a southeast-ward. Moreover, the majority of the two-layer exchange flow takes place on the western half of the strait since the eastern half is more shallow. Below 60 m and until 250 m, the exchange flow is relatively intense, with velocity values between 0.5 - 0.6 m/s in the direction of the NRS. The velocity norm and streamlines over the Strait of Tiran for various depths are presented in Appendix D.

3.2 Sediment plumes dispersal

The sediment footprints display a clear difference between fine sediments (<32 µm) and coarser ones (Fig. 3.10). Fine sediments can travel far into the GoA. After four weeks, some of these particles traveled ~ 200 km north into the gulf. Coarse clays and very fine silts (2-8 µm) have the potential to reach the northernmost part of the GoA and are mostly found on the eastern part of the gulf and much less along the western coast. Fine and medium silts (8-32 µm), however, are exclusively found on the eastern coast and can reach the northernmost tip of the GoA, but not

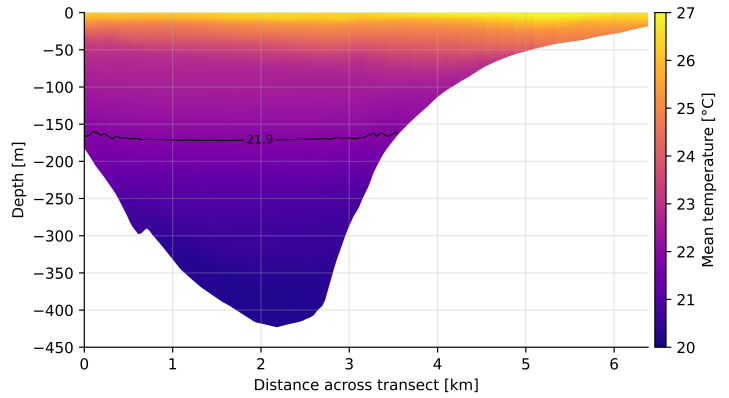

(a) Temperature

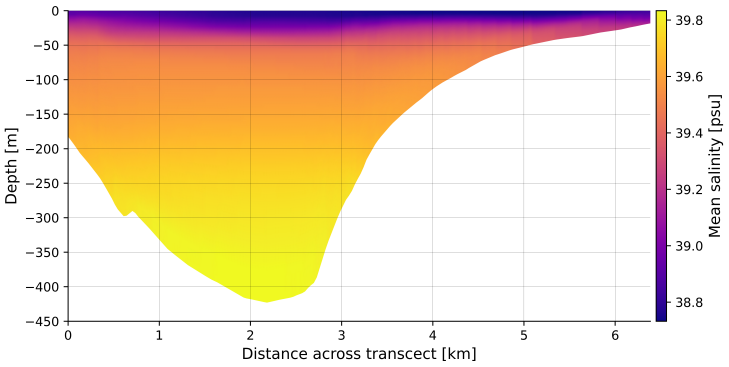

(b) Salinity

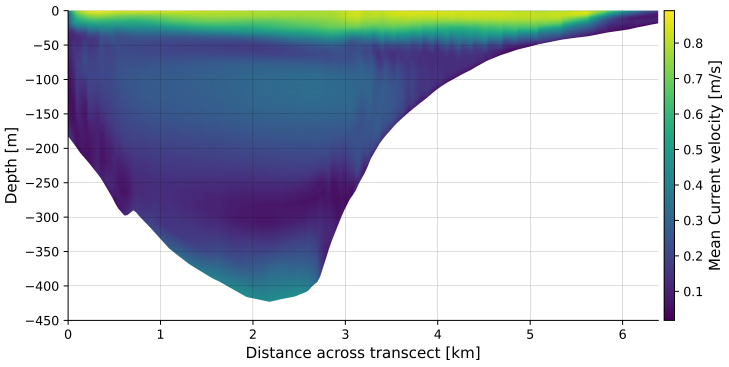

(c) Velocity norm

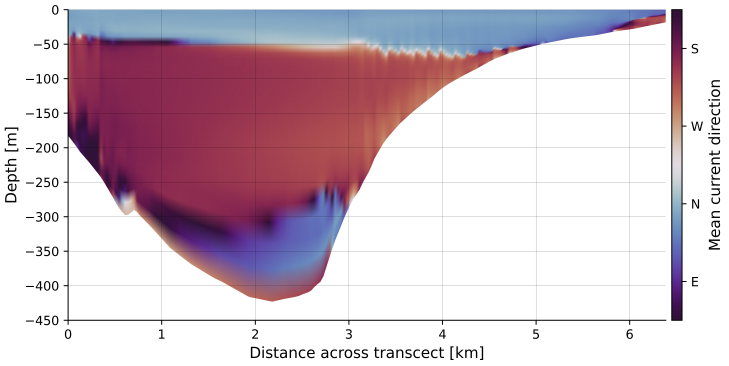

(d) Current direction

Figure 3.8: 34 days mean exchange flow proprieties in the Strait of Tiran. The two-layer exchange flow is composed of the warm and fresh inflowing NRS surface water and the cold and saline outflowing GoA intermediate water. The transect does not pass exactly over the strait sill.

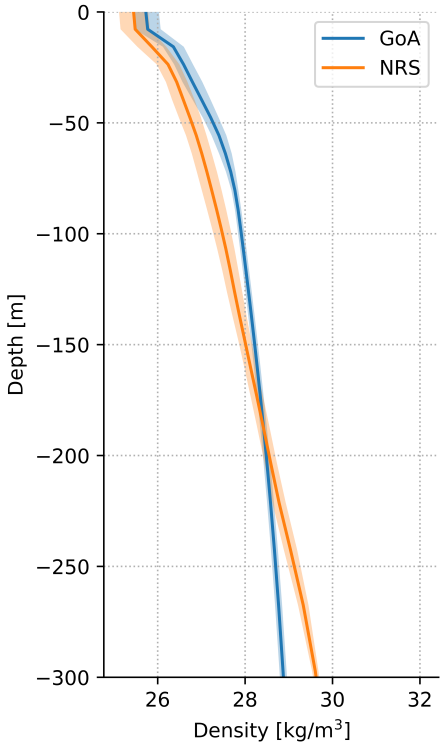

Figure 3.9: 34 days mean density profile of the water masses located approximately 3 km north and south of the Strait of Tiran sill. Shaded areas represent the standard deviation.

with the same density as the one of the first sediment class. Fine sediments can also travel into the NRS. In fact, the plume dispersal pattern for the two finest sediment classes are quite similar inside the NRS and cover almost the entirety of it. The main difference for these two sediment classes is the plume-free zone located next to Oxagon (Fig. 3.10B). The spatial extent of coarse sediments (>32 µm) is far more restricted than their fine counterparts. Coarse sediments can only travel a few kilometers from their release site. Most of their displacement happens during the first week and their rate of progression greatly reduces during the last three weeks.

The plume frequency shows the same pattern as the one identified with the sediment plumes: fine sediments have the potential to cover the whole domain while coarse sediments are extremely spatially restricted (Fig. 3.11). Besides, this metric shows the main dispersal patterns, which were impossible to discriminate using only the sediment footprints.

Fine sediments display the same dispersal patterns: particles released from Sindalah are either transported northward, where they enter the GoA by the western part of the Strait of Tiran, or are transported southward where they are predominantly captured by the anti-cyclonic NRS gyre (Fig. 3.11A-B). Particles released from Oxagon are transported northward and stay close to the coastline. A smaller, but non-negligible, fraction of particles are transported southward and away from the coast into the NRS. These main dispersal patterns have a high plume frequency of 85% and higher and reach values of 95% when close to either Sindalah or Oxagon. Conversely, some areas have relatively lowe plume frequency values. The eastern part of the Strait of Tiran seems to be less likely exposed to sediment plumes with maximum values of $\sim$ 60%. The Saudi coast of the northernmost part of the NRS has even lower frequency values of $\sim$ 50%. The lowest plume frequency values are found on the second northern half of the GoA, with values ranging from 30% to 40%.

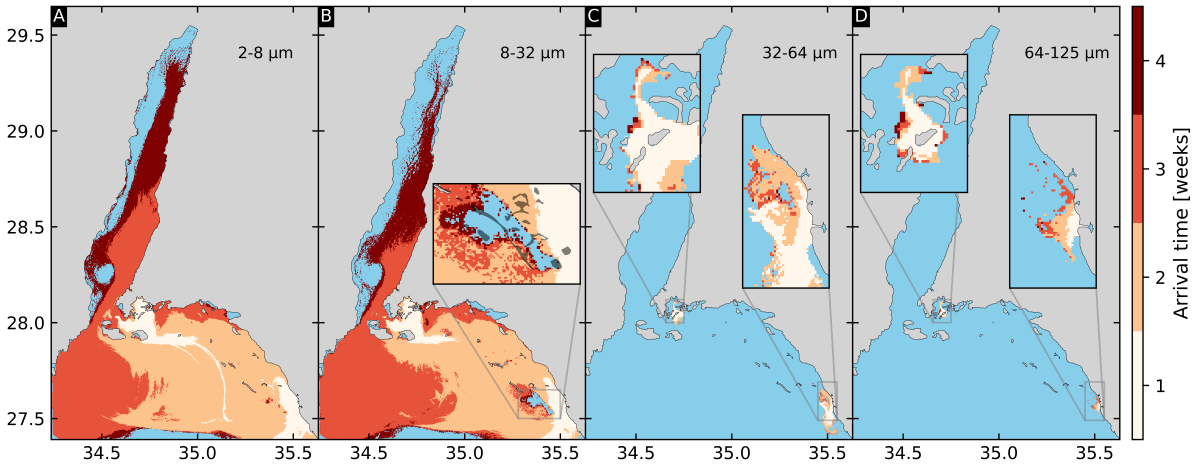

Figure 3.10: Footprints of sediment plumes dispersal for each sediment class expressed in the number of weeks elapsed since the start of the particles dispersal. For the two coarsest class of sediments, close-up views on Sindalah and Oxagon are added. Note the plume-free zone located next to Oxagon on panel B. In the close-up view on panel B, reefs are represented by the black shaded areas.

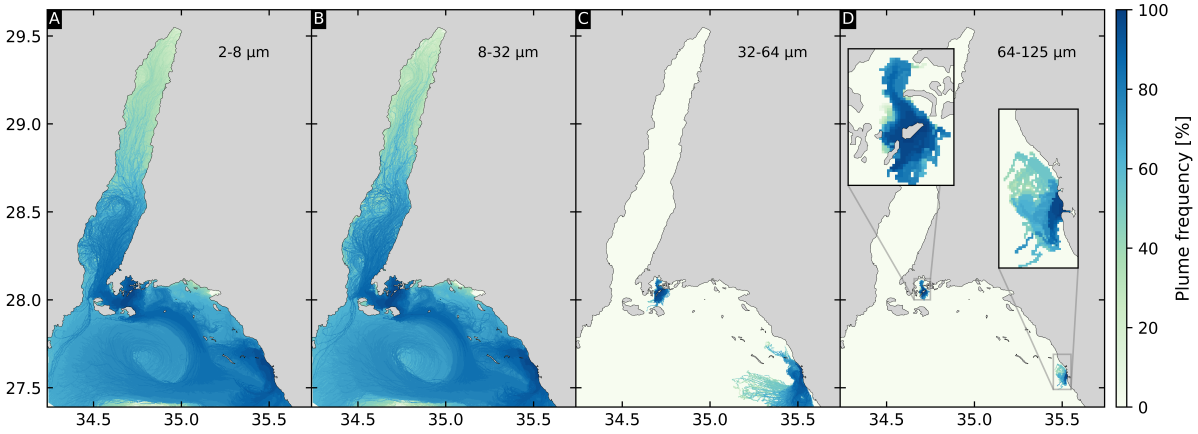

Figure 3.11: Plume frequency for each sediment class showcasing the main dispersal patterns. Close-up viewss of Sindalah and Oxagon are added for very fine sands

Coarse sediments display totally different dispersal patterns. Coarse silts released from Sindalah stay within a range of 10 km from their release site (Fig. 3.11C). As a consequence, the plume frequency mostly has very high values: 95% and higher. When released from Oxagon, coarse silts are mostly carried southward but the higher plume frequency is located along the coast to the north of the release site, over a distance of approximately 7 km. Very fine sands originating from Sindalah show the same dispersal pattern than coarse silts. When released from Oxagon, however, very fine sands, behave differently than coarse silts. The plume frequency is only higher next to Oxagon (<3 km) and does not show a preferential dispersal direction (Fig. 3.11D).

3.3 Environmental metrics and indicators

Larger particles are heavier and hence settle more quickly. The extent of the deposition zone increases as the particle sizes decrease (Fig. 3.12). The normalized cumulative deposition indicator shows that coarse sediments have higher deposition values but are restricted to an extent of approximately 10 km from their respective release site. Despite this spatial restriction, very fine sands showcase the highest deposition values across all the sediment classes (Fig. 3.12D). Fine sediments, on the other hand, settle all along the Saudi NRS and GoA coastline. The spatial deposition pattern on the NRS Saudi coast is the same for both the finest sediment classes, but fine and medium silts (Fig. 3.12B) display higher deposition values. On the contrary, coarse clays and very fine silts (Fig. 3.12A) have higher deposition values in the GoA as well as a higher deposition surface. Fine particles released from Sindalah have the potential to be carried up to the northernmost tip of the GoA, 190 km away from their release site.

The normalized cumulative turbidity indicator shows, once again, the same pattern highlighted by the sediment footprints and the plume frequency: fine sediments have the potential to cover the whole domain while coarse sediments are spatially restricted. Furthermore, the latter indicator shows that the surface area of high turbidity zones decreases as the particles size increases (Fig. 3.13). The two fine sediments classes have the same high turbidity zones pattern, with values slightly higher in the GoA and NRS for coarse clays and very fine silts (Fig.3.13A). Despite having a smaller spatial extent, coarse sediments display higher maximum turbidity values, which are located close to the release sites. When considering all of the sediment classes, we observe that most of the turbidity occurs north of Oxagon, along the coastline and all around Sindalah.

The total turbidity highlights the areas that are the most exposed to sediment plumes. Two areas stand out from the whole domain and are located next to Sindalah and Oxagon (Fig. 3.14A). The area surrounding Sindalah spans over 20 km from north to south with a width of 5 km. There are two smaller high exposure zones, located to the west and south-east of of the main high exposure zones. The main high-exposure area is located north of Oxagon, spanning over 35 km along the coastline. This area extends southward as well, but on a smaller distance of approximately 10 km. Others exposure zones with lower values can be observed as well, notably between the two main high-exposure ones. We can also observe that the track of the NRS gyre has higher exposure values. All the aforementioned exposure zones are located in the NRS. The only zone with slightly higher exposure values in the GoA is located on the Strait of Tiran and spans 20 km into the GoA, with values decreasing northward.

In a second step, we intersected the total turbidity exposure with the coral reefs. This yields exposure values exclusively over coral reefs (Fig. 3.14B) thus allowing to identify the reefs the most exposed to sediment plumes. We highlight two major zones: the first is located around Sindalah, while the second is situated north of Oxagon. Inside the first zone, we observe three reefs that have the highest possible exposure value loacted 9 km south, 2 km west and 8 km north of Sindalah (Fig. 3.14C). Within this first zone, most of the reefs have lower, but non-negligible, exposure values. On the contrary, a majority of reefs in the second zone have high exposure values. The most exposed reefs are located along the coastline, mainly north of Oxagon. We observe that this high-exposure zone is separated by a small area where reefs are less exposed, with values within the range of 0.3-0.5. The reefs located in the upper-left corner have a significantly lower exposure values. This contrasts with highly-exposed neighbouring reefs only 4 km away. The reefs located off-shore are relatively less exposed, with the exception

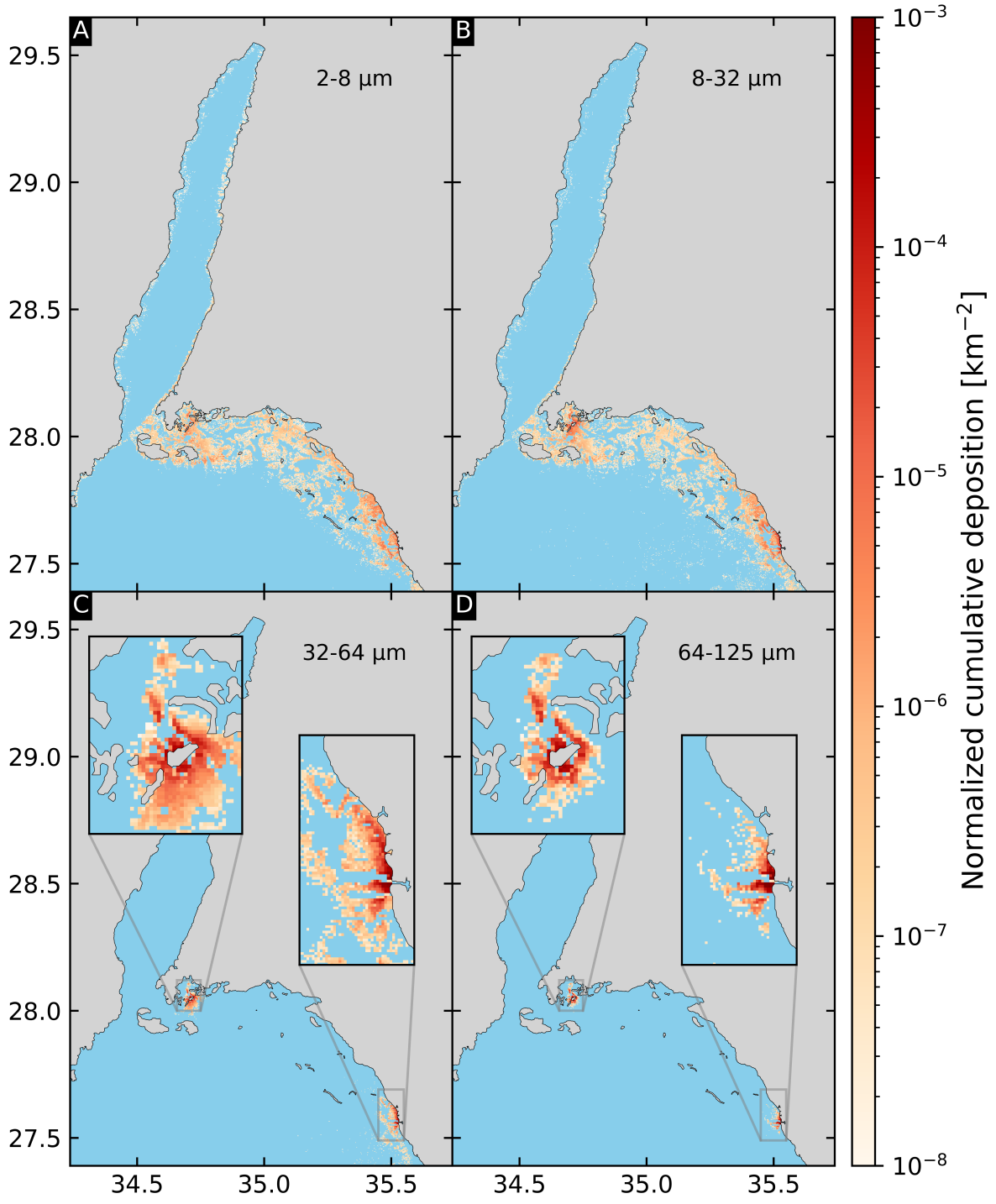

Figure 3.12: Average concentration of settled particles for all sediment classes. Deposition is higher for coarse sediments while fine sediments have the potential to settle almost 200 km away from their release site.

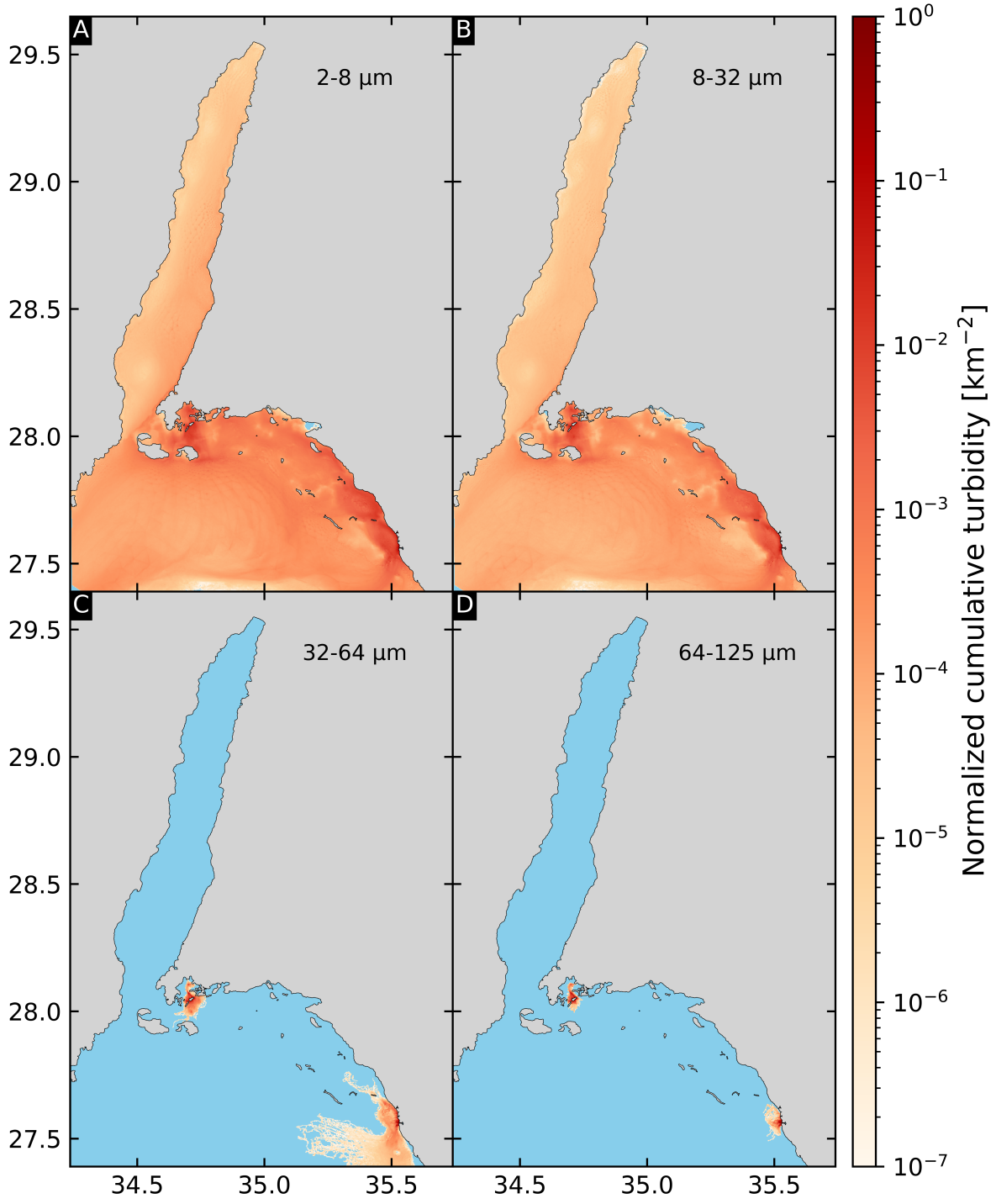

Figure 3.13: Average concentration of suspended particles for all sediment classes. High turbidity zones extent decrease as the particles size increases.

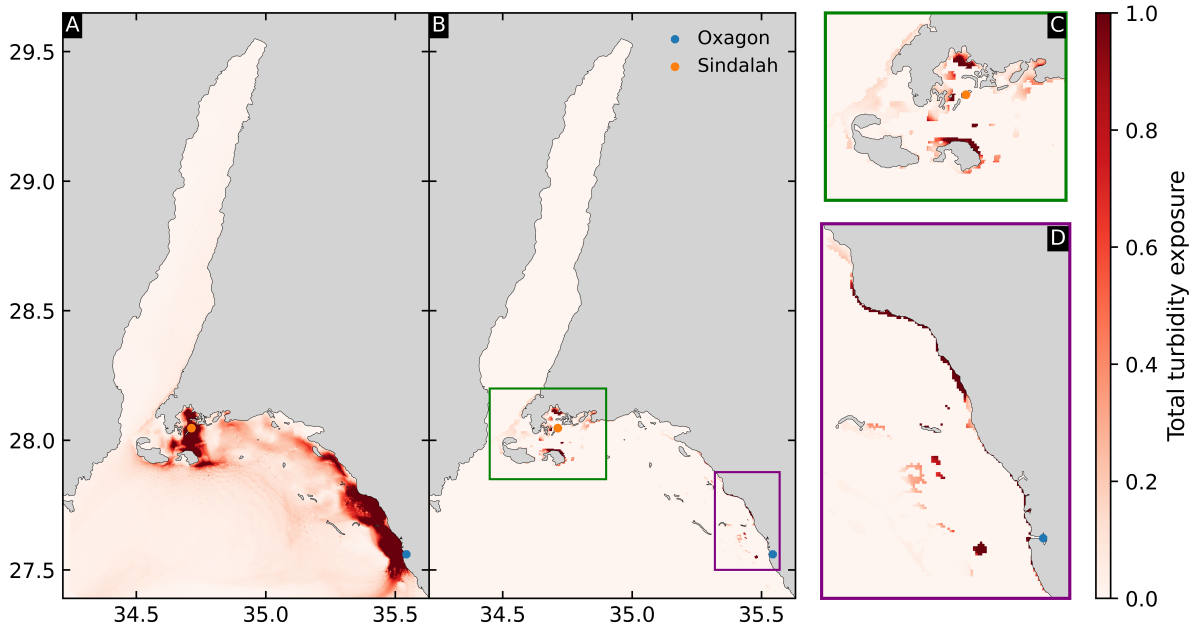

Figure 3.14: Total turbidity exposure (A) on the whole domain and (B) only on NRS and GoA coral reefs with a close-up view of (C) Sindalah and (D) Oxagon. The main high-exposure zone originates from Oxagon and spans over roughly 45 km.

of one reef located right next to Oxagon.

Chapter 4

Discussion

Despite the high error values on the current direction, our three-dimensional oceanic model still reproduces some important characteristics of the NRS and GoA physical oceanography. The seasonal conditions of the gulf are somewhat consistent with what can be found in the literature. During the months of October and November, the GoA is rather de-stratified as the inflowing NRS water mixes with the GoA intermediate layer. Our model also captures the complex surface flow composed of the NRS gyre and the chain of eddies along the GoA. We then used the simulated current to model the sediment dispersal from NEOM coastal development sites. Considering the error on the current direction, the dispersal results should therefore be interpreted with caution. With this consideration, our findings show that fine sediments (<32 µm) have a totally different dispersal pattern and footprint than coarse sediments (>32 µm). Larger, and hence heavier, sediments settled closer to the release sites with high deposition values. Fine sediments on the other hand have the potential to settle almost 200 km away from their release site, or to remain suspended in the water column and cover the whole domain. We then identified two main zones which are highly exposed to turbidity caused by sediment plumes, located along the coastline north of Oxagon and around Sindalah. Within these two zones, we highlighted the most exposed shallow coral reefs located less than 10 km from Sindalah and almost continuously along the coastline north of Oxagon.

4.1 Hydrodynamic model performance

The negative temperature gradient along the GoA is correctly captured which is in agreement with to previous modelling studies (Biton and Gildor, 2011a, 2016) as well as measurements (Paldor and Anati, 1979). It further matches the range of values given in Manasrah et al. (2019). Moreover, similarly to the aforementioned studies, the simulated negative thermal gradient is strong in the first northern half of the GoA and weaker afterwards. This thermal gradient is partially explained by the very high evaporation rates along the GoA. This results in a gradual increase in salinity toward the north (Manasrah et al., 2019), and is well captured by our model as well. Furthermore, the colder water temperatures along the eastern shore suggest that the model correctly represent upwelling resulting from the Ekman transort caused by wind, and corresponds to satellite imagery observations (Labiosa et al., 2003; Kaplan and Largier, 2006).

On a larger scale, our model reproduces the main characteristics of the NRS and GoA circulation. A relatively warm and fresh water enters the GoA in the south from the Strait of Tiran as a surface layer and flows northward, while cold and saline water exits the GoA as a bottom layer in the same strait. Biton and Gildor (2011a) showed that the GoA seasonality can be divided into

two periods. From April to September, during the restratification phase, the transport of NRS surface water into the GoA is at its maximum and the GoA surface layer is progressively rebuilt. As a consequence, the 21.9 °C isotherm is pushed down to ~ 200 m. From September onward, the mixing period starts. During this period the volume and temperature of the surface layer still increases but at a slower rate. At the beginning of October, according to Biton and Gildor (2011a), the 21.9 °C isotherm is at a depth of −175 m, while the output of our model shows that the same isotherm is located just above −200 m (Fig. 3.5). After the first week of November the isotherm depth increased of 50 m for our model and approximately 25 m for the model used for comparison, which is an acceptable range of values. For that period, both surface temperature fields are quite similar and have a value of ~ 26 °C. The GoA mixing condition described by Biton and Gildor (2011a) corresponds well to what can be observed by the temperature transects, which suggest that the model is able to reproduce the mixing dynamics taking place during that time of the year.

The Strait of Tiran connects the NRS to the GoA and the exchange flow over the strait is a key feature of the GoA. The exchange flow has been extensively studied over the years (Klinker et al., 1976; Murray et al., 1984; Manasrah et al., 2004; Ben-Sasson et al., 2009) but all the latter authors only considered a short period of time (typically 1 or 2 months). Biton and Gildor (2011a) were the first to study the complete seasonality of the exchange flow and showed that, during the majority of the year, it is constituted of a two-layer exchange flow that switches to a four-layer exchange flow from August to November. The authors defined the inflowing NRS surface water using net zero flux contour lines, which is located in the first 50 m of the water column. This layer has a temperature between 26 and 27 °C and a salinity of ~ 40.6 psu. The surface layer depth, determined using the current direction (Fig. 3.8d), as well as its temperature, are in agreement with our model. However, the simulated salinity values are about 1 psu saltier, with values of ~ 30.8 psu. Nonetheless, the range of salinity difference between the surface and −250 m are close, with a difference of ~ 0.3 psu between our model and the reference study, which again seems acceptable. The outflowing gulf intermediate water is delimited by the 21.9 °C isotherm and is located at a depth of −170 m according to Biton and Gildor (2011a). The average depth of the same isotherm over the whole simulated period is −160 m which is consistent with Biton et al.'s results (Fig. 3.4a). Nevertheless, we only observe a two-layer exchange flow instead of four. The exchange flow is driven by the density differences between the two water masses located on each side of the Strait of Tiran. Figure 3.9 shows that for any depth above −190 m, the GoA water is denser and hence flows below the NRS water. As a consequence no four-layer exchange flow is possible. Unlike other seasonal phenomena in the gulf, the four-layer pattern may not be a stable seasonal phenomenon characterizing the exchange flow seasonality through the Straits of Tiran and therefore may not occur on a yearly basis (Biton and Gildor, 2011b).

As mentioned previously, the surface current flows northward. The water mass properties in the northernmost part of the gulf reflect all the cumulative forcings applied to a parcel of water moving along the gulf. Hence, the tip of the GoA is the ideal location to assess the performance of the model. We compare the temperature and salinity profiles (Fig. 3.3) to monthly mean measurements for the 2003-2009 period presented in Biton and Gildor (2011a, 2016), at approximately 10 km of the tip of the gulf, where the measurement station is located. As explained previously, the SST is close to the observations. However, this relatively warm water layer exist until ~ 80 m according to the observations, while in our model this layer is extremely thin (less than 10 m). From the observations, the deep layer starts at −200 m while our results show that

it starts 200 m deeper, roughly at −400 m. Both intermediate layers have a similar width of ∼ 150 m but are at different depths. The salinity minimum is located at the surface whereas it should be located at a depth of −100 m. The observed salinity is mostly close to 40.7 psu with a minimum value of 40.55 psu, but our model displays values roughly 1 psu above the observations.

An important seasonal characteristic is the evolution of the salinity minimum that appears during the summer month and disappears after. Although the model doesn't capture the salinity minimum, the important salinity variations in the upper 150 m could be explained by the fact that the model still captures the variations that ultimately lead to the minimum, but not the minimum itself. The model temperature profile is quite similar to the ones observed during August and September. This would lead to believe that, in the northernmost part of the GoA, the model doesn't accurately represents the mixing conditions. This would also explained why the salinity minimum is located at the surface instead of deeper into the water column. This lack of mixing could be due to the coarse resolution of the NEMO model outputs used for the initial condition. Because of that resolution, there is no available data for the uppermost 10 km of the GoA. The last available values are thus extrapolated over this area, which do not accurately represent the northernmost mixing condition. This can be observed on the vertical transects (Fig. 3.4a and the corresponding animations). As shown by Biton and Gildor (2011a), the isotherms deepen from south to north. However, for the very last part of the GoA, the modeled isotherms rise. Thus it is likely the model needs more time before representing realistic conditions in that particular area, as it may not yet have converged to a dynamically stable equilibrium, and therefore partially explaining why the modeled temperature and salinity profiles correspond to stratified conditions.

The modeled surface current dynamics are complex and composed of various eddies along the GoA main axis, as reported in various studies (Berman et al., 2000; Gildor et al., 2010; Afargan and Gildor, 2015). Gildor et al. (2010) neglected the effects of winds, tides and irregularities in the coastline and bathymetry characteristic of the gulf but Afargan and Gildor (2015) took all these parameters into account and used high temporal and spatial resolution winds patterns. Their findings show that, in November, the surface current structure in the northern gulf consists of four eddies. Here, we only observe three, the fourth one, located at the tip of the GoA, was not observed. The latter gyre appears on rare occasions (Afargan and Gildor, 2015), therefore the model performance is satisfactory. Furthermore, the anti-cyclonic NRS gyre centered at ∼ 27.5 °N is consistent with simulated currents derived from satellite imagery (Taqi et al., 2019).

4.2 Assessment of the environmental impact

Few similar studies have been conducted in the NRS and GoA. It is therefore hard to compare our results with others. Nevertheless, Raitsos et al. (2017) used an LPT model forced by satellite-derived geostrophic velocities. They released coral larvae, which can be approximated by fine particles, from various location, including Duba which is located few kilometers south of Oxagon. Their dispersal patterns are similar to ours thus supporting our results.

The sediment footprints and plume frequencies of fine particles shows that the particles entering the GoA stay on the eastern shore as they are transported by the inflowing NRS surface water. Only the finest particles are observed on the western shore, which is know to experience important downwelling (Labiosa et al., 2003; Manasrah et al., 2006). Figures 3.10A and 3.10B both have plume-free zones. In the GoA, the plume free-zone corresponds to the gyre observed

on Fig. 3.6, while on the NRS it corresponds to a shallow area with an important number of reefs (Fig. 1.4) and a quite weak (~ 0.1 m/s) and turbulent flow (Fig. 3.7b). However the respective plume frequency of these plume-free zones are relatively high (> 60%). Thus these plume-free zones seem unrealistic as there are no reasons for such observations and are therefore visual artefacts which result from the arbitrary threshold value used in the methodology of the footprint computation. Nonetheless, the complex currents in these areas still transport fewer particles over these zones, as shown by the respective lower turbidity values (Fig. 3.13). Next to Oxagon, the currents seem too weak to transport particles larger than 8 µm since there is no plume-free zones for coarse clays and very fine silts (2-8 µm; Fig. 3.10A). Regarding the southernmost gyre located in the GoA, lower turbidity values could be explained by the upwelling inside the cyclonic eddy (Falkowski et al., 1991), keeping the particles suspended in the upper part of the water column and steering them away.

Our findings, while being highly uncertain due to the important error on the current directions, show that sediment plumes originating from NEOM coastal development sites have a high potential to impact the whole GoA and the area of the NRS considered in this work. On one hand, coarse sediments have the highest impact with regards to sediment deposition, but are spatially restricted thus reducing the total impacted area. Conversely, fine sediments have a large impact area but with less intensity. On the other hand, fine sediments can settle up to 200 km away from their release site, creating plumes that persist for an entire month. Therefore, to mitigate the environmental impact of sediment plumes, special attention should be given to fine particles.

4.3 Limitations and perspectives

We established a proof of concept of a 3D mutli-scale hydrodynamic model for the NRS and GoA region, despite the challenging features such as the significant bathymetry variations. This preliminary model still needs to be further improved, notably for the initial condition or for the wind forcings, for instance. Regardless how the hydrodynamic model performed, we paved the way to assess the environmental impact of the NEOM project on NRS and GoA marine ecosystems.

In a general way, our model correctly represents the main features of the NRS and GoA circulation and hydrodynamics rather well. Despite being qualitatively correct, our model performs poorly against *in-situ* current direction observations, but the results with regard to the velocity norm is satisfactory. This error could be the result of various factor. Firstly, we used σ-layers which are not designed to be used with domains featuring strong bathymetry gradients, such as this one. A more appropriate type of vertical layers would be σ-z layers. However, such vertical layers are not yet implemented in SLIM3D. Secondly, the resolution of the OGCM used to initialize our model, in this case; NEMO, is not high enough to correctly represent all the processes taking place in the GoA during the period of time considered here. As a consequence, extrapolation is used to tackle this issue, which yields erroneous initial conditions. However, this last issue could be resolved by considering a longer spin-up duration. Here, we only used a 38 days spin-up due to lack of time. Using a longer spin-up, such as one year, could help to mitigate the errors resulting from the initial conditions by ensuring that we simulated one full seasonal cycle before the period of interest. Such a long spin-up period will only be possible if the necessary computation resources are available. Moreover, we only considered a period of one month. This duration is not enough to correctly assess the ability of our model to represent

the complete seasonal variability. Nonetheless, based on the results for the month of October, the results are encouraging.

Most of the studies on the exchange flow across the Strait of Tiran either computed or measured the transport, which we did not do. Further work could implement such computations which will allow us the compare our model to the majority of these studies. As explained previously, during the mixing period, the GoA circulation is driven by density differences that partially result from important evaporation caused by the dry air blowing over the GoA. Hence, forcing our model with high-resolution wind data would greatly improve the results. Here we used the ERA5 dataset, but the Copernicus regional reanalysis for Europe (CERRA) dataset has recently been made available by ECMWF. The CERRA dataset covers the northern part of the Red Sea and the GoA with a spatial resolution of 5.5 km, against 31 km for ERA5 (Fig. E.1), but is currently only available until 2021.

Based on the RMSE values for the current direction, there seems to be a spatial dependency. For the first validation period, the ship was stationary during a non-negligible period of time. As explained in section 2.4.5, slow velocities improve the quality of the ADCP measurements. To ensure an optimal quality of the validation dataset, and therefore the quality of the validation, the ADCP data could be further investigated. The pre- and post-processing were conducted to the best of our capacity and by following the step-by-step instructions provided on the UH Currents Group website. Still, there remains uncertainty concerning the correctness of the resulting data. Furthermore, as the vertical resolution is increased closer to the surface, there could be a relation between the depth and the current direction error. This possibility was not further investigated due to lack of time.

We simulated sediment dispersal over one month. Given the important seasonality of the GoA, this is not sufficient to fully describe the particle dispersal. To have a representative view of the complete dispersal patterns, the LPT should be run over at least a year. This would allow us to take into account the seasonality of the GoA dynamics. This of course implies that the necessary hydrodynamics have been correctly modeled beforehand. Moreover, the rate of particle release was defined so that the total number of released particles would be high enough to ensure representative results. We did not take into account other dynamics which arise from complex dredging projects. Additionally, no resuspension was considered which is non-negligible, especially for mid-sized particles (Saint-Amand et al., 2022). Lastly, the short duration of the dispersal simulation implies that the finest sediment can only settle on the shallow parts of the domain. Indeed, assuming only a settling velocity of $w_s = 2 \times 10^{-5}$ m/s, which is representative for coarse clays and very fine silts, it would take approximately 2 months for a particle to reach a depth of -100 m, which is a depth at which mesophotic reefs can be found. Hence if we wish to include mesophotic reefs, the simulation duration must be increased.

Various approximations were made in the implementation of the LPT. First, the stochastic part of the displacement (i.e., the diffusion part) is solved using a simple forward Euler scheme, which is not the most accurate. A more precise alternative is the Milstein scheme (Gräwe and Wolff, 2010), which is already implemented in SLIM3D. However, the Milstein scheme is much more computationally expensive ($\sim$ 700 s/iter vs. $\sim$ 1 s/iter for the forward Euler method). Therefore, it is currently unrealistic to use the Milstein scheme. To make its use feasible, the computational cost must first be reduced. Secondly, the computation of the settling velocity relies on the kinematic viscosity which was set to a constant value of 10^{-6} m^2/s. To improve the

realism of the model, we could use an empirical formula based on the temperature and salinity to compute a more representative viscosity value. There is a clear footprint and sediment plumes pattern difference between fine and coarse particles. However, since we used relatively large sediment classes it is impossible to precisely identify the threshold at which these patterns begin to show significant differences. Further works should consider various sediment classes between 32 and 64 µm to identify this threshold. Identifying this threshold is crucial to implement effective measures to ensure sustainable coastal development.

We used the UNEP-WCMC data to assess the impacts on coral reefs. However this dataset is limited to shallow corals and does not consider the mesophotic reefs that exists in the GoA. Therefore the impacts that we reported are incomplete. Considering mesophotic reefs will allow us to have a more representative and realistic view of the environmental impacts on reefs. Moreover, some reefs that are clearly visible from satellite images are not present in the UNEP-WCMC data, but are reported in the Allen Coral Atlas dataset[1]. Combining both datasets could further improve the impact assessment. The total turbidity indicator allowed us to identify the most exposed reefs to turbidity caused by sediment plumes, but we did not assess the individual contribution of each sediment class to the total turbidity. This additional step would allow us to highlight which sediment class should be of particular concern on coastal development sites. Moreover, a supplementary step would be to compute risk maps. It is possible to derive the probability from the particle track, indicating the likelihood of a grid cell to contain a suspended particle. The risk is defined as the product between the exposition, in this case the total turbidity, and the probability of particle presence. To conduct this supplementary step, the only supplementary implementation is to assign an id to each particle to be able to reconstruct each particle track during post-processing.

Finally, only two release sites corresponding to two NEOM projects were considered. The most imposing one, The Line, was not considered as most of it is located away from the coastline. NEOM recently announced 12 new projects that will be located along 120 km of the Saudi GoA coastline (NEOM, 2024b). As such, future works will have to consider these new projects.

In a broader way, our model could provide further insights into marine pollution (e.g. desalination plants brines, heavy metals) and mesophotic-shallow reef interaction. Since they all are passive particles, they all can be tracked using the same LPT model. As discussed, shallow 'super-corals' are highly exposed and mesophotic reefs could provide resilience to these surface reefs. However, it is still unknown if such interactions are possible in the NRS and GoA. A first step towards a answer to this question would to test this hypothesis using our model.

[1] https://allencoralatlas.org

Chapter 5

Conclusion

In the context of a warming world, annual bleaching events are becoming more likely and threaten coral reefs on a global scale. However, the so-called 'super-corals' located in the NRS and GoA could act as a climate refuge until the end of the century. While being virtually immune to climate change, they are not immune to anthropogenic stressors such as the NEOM mega-project. The aim of this work was to assess the environmental impact of the NEOM project on coastal ecosystem by the means of an ocean model combined with a sediment dispersal modelling approach.

The first step consisted of modelling the 3D hydrodynamics in the NRS and GoA using the 3D version of the multi-scale ocean model SLIM. We were able to establish a proof of concept of a 3D hydrodynamic model, despite the challenging features of the GoA and NRS. We then used the modeled currents with a LPT model to simulate the sediment dispersal of various sediment types, ranging from 2 µm to 125 µm. From all the particle tracks, we derived sediment footprints and plume frequencies maps which allowed us to study the spatio-temporal patterns of the sediment plumes. Subsequently, we computed various environmental indicators that we intersected with coral reefs in order to highlight the most exposed ones.

In spite of our model being only partially quantitatively validated, it still correctly represents most of the physical oceanography features of the GoA and NRS. With this consideration, our results must be carefully interpreted. The spatio-temporal pattern analysis showed that, within 4 weeks after the release, fine particles have the potential to cover the almost entirety of the GoA and the considered area of the NRS. Conversely, coarse sediment have smaller spatial extent and most of their displacement takes place during the first week. As a consequence, coarse sediment plume frequency are the highest and the more denser, with maximum values of 95% and more. NRS and GoA coral reefs are mostly impacted by turbidity. Deposition for coarse sediments is high but extremely spatially restricted, while it is the opposite for fine sediments, which have the potential to settle up to 200 km away from their release site. We identified two high-exposure zones using the total turbidity indicator, which we then intersected with coral reefs. All the most exposed reefs are located in the NRS. Around Sindalah, three reefs are highly exposed, but the majority have relatively low values. Most of the reefs affected by Oxagon are situated to its north, extending along the coastline over an almost continuous zone of 45 km.

In a broader way, our model could provide further insights into marine pollution (e.g. desalination plants brines, heavy metals) and mesophotic-shallow reef interaction to effectively support sustainable coastal development.

Bibliography

Afargan, H. and Gildor, H. (2015). The role of the wind in the formation of coherent eddies in the gulf of eilat/aqaba. *Journal of Marine Systems*, 142:75–95.

Ahmed, A., Ahmed, M., Abou-Elhaggag, M., and El-Badry, H. (2012). Hydrodynamic modeling of the gulf of aqaba. *Journal of Environmental Protection*, 03.

Bak, R. P. M., Nieuwland, G., and Meesters, E. H. (2005). Coral reef crisis in deep and shallow reefs: 30 years of constancy and change in reefs of curacao and bonaire. *Coral Reefs*, 24(3):475–479.

Barale, V. et al. (2007). Marine and coastal features of the red sea. *European Commission, EUR*, 23091:56.

Beckmann, A. and Haidvogel, D. B. (1993). Numerical simulation of flow around a tall isolated seamount. part i: Problem formulation and model accuracy. *Journal of Physical Oceanography*, 23(8):1736–1753.

Bellworthy, J. and Fine, M. (2017). Beyond peak summer temperatures, branching corals in the gulf of aqaba are resilient to thermal stress but sensitive to high light. *Coral Reefs*, 36(4):1071–1082.

Ben-Sasson, M., Brenner, S., and Paldor, N. (2009). Estimating air–sea heat fluxes in semien-closed basins: The case of the gulf of elat (aqaba). *Journal of physical oceanography*, 39(1):185–202.

Berman, T., Paldor, N., and Brenner, S. (2000). Simulation of wind-driven circulation in the gulf of elat (aqaba). *Journal of Marine Systems*, 26(3-4):349–365.

Biton, E. and Gildor, H. (2011a). The general circulation of the gulf of aqaba (gulf of eilat) revisited: The interplay between the exchange flow through the straits of tiran and surface fluxes. *Journal of Geophysical Research: Oceans*, 116(C8).

Biton, E. and Gildor, H. (2011b). Stepwise seasonal restratification and the evolution of salinity minimum in the gulf of aqaba (gulf of eilat). *Journal of Geophysical Research: Oceans*, 116(C8).

Biton, E. and Gildor, H. (2016). On the origin of a chain of eddies in the gulf of eilat/aqaba. *Journal of Physical Oceanography*, 46(8):2269–2284.

Bongaerts, P., Ridgway, T., Sampayo, E. M., and Hoegh-Guldberg, O. (2010). Assessing the 'deep reef refugia'hypothesis: focus on caribbean reefs. *Coral Reefs*, 29(2):309–327.

Bongaerts, P., Riginos, C., Brunner, R., Englebert, N., Smith, S. R., and Hoegh-Guldberg, O. (2017). Deep reefs are not universal refuges: reseeding potential varies among coral species. *Science Advances*, 3(2):e1602373.

Braithwaite, C. J. (1987). *Geology and palaeogeography of the Red Sea region*. Pergamon Press Oxford.

Burchard, H., Bolding, K., and Villarreal, M. R. (1999). *GOTM, a general ocean turbulence model: theory, implementation and test cases*. Space Applications Institute.

Canuto, V. M., Howard, A., Cheng, Y., and Dubovikov, M. (2001). Ocean turbulence. part i: One-point closure model—momentum and heat vertical diffusivities. *Journal of Physical Oceanography*, 31(6):1413–1426.

Cetina-Heredia, P. and Connolly, S. R. (2011). A simple approximation for larval retention around reefs. *Coral Reefs*, 30:593–605.

Dalton, S. J. and Carroll, A. G. (2011). Monitoring coral health to determine coral bleaching response at high latitude eastern australian reefs: An applied model for a changing climate. *Diversity*, 3(4):592–610.

de Oliveira Soares, M., de Araújo, J. T., Ferreira, S. M. C., Santos, B. A., Boavida, J. R. H., Costantini, F., and Rossi, S. (2020). Why do mesophotic coral ecosystems have to be protected? *Science of The Total Environment*, 726:138456.

Delandmeter, P. (2017). *Discontinuous Galerkin finite element modelling of geophysical and environmental flows*. PhD thesis, UCLouvain.

De'Ath, G., Fabricius, K. E., Sweatman, H., and Puotinen, M. (2012). The 27–year decline of coral cover on the great barrier reef and its causes. *Proceedings of the National Academy of Sciences*, 109(44):17995–17999.

Diaz, C., Foster, N. L., Attrill, M. J., Bolton, A., Ganderton, P., Howell, K. L., Robinson, E., and Hosegood, P. (2023). Mesophotic coral bleaching associated with changes in thermocline depth. *Nature Communications*, 14(1):6528.

DiBattista, J. D., Howard Choat, J., Gaither, M. R., Hobbs, J.-P. A., Lozano-Cortés, D. F., Myers, R. F., Paulay, G., Rocha, L. A., Toonen, R. J., Westneat, M. W., et al. (2016). On the origin of endemic species in the red sea. *Journal of Biogeography*, 43(1):13–30.

Dixon, A. M., Forster, P. M., Heron, S. F., Stoner, A. M., and Beger, M. (2022). Future loss of local-scale thermal refugia in coral reef ecosystems. *PLoS Climate*, 1(2):e0000004.

Dobbelaere, T., Holstein, D. M., Gramer, L. J., McEachron, L., and Hanert, E. (2024). Investigating the link between the port of miami dredging and the onset of the stony coral tissue loss disease epidemics [submitted for publication]. *Marine Pollution Bulletin*.

Done, T. (2011). *Coral Reef, Definition*, pages 261–267. Springer Netherlands, Dordrecht.

Eakin, C. M., Morgan, J. A., Heron, S. F., Smith, T. B., Liu, G., Alvarez-Filip, L., Baca, B., Bartels, E., Bastidas, C., Bouchon, C., et al. (2010). Caribbean corals in crisis: record thermal stress, bleaching, and mortality in 2005. *PloS one*, 5(11):e13969.

Eakin, C. M., Sweatman, H. P. A., and Brainard, R. E. (2019). The 2014–2017 global-scale coral bleaching event: insights and impacts. *Coral Reefs*, 38(4):539–545.

Edwards, F. J. (1987). Chapter 3 - climate and oceanography. In EDWARDS, A. J. and HEAD, S. M., editors, *Red Sea*, Key Environment Series, pages 45–69. Pergamon, Amsterdam.

Egbert, G. D. and Erofeeva, S. Y. (2002). Efficient inverse modeling of barotropic ocean tides. *Journal of Atmospheric and Oceanic technology*, 19(2):183–204.

Erftemeijer, P. L., Riegl, B., Hoeksema, B. W., and Todd, P. A. (2012). Environmental impacts of dredging and other sediment disturbances on corals: a review. *Marine pollution bulletin*, 64(9):1737–1765.

Evensen, N. R., Fine, M., Perna, G., Voolstra, C. R., and Barshis, D. J. (2021). Remarkably high and consistent tolerance of a red sea coral to acute and chronic thermal stress exposures. *Limnology and Oceanography*, 66(5):1718–1729.

Eyal, G., Tamir, R., Kramer, N., Eyal-Shaham, L., and Loya, Y. (2019). The red sea: Israel. *Mesophotic coral ecosystems*, pages 199–214.

Falkowski, P. G., Ziemann, D., Kolber, Z., and Bienfang, P. K. (1991). Role of eddy pumping in enhancing primary production in the ocean. *Nature*, 352(6330):55–58.

Fattouh, B. and Sen, A. (2016). Saudi arabia's vision 2030, oil policy and the evolution of the energy sector. *Oxford Institute for Energy Studies, Oxford Energy Comment, July https://www. oxfordenergyorg/wpcms/wpcontent/uploads/2016/07/Saudi-Arabias-Vision-2030-Oil-Policy-and-the-Evolutionof-the-Energy-Sectorpdf*.

Fine, M., Cinar, M., Voolstra, C. R., Safa, A., Rinkevich, B., Laffoley, D., Hilmi, N., and Allemand, D. (2019). Coral reefs of the red sea—challenges and potential solutions. *Regional Studies in Marine Science*, 25:100498.

Fine, M., Gildor, H., and Genin, A. (2013). A coral reef refuge in the red sea. *Global change biology*, 19(12):3640–3647.

Fisher, R., O'Leary, R. A., Low-Choy, S., Mengersen, K., Knowlton, N., Brainard, R. E., and Caley, M. J. (2015). Species richness on coral reefs and the pursuit of convergent global estimates. *Current Biology*, 25(4):500–505.

Geuzaine, C. and Remacle, J.-F. (2009). Gmsh: A 3-d finite element mesh generator with built-in pre-and post-processing facilities. *International journal for numerical methods in engineering*, 79(11):1309–1331.

Gildor, H., Fredj, E., and Kostinski, A. (2010). The gulf of eilat/aqaba: a natural driven cavity? *Geophysical & Astrophysical Fluid Dynamics*, 104(4):301–308.

Glynn, P. W. and D'Croz, L. (1990). Experimental evidence for high temperature stress as the cause of el niño-coincident coral mortality. *Coral Reefs*, 8(4):181–191.

Gräwe, U. and Wolff, J.-O. (2010). Suspended particulate matter dynamics in a particle framework. *Environmental fluid mechanics*, 10:21–39.

Hall, E. R., Muller, E. M., Goulet, T., Bellworthy, J., Ritchie, K. B., and Fine, M. (2018). Eutrophication may compromise the resilience of the red sea coral stylophora pistillata to global change. *Marine Pollution Bulletin*, 131:701–711.

Hamilton, E. L. and Bachman, R. T. (1982). Sound velocity and related properties of marine sediments. *The Journal of the Acoustical Society of America*, 72(6):1891–1904.

Haney, R. L. (1991). On the pressure gradient force over steep topography in sigma coordinate ocean models.

Hoegh-Guldberg, O. (1999). Climate change, coral bleaching and the future of the world's coral reefs. *Marine and Freshwater Research*, 50.

Hoegh-Guldberg, O. (2005). Low coral cover in a high-co2 world. *Journal of Geophysical Research: Oceans*, 110(C9).

Hoegh-Guldberg, O. (2011). Coral reef ecosystems and anthropogenic climate change. *Regional Environmental Change*, 11(1):215–227.

Hoegh-Guldberg, O., Fine, M., Sawalmih, A. A., Ferrier-Pagès, C., Meibom, A., Ormond, R., and Voolstra, C. R. (2022). The gulf of aqaba's reefs of hope : Assigning world heritage status to the coral reefs of the gulf of aqaba, northern red sea. online at https://policylabs.frontiersin.org/content/the-gulf-of-aqabas-reefs-of-hope-science-policy-paper.

Hoegh-Guldberg, O., Jacob, D., Bindi, M., Brown, S., Camilloni, I., Diedhiou, A., Djalante, R., Ebi, K., Engelbrecht, F., Guiot, J., et al. (2018). Impacts of 1.5 c global warming on natural and human systems. *Global warming of 1.5° C*.

Hoegh-Guldberg, O., Poloczanska, E. S., Skirving, W., and Dove, S. (2017). Coral reef ecosystems under climate change and ocean acidification. *Frontiers in Marine Science*, 4.

Holstein, D. M., Paris, C. B., Vaz, A. C., and Smith, T. B. (2016). Modeling vertical coral connectivity and mesophotic refugia. *Coral Reefs*, 35(1):23–37.

Hughes, T. P., Anderson, K. D., Connolly, S. R., Heron, S. F., Kerry, J. T., Lough, J. M., Baird, A. H., Baum, J. K., Berumen, M. L., Bridge, T. C., Claar, D. C., Eakin, C. M., Gilmour,

J. P., Graham, N. A. J., Harrison, H., Hobbs, J.-P. A., Hoey, A. S., Hoogenboom, M., Lowe, R. J., McCulloch, M. T., Pandolfi, J. M., Pratchett, M., Schoepf, V., Torda, G., and Wilson, S. K. (2018). Spatial and temporal patterns of mass bleaching of corals in the anthropocene. *Science*, 359(6371):80–83.

IPCC (2023). Synthesis report summary for policymakers. *Climate Change 2023: Synthesis Report. Contribution of Working Groups I, II and III to the Sixth Assessment Report of the Intergovernmental Panel on Climate Change*, pages 1–34.

Jackett, D. R., McDougall, T. J., Feistel, R., Wright, D. G., and Griffies, S. M. (2006). Algorithms for density, potential temperature, conservative temperature, and the freezing temperature of seawater. *Journal of Atmospheric and Oceanic Technology*, 23(12):1709–1728.

Jantara Junior, V. L., Ramirez, I. S., Garcia Marquez, F. P., and Papaelias, M. (2021). Numerical evaluation of type i pressure vessels for ultra-deep ocean trench exploration. *Results in Engineering*, 11:100267.

Jha, R. and Zi-rong, X. (2004). Biomedical compounds from marine organisms. *Marine Drugs*, 2:123 – 146.

Jones, R., Fisher, R., and Bessell-Browne, P. (2019). Sediment deposition and coral smothering. *PLoS One*, 14(6):e0216248.

Kantha, L. H. and Clayson, C. A. (2000). *Numerical models of oceans and oceanic processes*. Elsevier.

Kaplan, D. M. and Largier, J. (2006). Hf radar-derived origin and destination of surface waters off bodega bay, california. *Deep Sea Research Part II: Topical Studies in Oceanography*, 53(25):2906–2930. The Role of Wind-Driven Flow in Shelf Productivity.

Kärnä, T., Legat, V., Deleersnijder, E., and Burchard, H. (2012). Coupling of a discontinuous galerkin finite element marine model with a finite difference turbulence closure model. *Ocean Modelling*, 47:55–64.

Klinker, J., Reiss, Z., Kropach, C., Levanon, I., Harpaz, H., Halicz, E., and Assaf, G. (1976). Observations on circulation pattern in gulf of elat (aqaba), red-sea. *Israel Journal of Earth Sciences*, 25(4-Mar):85–103.

Knowlton, N. (2001). The future of coral reefs. *Proceedings of the National Academy of Sciences*, 98(10):5419–5425.

Knowlton, N. and Jackson, J. B. C. (2001). The ecology of coral reefs. In *Marine Community Ecology*, pages 395–422. Sinauer, Sunderland, MA.

Kramer, N., Eyal, G., Tamir, R., and Loya, Y. (2019). Upper mesophotic depths in the coral reefs of eilat, red sea, offer suitable refuge grounds for coral settlement. *Scientific Reports*, 9(1):2263.

Krueger, T., Horwitz, N., Bodin, J., Giovani, M.-E., Escrig, S., Meibom, A., and Fine, M. (2017). Common reef-building coral in the northern red sea resistant to elevated temperature and acidification. *Royal Society open science*, 4(5):170038.

Labiosa, R. G., Arrigo, K. R., Genin, A., Monismith, S. G., and van Dijken, G. (2003). The interplay between upwelling and deep convective mixing in determining the seasonal phytoplankton dynamics in the gulf of aqaba: Evidence from seawifs and modis. *Limnology and oceanography*, 48(6):2355–2368.

Lakhouit, A. (2019). Tourism impact on marine ecosystems in the north of red sea. *Journal of Sustainable Development*, 13(1):10–7.

Lesser, M. P., Slattery, M., and Leichter, J. J. (2009). Ecology of mesophotic coral reefs. *Journal of Experimental Marine Biology and Ecology*, 375(1):1–8.

Loya, Y. (1972). Community structure and species diversity of hermatypic corals at eilat, red sea. *Marine Biology*, 13:100–123.

MacDonald, N. J., Davies, M. H., Zundel, A. K., Howlett, J. D., Demirbilek, Z., Gailani, J. Z., Lackey, T. C., Smith, J., et al. (2006). Ptm: Particle tracking model report 1: Model theory, implementation, and example applications. *ERDC/CHL TR-06-20. Vicksburg, MS: US Army Engineer Research and Development Center. http://acwc. sdp. sirsi. net/client/search/asset/1000777*.

Madakam, S. and Bhawsar, P. (2020). Neom smart city: The city of future (the urban oasis in saudi desert). *Handbook of smart cities*, pages 1–23.

Madec, G., Bell, M., Blaker, A., Bricaud, C., Bruciaferri, D., Castrillo, M., Calvert, D., Chanut, J., Clementi, E., Coward, A., Epicoco, I., Éthé, C., Ganderton, J., Harle, J., Hutchinson, K., Iovino, D., Lea, D., Lovato, T., Martin, M., Martin, N., Mele, F., Martins, D., Masson, S., Mathiot, P., Mele, F., Mocavero, S., Müller, S., Nurser, A. G., Paronuzzi, S., Peltier, M., Person, R., Rousset, C., Rynders, S., Samson, G., Téchené, S., Vancoppenolle, M., and Wilson, C. (2023). Nemo ocean engine reference manual.

Manasrah, R., Abu-Hilal, A., and Rasheed, M. (2019). *Physical and Chemical Properties of Seawater in the Gulf of Aqaba and Red Sea*, pages 41–73. Springer International Publishing, Cham.

Manasrah, R., Badran, M., Lass, H. U., and Fennel, W. (2004). Circulation and winter deep-water formation in the northern red sea. *Oceanologia*, 46(1).

Manasrah, R. S., Al-Horani, F. A., Rasheed, M. Y., Al-Rousan, S. A., and Khalaf, M. A. (2006). Patterns of summer vertical and horizontal currents in coastal waters of the northern gulf of aqaba, red sea. *Estuarine, Coastal and Shelf Science*, 69(3-4):567–579.

Moberg, F. and Folke, C. (1999). Ecological goods and services of coral reef ecosystems. *Ecological Economics*, 29(2):215–233.

Murray, S. P., Hecht, A., and Babcock, A. (1984). On the mean flow in the tiran strait in winter. *Journal of marine research*, 42(2):265–287.

Muscatine, L. and Porter, J. W. (1977). Reef Corals: Mutualistic Symbioses Adapted to Nutrient-Poor Environments. *BioScience*, 27(7):454–460.

NEOM (2024a). NEOM and MDL Beast set to unveil a luxurious beach club experience on Sindalah Island. https://www.neom.com/en-us/newsroom/neom-mdlbeast-luxurious-beach-club.

NEOM (2024b). Neom reveals magna, its new coastal region. https://www.neom.com/en-us/newsroom/neom-reveals-magna.

Okubo, A. (1971). Oceanic diffusion diagrams. *Deep Sea Research and Oceanographic Abstracts*, 18(8):789–802.

Osman, E. O., Smith, D. J., Ziegler, M., Kürten, B., Conrad, C., El-Haddad, K. M., Voolstra, C. R., and Suggett, D. J. (2018). Thermal refugia against coral bleaching throughout the northern red sea. *Global change biology*, 24(2):e474–e484.

Paldor, N. and Anati, D. (1979). Seasonal variations of temperature and salinity in the gulf of elat (aqaba). 26:661–672.

Pandolfi, J. M., Bradbury, R. H., Sala, E., Hughes, T. P., Bjorndal, K. A., Cooke, R. G., McArdle, D., McClenachan, L., Newman, M. J. H., Paredes, G., Warner, R. R., and Jackson, J. B. C. (2003). Global trajectories of the long-term decline of coral reef ecosystems. *Science*, 301(5635):955–958.

Papadopoulos, V. P., Zhan, P., Sofianos, S. S., Raitsos, D. E., Qurban, M., Abualnaja, Y., Bower, A., Kontoyiannis, H., Pavlidou, A., Asharaf, T. M., et al. (2015). Factors governing the deep ventilation of the r ed s ea. *Journal of Geophysical Research: Oceans*, 120(11):7493–7505.

Raitsos, D. E., Brewin, R. J., Zhan, P., Dreano, D., Pradhan, Y., Nanninga, G. B., and Hoteit, I. (2017). Sensing coral reef connectivity pathways from space. *Scientific Reports*, 7(1):9338.

Ribot, M., Klinger, Y., Jónsson, S., Avsar, U., Pons-Branchu, E., Matrau, R., and Mallon, F. L. (2021). Active faults' geometry in the gulf of aqaba, southern dead sea fault, illuminated by multibeam bathymetric data. *Tectonics*, 40(4):e2020TC006443.

Rocha, L. A., Pinheiro, H. T., Shepherd, B., Papastamatiou, Y. P., Luiz, O. J., Pyle, R. L., and Bongaerts, P. (2018). Mesophotic coral ecosystems are threatened and ecologically distinct from shallow water reefs. *Science*, 361(6399):281–284.

Saint-Amand, A., Grech, A., Choukroun, S., and Hanert, E. (2022). Quantifying the environmental impact of a major coal mine project on the adjacent great barrier reef ecosystems. *Marine Pollution Bulletin*, 179:113656.

Skirving, W., Marsh, B., De La Cour, J., Liu, G., Harris, A., Maturi, E., Geiger, E., and Eakin, C. M. (2020). Coraltemp and the coral reef watch coral bleaching heat stress product suite version 3.1. *Remote Sensing*, 12(23).

Smagorinsky, J. (1963). General circulation experiments with the primitive equations: I. the basic experiment. *Monthly weather review*, 91(3):99–164.

Sofianos, S. S. and Johns, W. E. (2003). An oceanic general circulation model (ogcm) investigation of the red sea circulation: 2. three-dimensional circulation in the red sea. *Journal of Geophysical Research: Oceans*, 108(C3).

Song, Y. and Haidvogel, D. (1994). A semi-implicit ocean circulation model using a generalized topography-following coordinate system. *Journal of Computational Physics*, 115(1):228–244.

Soulsby, R. (1997). Dynamics of marine sands.

Spalding, M., Ravilious, C., and Green, E. P. (2001). *World atlas of coral reefs*. Univ of California Press.

Storlazzi, C. D., Norris, B. K., and Rosenberger, K. J. (2015). The influence of grain size, grain color, and suspended-sediment concentration on light attenuation: Why fine-grained terrestrial sediment is bad for coral reef ecosystems. *Coral Reefs*, 34(3):967–975.

Takeyasu, K., Uchiyama, Y., and Mitarai, S. (2023). Quantifying connectivity between mesophotic and shallow coral larvae in okinawa island, japan: a quadruple nested high-resolution modeling study. *Frontiers in Marine Science*, 10:1174940.

Taqi, A. M., Al-Subhi, A. M., Alsaafani, M. A., and Abdulla, C. P. (2019). Estimation of geostrophic current in the red sea based on sea level anomalies derived from extended satellite altimetry data. *Ocean Science*, 15(3):477–488.

Thomas, C. J., Bridge, T. C., Figueiredo, J., Deleersnijder, E., and Hanert, E. (2015). Connectivity between submerged and near-sea-surface coral reefs: can submerged reef populations act as refuges? *Diversity and Distributions*, 21(10):1254–1266.

Trommer, G., Siccha, M., Rohling, E. J., Grant, K., van der Meer, M. T., Schouten, S., Hemleben, C., and Kucera, M. (2010). Millennial-scale variability in red sea circulation in response to holocene insolation forcing. *Paleoceanography*, 25(3).

UNEP-WCMC, WorldFishCentre, WRI, and TNC (2021). Global distribution of coral reefs. Compiled from multiple sources including the Millennium Coral Reef Mapping Project. Version 4.1, updated by UNEP-WCMC. Includes contributions from IMaRS-USF and IRD (2005), IMaRS-USF (2005) and Spalding et al. (2001). Cambridge (UK): UN Environment Programme World Conservation Monitoring Centre. Data DOI : https://doi.org/10.34892/t2wk-5t34.

Vallaeys, V. (2018). *Discontinuous Galerkin finite element modelling of estuarine and plume dynamics*. PhD thesis, UCLouvain.

Wagner, D., Friedlander, A. M., Pyle, R. L., Brooks, C. M., Gjerde, K. M., and Wilhelm, T. (2020). Coral reefs of the high seas: hidden biodiversity hotspots in need of protection. *Frontiers in Marine Science*, page 776.

Wentworth, C. K. (1922). A scale of grade and class terms for clastic sediments. *The journal of geology*, 30(5):377–392.

Yao, F., Hoteit, I., Pratt, L. J., Bower, A. S., Köhl, A., Gopalakrishnan, G., and Rivas, D. (2014). Seasonal overturning circulation in the red sea: 2. winter circulation. *Journal of Geophysical Research: Oceans*, 119(4):2263–2289.

Appendix A

Mathematical descriptions of the stretching functions

In this work we used the stretching functions described by Song and Haidvogel (1994) which the user can control using three parameters :h_c, θ_s and θ_b. The stretching function equation read:

$$z_i|_{h_i<h_c} = \sigma(h_i + \eta_i) \tag{A.1}$$

$$z_i|_{h_i>=h_c} = \sigma.h_c + C(\sigma).(h_i + \eta_i - h_c) \tag{A.2}$$

where

$$\sigma = \frac{-k}{nz} \quad \text{with} \quad 0 \leq k \leq nz \tag{A.3}$$

$$C(\sigma) = (1-\theta_b)\frac{\sinh(\theta_s.\sigma)}{\sinh(\theta_s)} + \theta_b \frac{\tanh\left[\theta_s.\left(\sigma+\frac{1}{2}\right)\right] - \tanh\left(\frac{\theta_s}{2}\right)}{2\tanh\left(\frac{\theta_s}{2}\right)} \tag{A.4}$$

With z_i the vertical coordinates of the series of nodes under surface node i (negative downwards), h_c a positive critical depth, h_i the local bathymetry, η_i the local sea surface elevation, θ_b a bottom control parameter, θ_s a surface control parameter, and sinh and tanh the hyperbolic sinus and tangent.

The SH function divides the domain into two part and uses a different stretching in each. For $h_i < h_c$ pure σ-layers are applied (i.e. there is no stretching). In other areas the SH stretching function is applied with the parameters specified by the user. $\theta_s \in]0;20]$ is such that the larger its value, the more compressed the layers are above h_c. $\theta_b \in [0;1[$ controls the dispatch of the stretching between the surface and the bottom. The lower its value, the more the resolution goes only to the surface (above the critical depth). On the contrary, the higher its value, the more the resolution is shared between the surface and the bottom. This last feature is pretty useful to create a second focal depth in the water column, near the bottom for instance. The parameters used where :

$$h_c = 250\,\text{m} \qquad \theta_s = 8 \qquad \theta_b = 0.005$$

Appendix B

Smoothing effect on the bathymetry

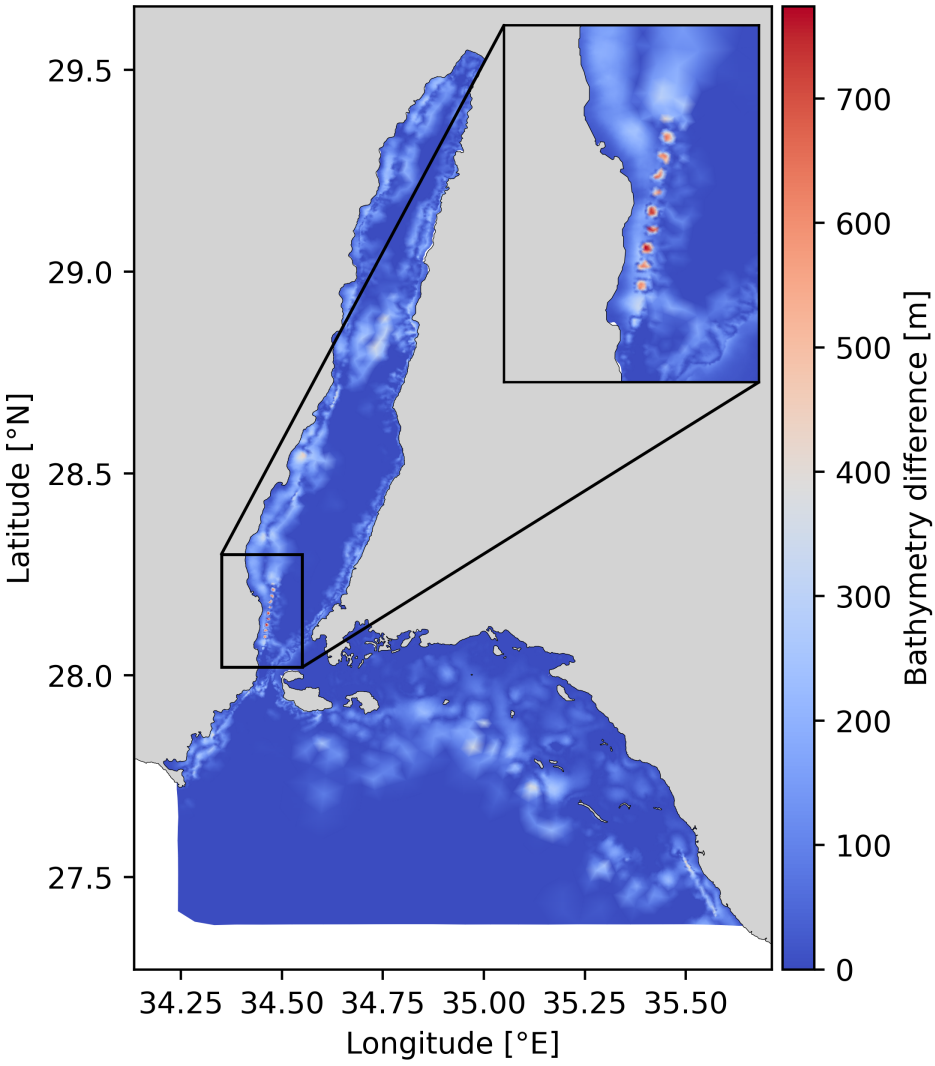

Figure B.1: Smoothing effect from the prepossessing step measured as the difference from the merged GEBCO-Ribot bathymetry and the smoothed and merged GEBCO-Ribot bathymetry. Mean difference is 38 m while the median is 13 m.

Appendix C

Validation

C.1 Validation cruise tracks

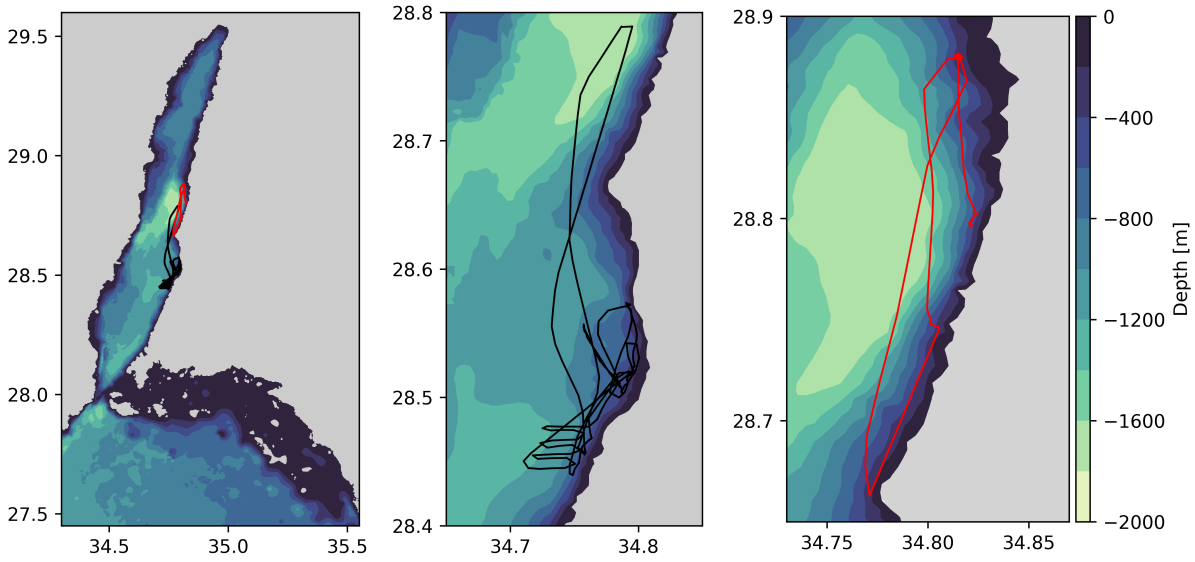

Figure C.1: Cruise tracks for the first validation period (black) and the second (red)

C.2 Validation period 1

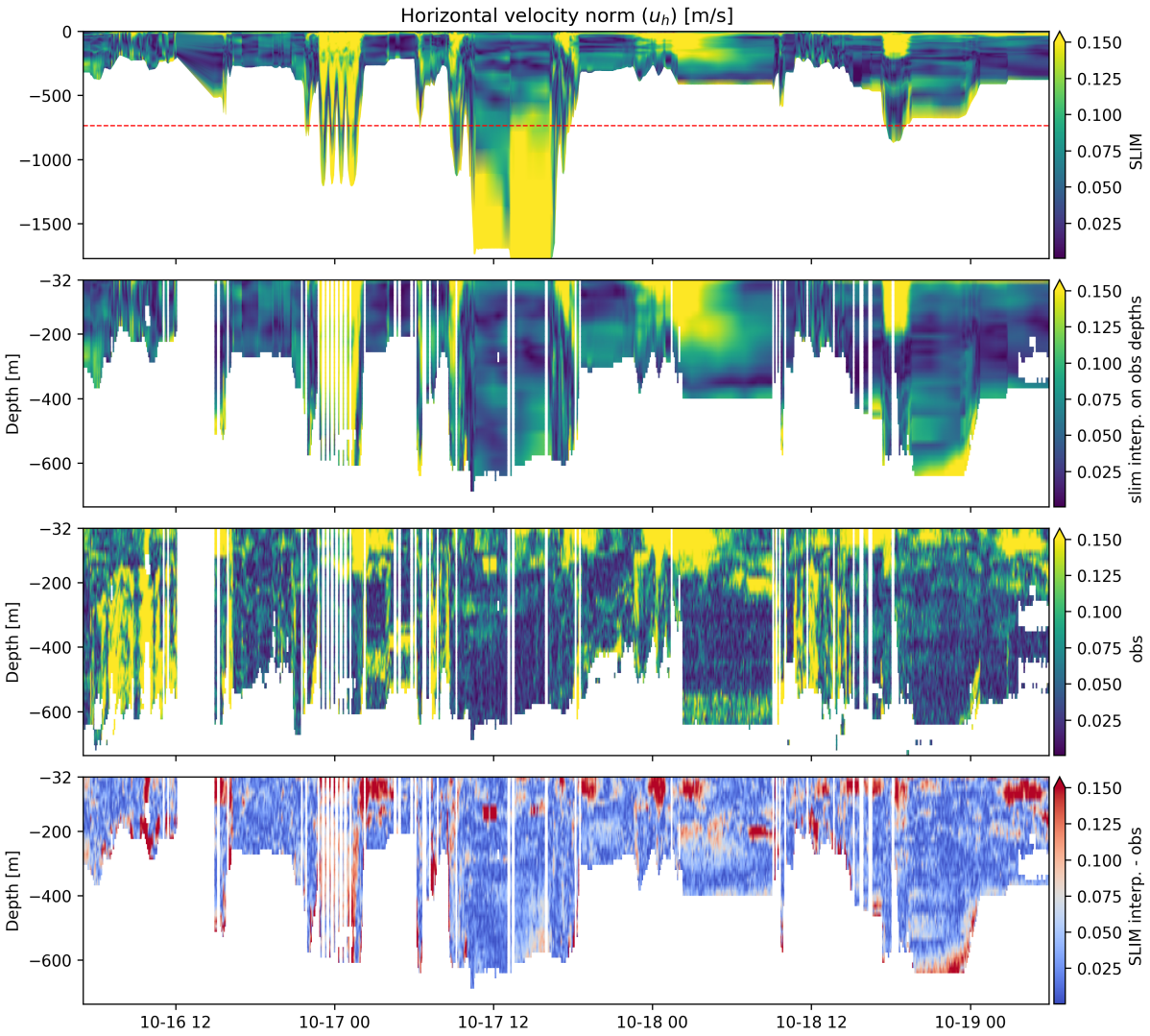

Figure C.2: current norm from wh300

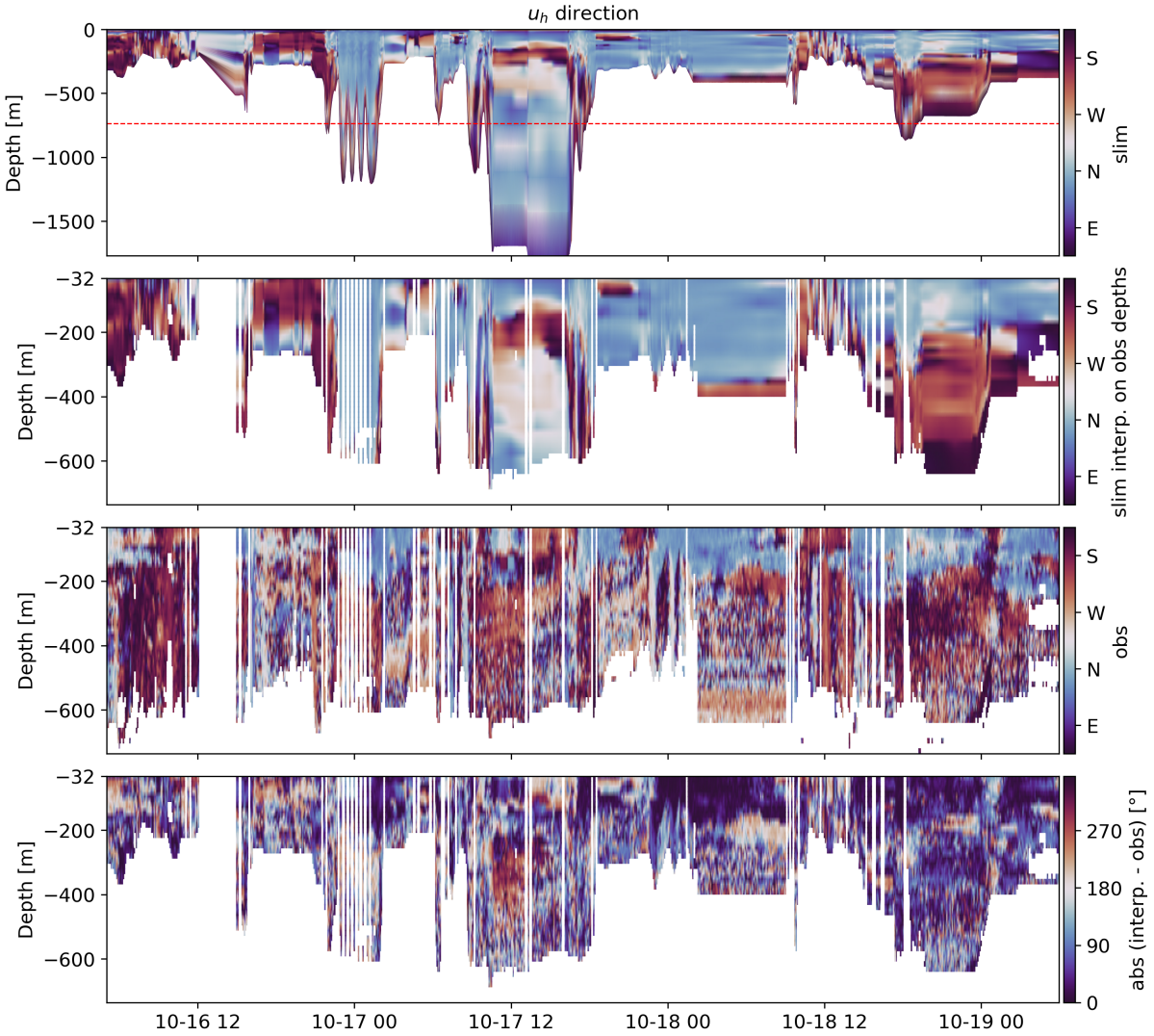

Figure C.3: current direction from os75

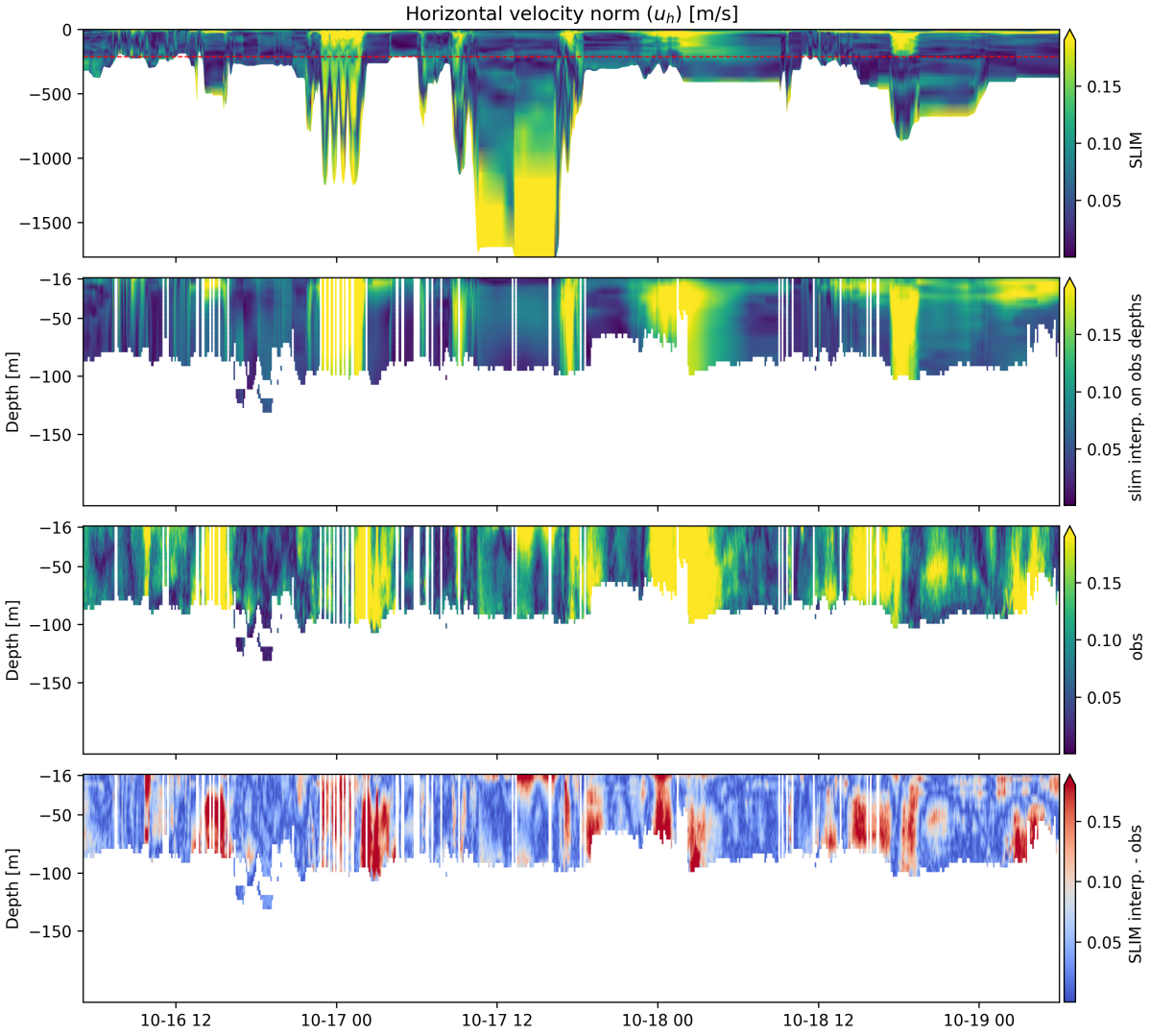

Figure C.4: current norm from wh300

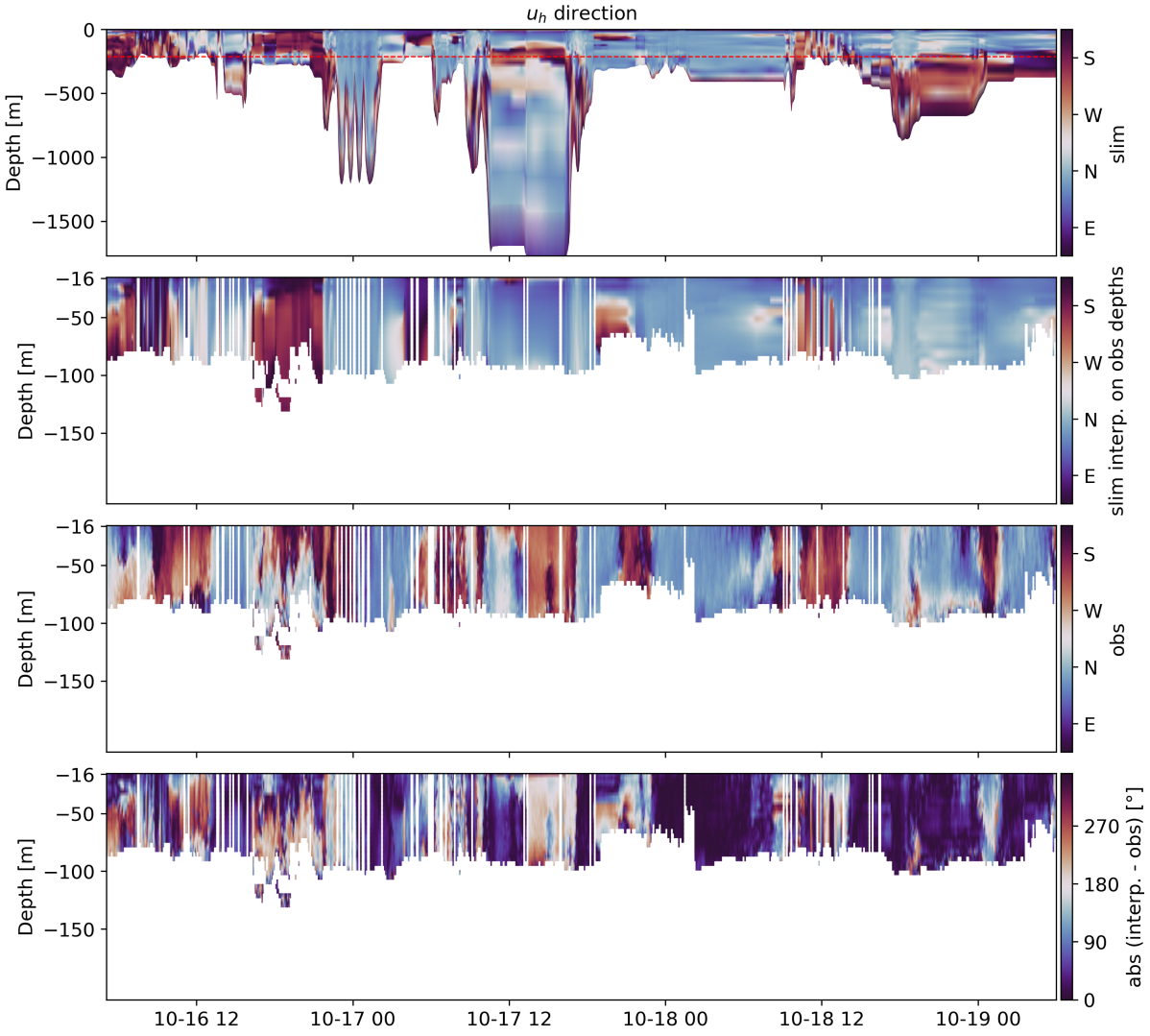

Figure C.5: current direction from wh300

C.3 Validation period 2

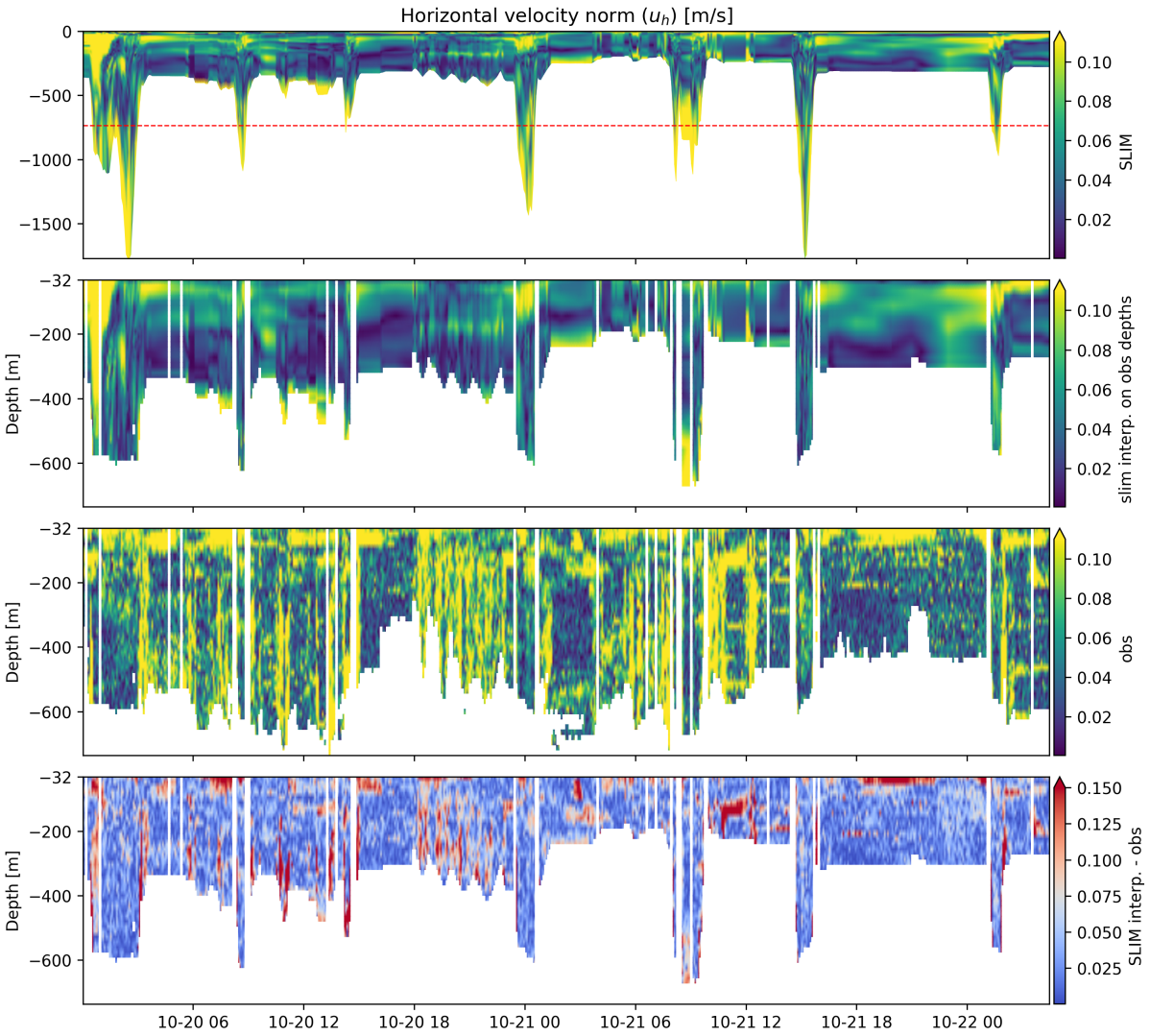

Figure C.6: current norm from wh300

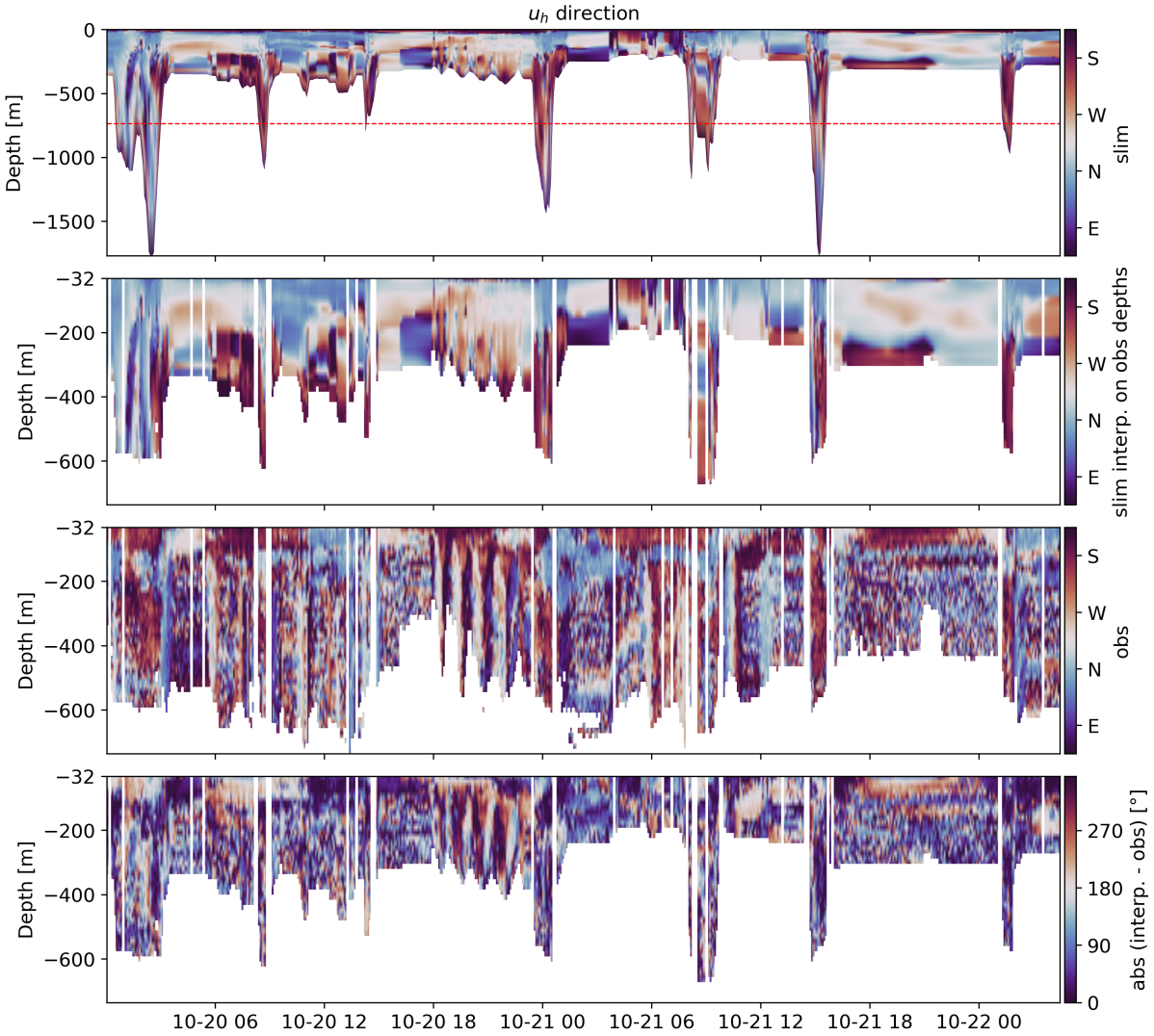

Figure C.7: current direction from os75

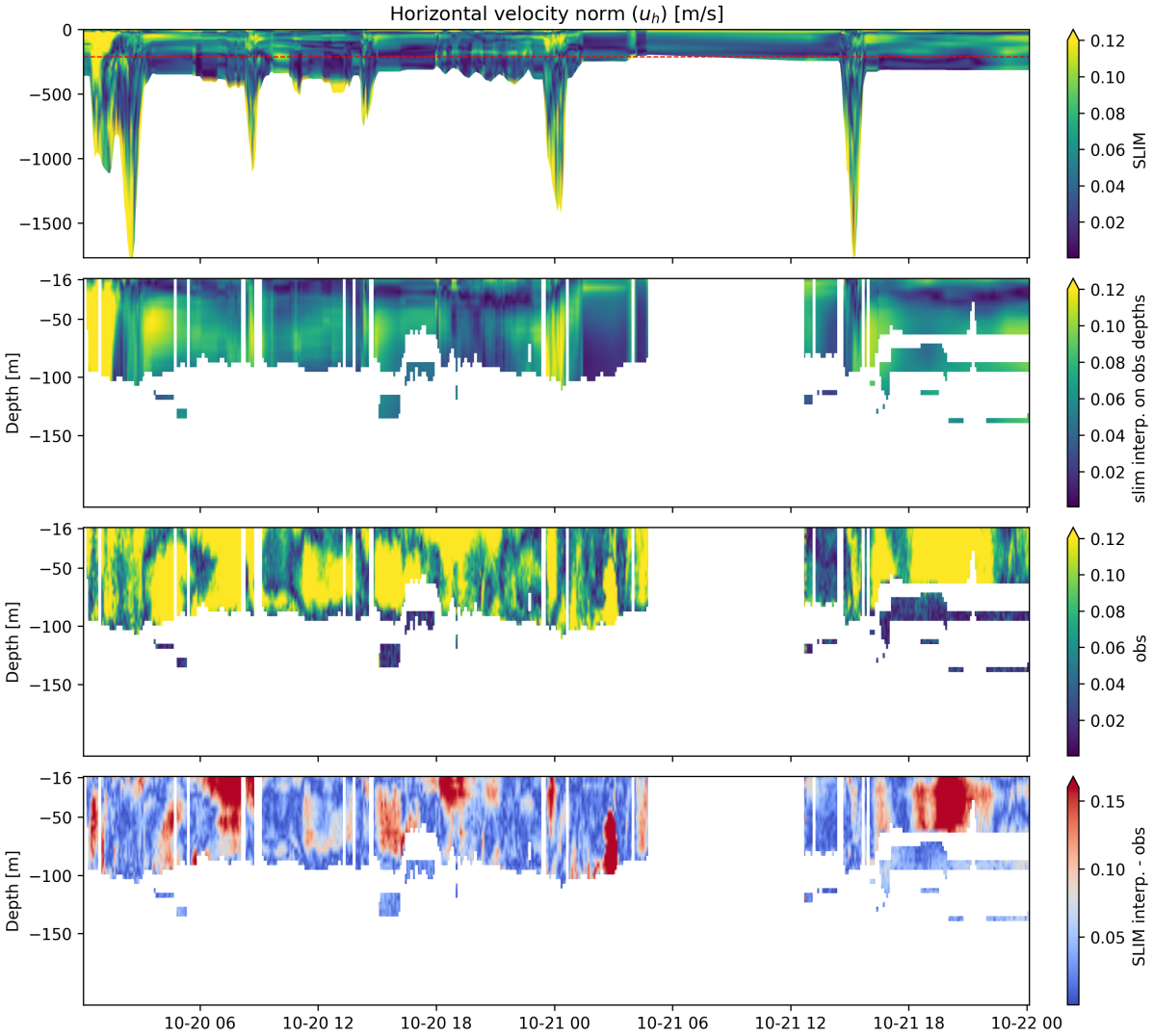

Figure C.8: current norm from wh300

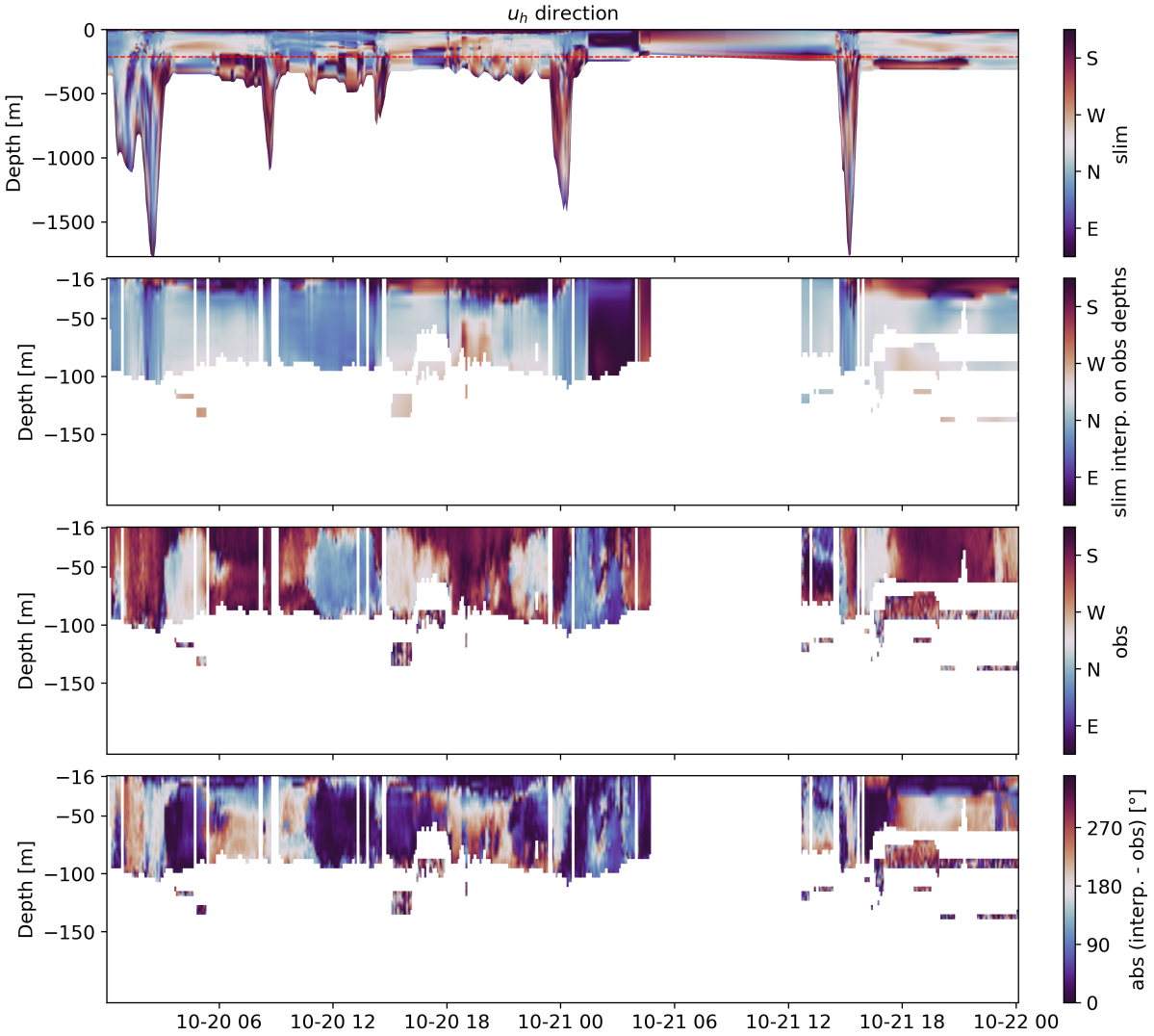

Figure C.9: current direction from wh300

Appendix D

Velocity field close-ups in the areas of interest

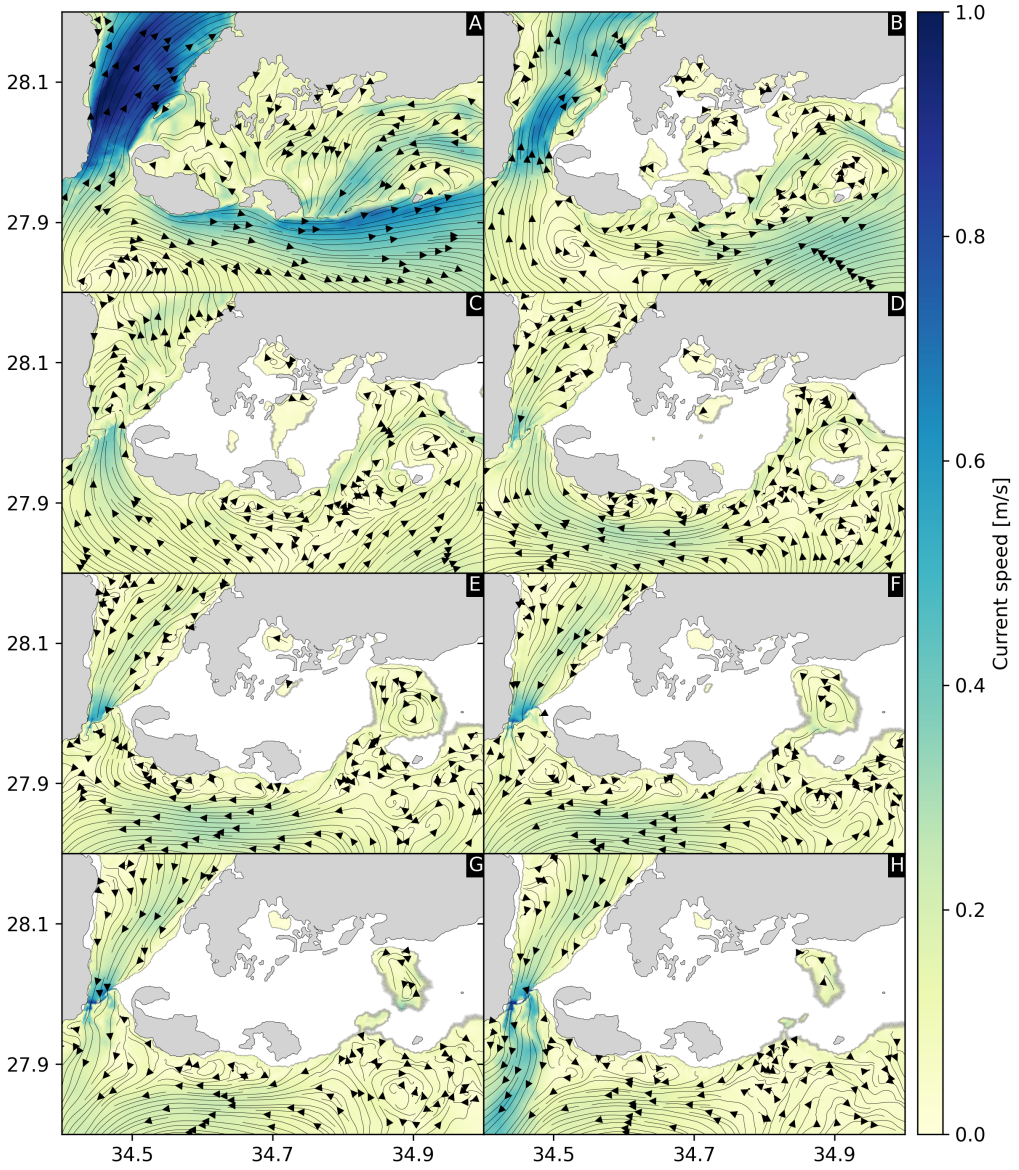

Figure D.1: Close-up snapshots of the velocity field streamlines and magnitudes on the Strait of Tiran on 2023/11/11 at 05:00 AM for different depths : (a) surface, (b) -20 m, (c) -40 m, (d) -60 m, (e) -80 m, (f) -100 m, (g) -120 m and (h) -140 m

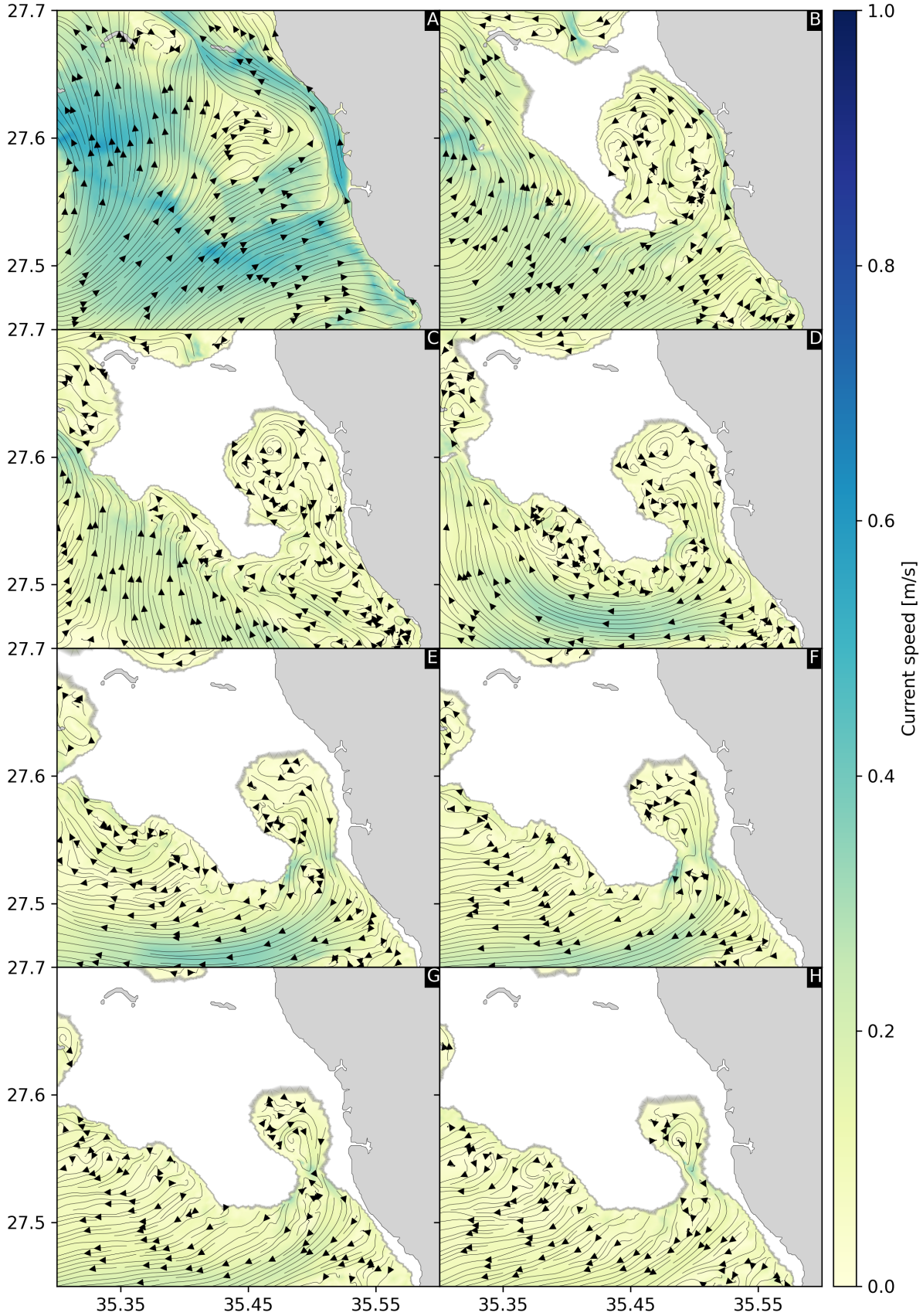

Figure D.2: Close-up snapshots of the velocity field streamlines and magnitudes on Oxagon on 2023/11/11 at 05:00 AM for different depths : (a) surface, (b) -20 m, (c) -40 m, (d) -60 m, (e) -80 m, (e) -80 m, (f) -100 m, (g) -120 m and (h) -140 m

Appendix E

ERA5 vs CERRA grid

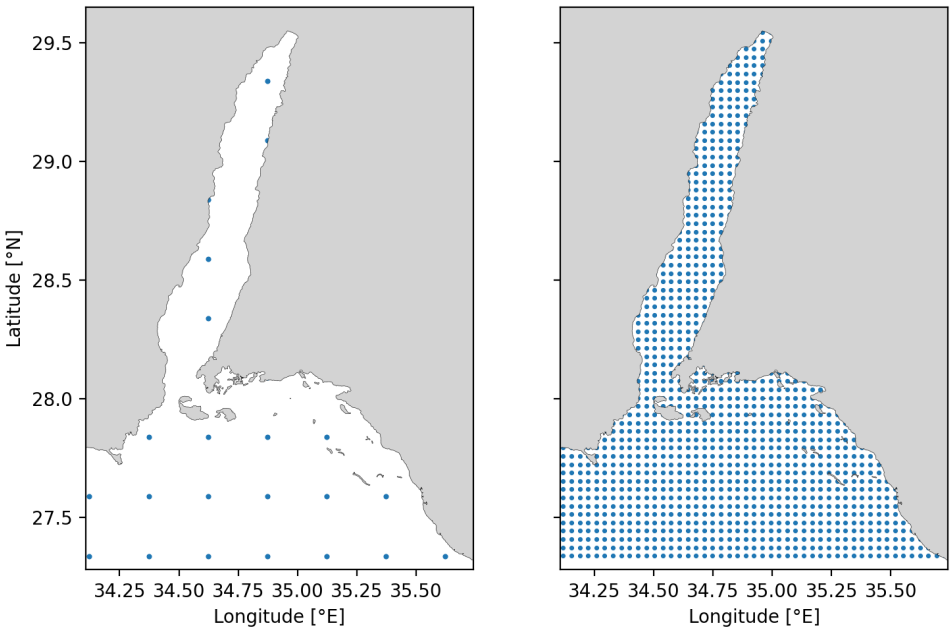

Figure E.1: ERA5 grid (left) and CERRA (right) grid comparaison

Assessing the environmental impact of the NEOM project on coastal ecosystems in the Northern Red Sed and Gulf of Aqaba

Mattias Van Eetvelt

In the context of a warming world, annual bleaching events are becoming more likely and threaten coral reefs on a global scale, leading to a growing interest in identifying local-scale thermal refugia. However such shallow reef refugia are predicted to disappear in a +2.0 °C climate world. Yet, hope remains as Northern Red Sea (NRS) corals could act as a thermal refuge until the end of the century. While being virtually immune to climate change, these so-called 'super-corals' are not immune to anthropogenic stressors such as the NEOM mega-project. Here, we used a three-dimensional multi-scale ocean model coupled with a Lagragian Particle Tracker (LPT) model to simulate sediment dispersal originating from coastal development sites and assess the environmental impact of the NEOM project on NRS corals. We show that fine sediments (<32µm) have a high potential to impact the entire Gulf of Aqaba (GoA) and part of the NRS, as they can remain suspended in the water column for up to one month and can settle 200 km away from their release site. We identified the most exposed reefs located within 10 km of Sindalah and along 45 km of the Oxagon coastline. Furthermore, we highlight that all the most exposed reefs are located in the NRS ; none are within the GoA. To our knowledge, this work is the first to quantitatively assess the environmental impact of the NEOM project on NRS and GoA shallow coral reefs. Based on our results, we expose the need for the implementation of mitigation measures to ensure sustainable coastal development. In a broader way, our model could provide further insights into marine pollution (e.g. desalination plants brines, heavy metals) and mesophotic-shallow reef interaction.

UNIVERSITÉ CATHOLIQUE DE LOUVAIN

Faculté des bioingénieurs

Croix du Sud, 2bte L7.05.01, 1348 Louvain-La-Neuve, Belgique | www.uclouvain.be/agro